MULTI-LEVEL MODELING OF TOTAL IONIZING DOSE IN a-SiO_2: FIRST PRINCIPLES TO CIRCUITS

By

Christopher J. Nicklaw

Dissertation

Submitted to the Faculty of the

Graduate School of Vanderbilt University

in partial fulfillment of the requirements

for the degree of

DOCTOR OF PHILOSOPHY

in

Electrical Engineering

August, 2003

Nashville, Tennessee

Approved:

Ronald D. Schrimpf, Chair
Kenneth F. Galloway, Chair
Robert Weller
Sokrates Pantelides
Daniel M. Fleetwood

ACKNOWLEDGEMENTS

First, I want to thank my family, my wife Rose, and my sons Richard, Christopher, Shawn, Travis and Manish, for their love and support. If not for them, nothing would have meaning.

I also wish to thank my co-advisors Ron Schrimpf and Ken Galloway for their support and continued confidence and my committee members Sokrates Pantelides, Robert Weller, and Dan Fleetwood for their numerous insights and suggestions.

TABLE OF CONTENTS

Appendix

LIST OF TABLES

LIST OF FIGURES

CHAPTER I

INTRODUCTION

Radiation-resistant electronics are integral to the aerospace, nuclear reactor and weapons communities. The study of radiation effects in semiconductor electronics, and the development of radiation-resistant integrated circuits, has an active scientific and engineering community that produces a wealth of data and conceptual understanding. Much has been published on basic damage mechanisms, and on device properties for a specific application. Attempting to apply this information to an area outside the purview of the radiation affects community, key pieces of information needed to link basic damage mechanisms to usable electronic design guidelines are often missing.

The subject of radiation effects in semiconductor devices is complex because of the numerous possible combinations of different types of radiation, radiation damage, and semiconductor devices. Also, the electrical behavior of the irradiated devices must frequently be monitored over decades of time.

An improved understanding of basic mechanisms, and linking this understanding to a design flow methodology, will give designers radiation-knowledgeable device models for the exploration of the design space, with the restrictions given by the radiation environment. This dissertation provides new insights into the basic mechanisms of a-SiO_2 defects, and provides a link between basic mechanisms and Electronic Design Automation (EDA) tools, providing an enhanced design flow for radiation-resistant electronics.

The design flow for creating integrated circuits is depicted in Fig. 1. The dashed black line represents the information flow for Total Ionizing Dose Modeling. In this dissertation, basic materials research using *ab initio* software to understand the type, the structure, and the electronic properties of intrinsic and extrinsic defects within a-SiO_2 is described. This information is then carried forward to the device modeling. Process modeling or raw data provides temperature information that is used to estimate the total concentration of defects within the device. Device modeling provides the electrical characteristics of the semiconductor device structure given a concentration of defects that is distributed by population and energy as obtained from the process and *ab initio* studies. Part of this research included the improvement and extension to three-dimensions a device

simulator that supports multiple carrier transport within the oxide for a given total ionizing dose. The output of the device simulator (current-vs-voltage curves) supports the Compact Modeling Framework (CMF). This dissertation work included the development of a CMF. This CMF provides the capability to create and modify SPICE compact model behaviors using macro-modeling techniques and Verilog-AMS within the SPICE simulation environment.

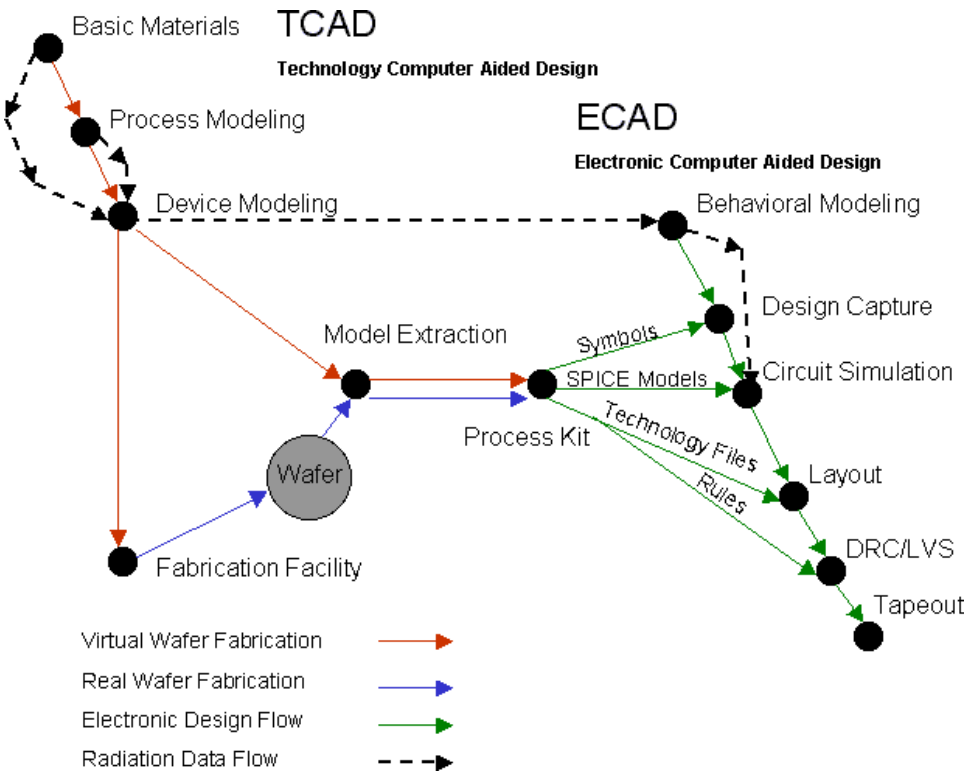

Figure 1: Design flow for creating integrated circuits using modeling tools.

Radiation Damage Mechanisms

The effects of radiation on semiconductor devices can be categorized by the basic radiation damage mechanisms:

Displacement Damage: Incident radiation displaces silicon atoms from their lattice sites. The resulting defects alter the electronic characteristics of the semiconductor crystal. It will be discussed mainly for completeness, as it is not part of the primary research effort described here.

Ionization Damage: Energy absorbed by electronic ionization in insulating layers, predominantly SiO_2, liberates charge carriers, which diffuse or drift to other locations where they are trapped, leading to changes in the electric fields. Ionization produces three types of effects: total dose, single event, and transient. These will all be discussed within this chapter.

Some devices are more sensitive to ionization effects, while other device types are dominated by displacement damage. Hardly a system is immune to either phenomenon, and many are sensitive to both at one level or another.

Displacement damage depends on the Non-Ionizing Energy Loss (NIEL) process. Energy and momentum transfer to lattice atoms depends on the mass and energy of the incident particles. A measure for displacement damage is displaced atoms per volume, and must be specified for a specific particle type and energy.

Ionization effects depend primarily on the absorbed energy, and are frequently assumed to be independent of the type of radiation. At typical incident energies, ionization is the dominant absorption mechanism. Ionization damage can be measured in terms of energy absorption per unit mass, being expressed in rad (1 rad = 100 erg/g). The charge liberated by a given ionizing dose depends on the target material. The ionizing dose must be referred to a specific target material, for example 1 rad(Si), or 1 rad(SiO_2).

Displacement Damage

An incident particle or photon capable of imparting energy of about 20 eV to a silicon atom can dislodge it from its lattice site[2, 3]. Displacement damage creates defect clusters. For example, a 1 MeV neutron transfers about 60 to 70 keV to the Si recoil atom, which in turn can displace roughly 1000 additional atoms in a region of about 0.1 μm radius.

Displacement damage manifests itself in two ways; the formation of mid-gap states, and/or a change in doping characteristics. The formation of mid-gap states facilitates the transition of electrons from the valence to the conduction band. In depletion regions, this leads to an increase in the generation current of reverse-biased pn diodes. In forward biased junctions, or non-depleted regions, mid-gap states facilitate charge loss by recombination. States close to the band edges facilitate trapping, where charge is captured and released after a certain time.

Ionization Damage

Ionizing radiation creates electron-hole pairs in the oxide and the silicon substrate. The electrons are quite mobile and move to the most positive electrode. Holes move by a rather complex and slow hopping mechanism, which allows trapping in the oxide volume, and an associated fixed positive charge. Holes that make it to the oxide-silicon interface can be captured by traps near the interface. This is illustrated in Fig. 2, which shows a schematic cross-section of an n-channel Metal-Oxide Semiconductor Field-effect Transistor (MOSFET). A positive voltage applied to the gate electrode attracts electrons to the surface of the silicon beneath the gate. This "inversion" charge forms a conductive channel between the n+ doped source and drain electrodes. Holes freed by radiation accumulate at the oxide-silicon interface. The positive charge build up at the silicon interface requires that the gate voltage be adjusted to more negative values to maintain the same amount of charge in the channel.

The trapped oxide charge distribution can depend on time, and more specifically, on how the electric field in the oxide changes with time. The charge state of a trap depends on the local quasi Fermi level, so that the concentration of trapped charges will vary with changes in the applied voltage. Ionization effects depend not only on the dose, but also on the dose rate. Figure 3 also shows a thick field oxide, which serves to control the silicon surface charge adjacent to the MOS device and prevent parasitic channels to adjacent devices. Positive charge buildup also occurs here.

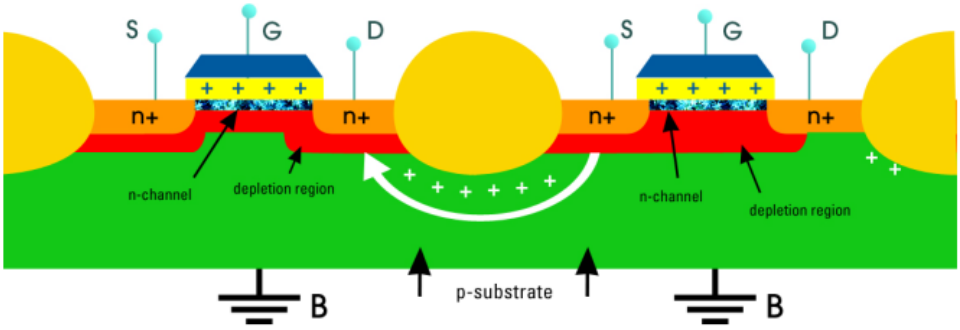

Figure 2: Cross section of NMOS device with trapped charge in the oxide.

Both bulk and Silicon-On-Insulator(SOI) CMOS structures, depicted in Fig. 3, are subject to the effects described above. SOI is often cited as a specifically radiation-hard technology because

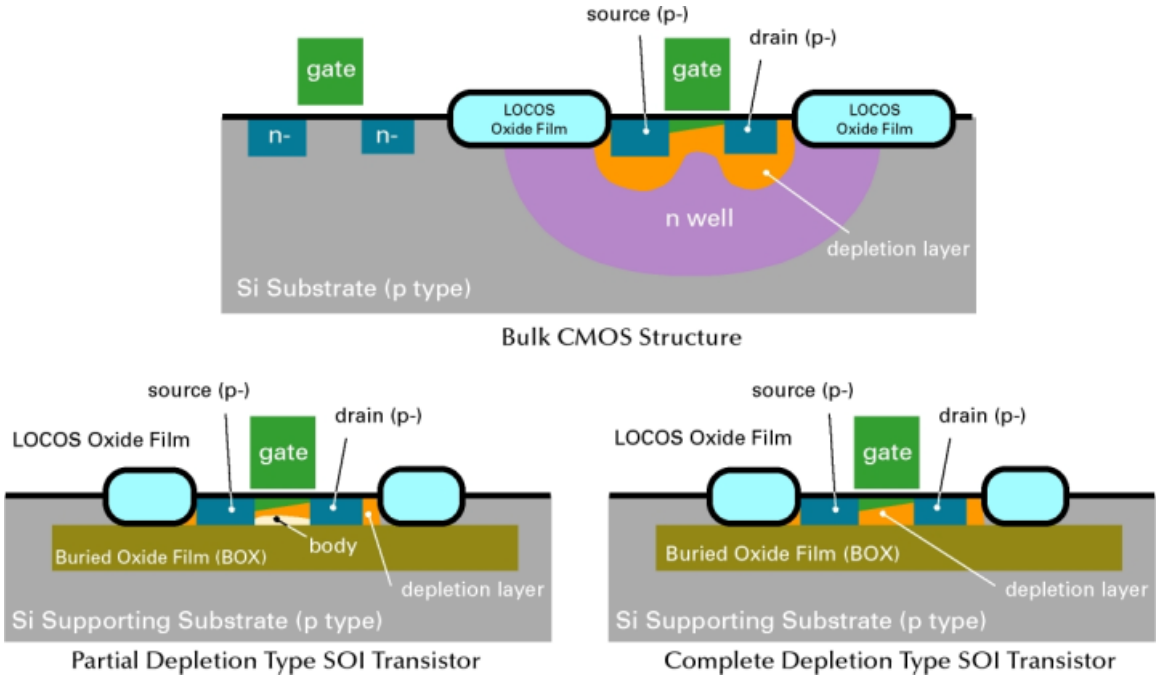

Figure 3: Bulk and SOI MOS structures.

of its resistance to transient radiation effects, primarily single-event effects caused by heavy ions or photo-currents produced by high dose-rate ionizing radiation. Although SOI can provide superior device speed because of reduced parasitic capacitance, this technology is not inherently more resistant to total-dose radiation. If anything, the additional oxide interfaces tend to complicate matters.

Total Dose Effects Of most concern in the total dose effects is the creation of hole-electron pairs in silicon dioxide, an insulator used to: 1) isolate neighboring transistors, 2) provide gate isolation in silicon MOSFET technology, and 3) provide surface passivation in silicon bipolar technology. In any silicon technology in which silicon dioxide is in contact with low acceptor doping level (p-type) silicon, total-dose effects must be considered. The dominant effects are due to holes being trapped at the interface of the Si-SiO_2, causing free electrons to be attracted to the interface, and resulting in inversion in the silicon near the interface. If the low doped p-region isolates two n-doped regions, then isolation is compromised and leakage currents may flow between the two n-regions.

In addition to hole trapping, interface traps, which may be charged positively or negatively depending upon bias condition, are also generated at the Si-SiO_2 interface. Two effects are

associated with interface traps. In n-channel MOS transistors under positive bias conditions, electrons are trapped in these states. This increases the threshold voltage. Electrons transporting through n-channels, or holes transporting through p-channels, undergo Coulomb scattering from the charged interface states. This results in reduction in carrier channel mobility and hence increased channel "on" resistance.

Dose Rate Effects Effects that are related to the rate at which radiation is absorbed in circuits include upset, latch-up, snap back in integrated circuits, and burn-out in bipolar and n-channel power transistors. All these effects are a consequence of radiation generated photocurrents in p-n junctions. Electron-hole pairs generated in the depletion region of a p-n junction by ionizing radiation are swept out by the high electric field present in this region. This promptly collected charge is termed the prompt photocurrent. Carriers generated within a diffusion length of the depletion region will diffuse to the depletion region where they are collected. These photocurrents sum in digital integrated circuits to produce transient currents that can cause changes in logic levels at digital gates due to charging and discharging of gate capacitance, or transistors being turned on or off. If the dose rate is high enough, the product of photocurrent and resistance causes a drop in power supply voltage across the metal resistance and power supply voltage actually present at the memory cell, and an error is introduced in the memory cell. This phenomenon is called rail-span collapse.

Single Event Effects (SEE) Single Event Effects refer to the fact that it is not a cumulative effect, but an effect related to individual interactions in the silicon. Ionizing particles can directly deposit enough charge locally in the silicon to disturb the function of electronic circuits (Fig. 4).

Single Event Upset (SEU) The deposited charge is sufficient to flip the value of a digital signal. Single Event Upsets normally refer to bit flips in memory circuits, but may also in some cases directly affect digital signals in logic circuits.

Single Event Latup-up (SEL) Bulk CMOS technologies (not Silicon On Insulator) have parasitic bipolar transistors that can be triggered by a locally deposited charge to generate a kind of short circuit between the power supply and ground. CMOS processes

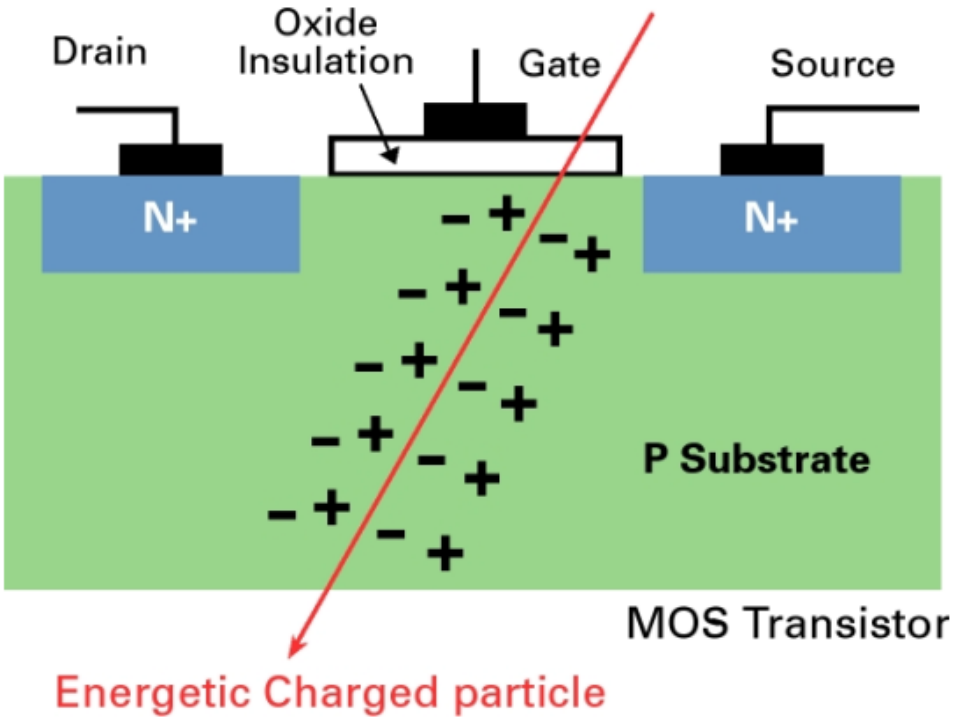

Figure 4: Interaction of cosmic rays with silicon.

are made to prevent this from occurring under normal operating conditions, but a local charge deposition from a traversing particle may potentially trigger this effect. Single event latch-up may be limited to a small local region, or may propagate to affect large parts of the chip. The large currents caused by this short circuit effect can permanently damage components if they are not externally protected against the large short circuit current and the related power dissipation.

Single Event Burnout (SEB) Single event burnout refers to destructive failures of power MOSFET transistors. This destructive failure mechanism is normally associated with failures in the main switching transistors of switching mode power supplies.

Approaches Towards Radiation Hardened Integrated Circuits

Commercial electronics can frequently survive 3-10 krad(Si) of total dose without significant parametric degradation. The failure mechanism is typically field-oxide inversion, resulting in increased leakage current. They can also remain functional (although degraded) from 10-30 krad(Si), but they may suffer a high single-event upset rate or possible latch-up when struck by heavy ions.

Some fabrication processes used to harden integrated circuits (ICs) against total ionizing dose

are closely guarded secrets, protected either by government classification or company proprietary restrictions. What can be examined, though, are some particulars about the principal process factors affecting the total dose tolerance.

The first step in hardening a CMOS IC against total dose radiation is to minimize voltage shifts, or their impact in the circuit, due to radiation induced charge trapping in the gate and field oxides. Two approaches can be used, either individually or in parallel: reducing the number of holes trapped in dielectric layers, and compensating for the trapped holes with trapped electrons.

The easiest way to minimize the trapped-hole density is to thin the oxide[2]. A clean gate oxide less than 4-5 nm thick, which is typical of today's commercial integrated circuits, can usually survive up to 100 krad(Si) or more with no process changes. On the other hand, where local oxidation of silicon is used, field oxides must remain thick to meet isolation and planarity requirements. Minimizing the trapped-hole density in them is much trickier and requires special processing.

Adding electron traps to offset hole traps is another method of countering radiation effects on field or isolation oxide structures. The addition of electron traps within the a-SiO_2 structure is achieved through implantation or introduction of an element. Hardness levels in excess of 300 krad(Si) can be achieved. Specific approaches for radiation hardened ICs are outlined below.

Use of ion implanted silicon-dioxide films It is observed that radiation-induced interface-trap buildup is suppressed using ion implanted SiO_2. By using a large arsenic ion dose, the interface-state buildup can be suppressed by one order of magnitude. It is found that interface-state buildup depends on the ion dose, the gate bias during irradiation and the annealing atmosphere[2]. After applying this technique to a conventional bipolar process, the current gain in lateral pnp transistors degraded by only 10% after 10 Mrad(SiO_2) irradiation.

Radiation induced trapped positive charges can be compensated by implanting aluminum. Aluminum in SiO_2 films acts as an electron trap, compensating for the positive trapped charges when in the right concentrations. Si atoms can also be implanted into silicon dioxide films. The Si changes the SiO_2 stoichiometry to an SiO_x stoichiometry, providing electron traps. Process conditions must be controlled. Temperatures over 900°C cause Si to diffuse rapidly. The diffusing Si tends to form nano-crystals, reducing its compensating properties[4].

Circuit Design Circuits can be made harder to ionizing radiation by the employment of circuit

design techniques. Radiation Hardened By Design (RHBD) methodology is described in [5].

Shielding Using radiation shields, typically of a tungsten/copper alloy, is another choice. They can either be built into the package structure, or be attached to the top and bottom[2]. While they are effective in reducing the electron component of the total dose radiation, they are much less effective in lessening the proton radiation.

A Radiation-Resistant Electronics Design Methodology

With the maturity of Technology CAD (TCAD) tools[6, 7], Real Wafer Fabrication (RWF) can be emulated by process simulation, from which realistic device structures and doping profiles can be generated, and transistor performance can be characterized through device simulation with reasonable accuracy. Interconnect delays can also be extracted through technology characterization, which can provide information for Design Rule Checker (DRC) and layout parasitic extraction (LPE) tools in the physical design. Simulation Program with Integrated Circuit Emphasis (SPICE) parameters can also be extracted from the "virtual device" I-V characteristics for back-annotating circuit simulators and timing analyzers, which allow "calibrating" EDA tools based on TCAD tools. Of course, how effective this approach will be in aiding first-time silicon success depends on how well the process and device simulators are calibrated to the RWF results. This calibration involves "manufacturing-verification" in the "Virtual Wafer Fabrication" (VWF) environment.

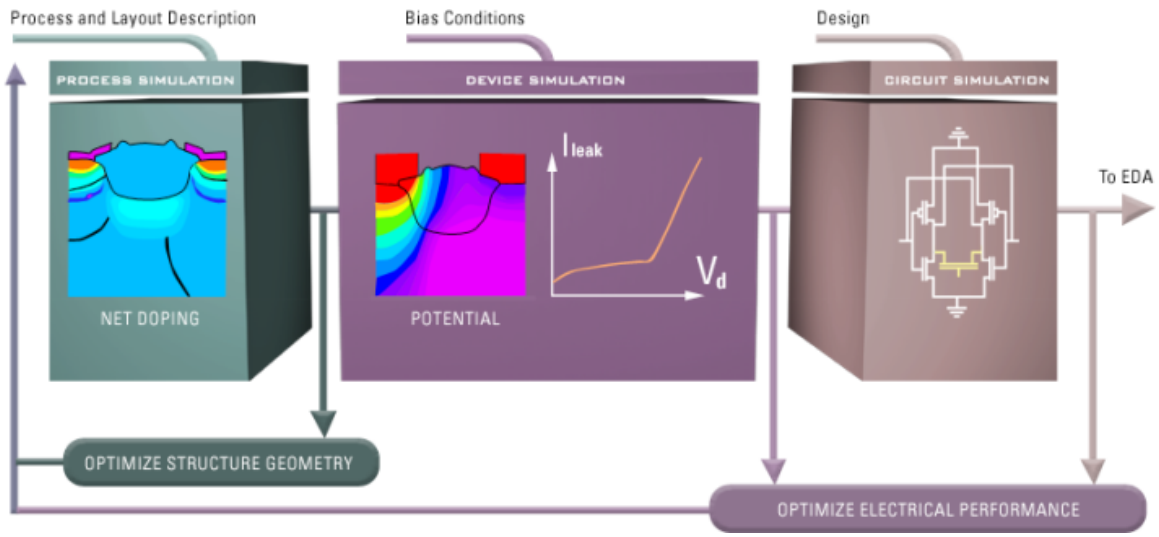

Figure 5: Design/Fabrication Flow

The design/fabrication flow described above is illustrated in Fig. 5. Traditionally, technology developers and circuit designers are largely separate entities loosely linked by a set of GDSII physical device layout files and SPICE model parameters. This worked well before entering into the nanometer era, due to the fact that transistor characteristics could be modeled unambiguously and statistical variations due to process fluctuations only represent a relatively small percentage of the nominal characteristics being modeled. The challenge in the nanometer era is the development of models, algorithms, and methodologies that are accurate as well as efficient in order to make the best use of the available technology while reducing design margins. From a technology/transistor/circuit modeling point of view, as opposed to top-down or layout designs, the Compact Model (CM) is at the core of the modeling hierarchy, as it bridges between a given technology and circuit design, and determines the accuracy/speed for the design as well. The real challenge is how to "propagate" the detailed physics captured in lower-level atomic, process and device modeling to higher-level (circuit/block) abstractions, and integrate the various views of the system. The varying views of a transistor system are illustrated in Fig. 6.

Multi-Level Modeling Approach

There are various ways to classify a design flow and methodology depending on applications, such as top-down vs. bottom-up, analog vs. digital, synthesis vs. analysis, etc. In this dissertation, a multi-level hierarchical modeling approach for radiation-effects in a given (CMOS-SOI) technology will be introduced. This multi-level approach is depicted in Fig. 7.

Atomic level modeling is related to the detailed atomic structures, and examining the type of defect, its structure, and its energy distribution. Atomic level modeling is accomplished by numerically solving Schrodinger's equation using Hartree-Fock (HF) or Density Functional Theory (DFT)[8].

Technology level modeling is related to the detailed device layer structures, and doping profiles, and their dependence on process variations, as well as the resulting electrical characteristics. This is modeled by numerically solving process and transport differential equations for a single transistor.

Device level modeling is related to the description of transistor terminal characteristics normally expressed in compact closed-form equations. The major challenge at this level is to reduce

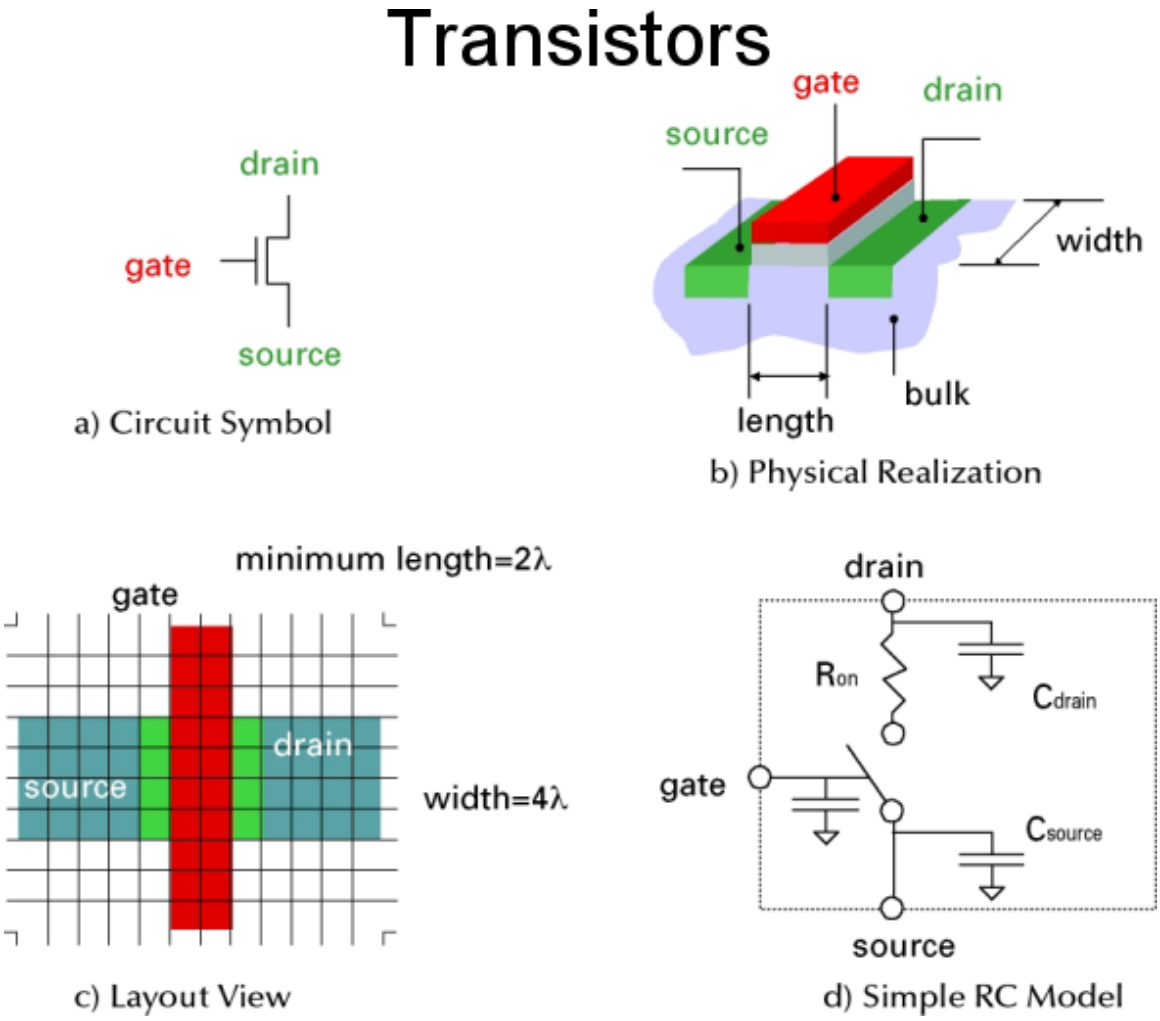

Figure 6: Multiple views of a transistor from the perspective of a) a circuit designer, b) a device engineer, c) a layout engineer, and d) a model development engineer.

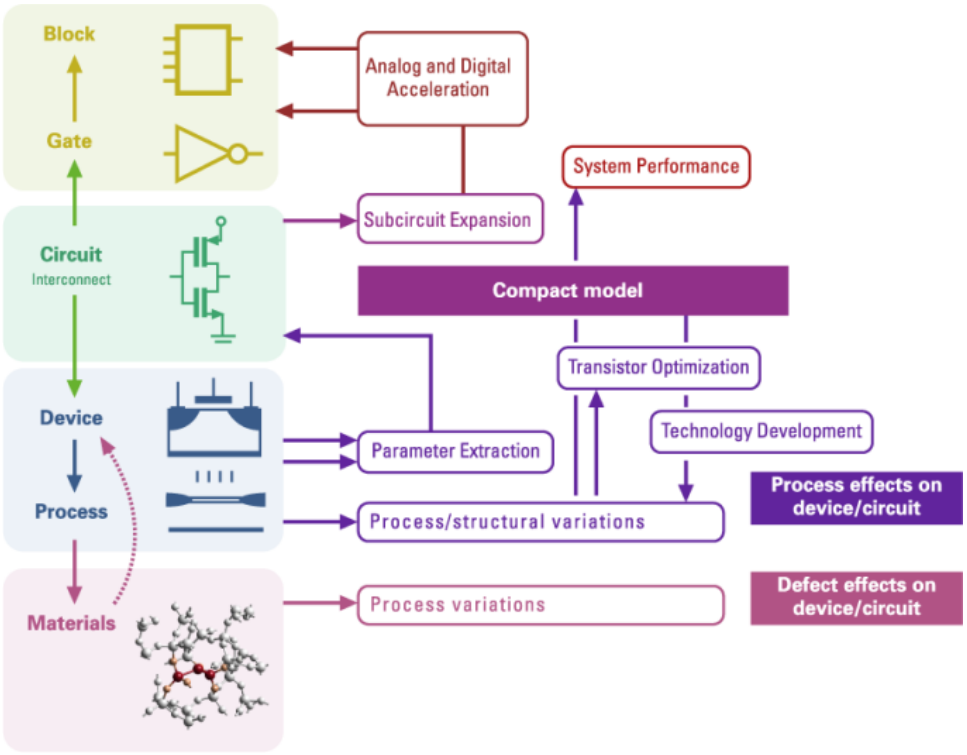

Figure 7: Compact multi-level technology/transistor/subsystem modeling.

the device behavior at the technology level to a spatially-independent, 0-dimension representation, which will be used as a model for the nonlinear device at the circuit level. In our multi-level hierarchical modeling approach to radiation effects, the traditional TCAD flow of Fig. 5 is replaced by Fig. 8.

Circuit level modeling traditionally refers to the solution of large linear/nonlinear systems of equations by various matrix-solution techniques. Besides the normal convergence problems in any iterative solution techniques, as well as storage allocation for large matrices, a major concern at this level is the accuracy/speed tradeoff, which depends largely on the device models and the circuit size.

System level modeling, in a narrow sense for this discussion, refers to the analysis and description of the behavioral blocks that make up a given system. From a simulation perspective, it requires acceleration methods to simulate these blocks at a higher level of abstraction, such as event-driven logic simulators, selective-trace algorithms, static-timing analyzers, analog behavioral modeling (Verilog-A/AMS, VHDL-AMS), Very High-Speed IC HDL (VHSIC HDL or

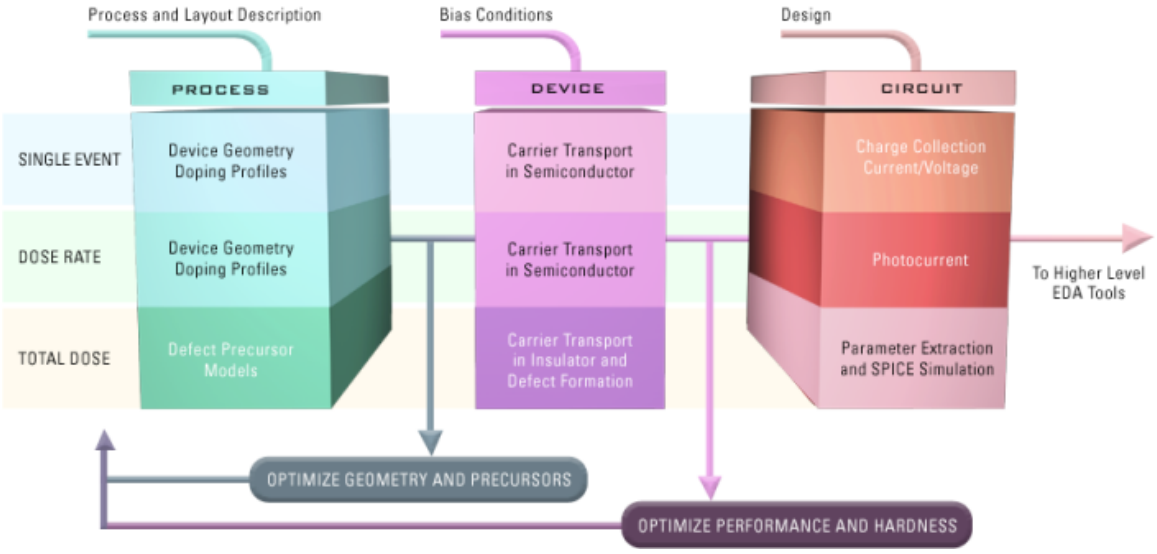

Figure 8: TCAD design flow for radiation effects modeling.

VHDL), Verilog, and System-C[9, 10, 11, 12].

Traditionally, the above five levels of abstraction are relatively independent or loosely coupled, represented by atomic, TCAD, CM, SPICE, and system, respectively (Fig. 9); each of these has its own target domain as well as developers, which results in different tools. There is no direct link between Atomic and TCAD, TCAD and CM, or SPICE and System level tools. The interaction between CM and SPICE is at the core of the modeling hierarchy, but the traditional approach is to have a complicated CM as a nonlinear "element stamp" in a "flattened" SPICE matrix solver, which limits its extension to higher levels of abstraction for large circuits. Recent development addresses these issues, for example, using hierarchical simulators. However, due to the fact that circuit tool vendors and device model developers are largely separate entities, current practice is still to rely heavily on the foundry/manufacturer to provide the model parameters, for the designer to create user-sub-circuits to characterize transistor behaviors (RF, noise, worst-/best-case), and to run the design on various commercial simulators.

This incompatibility is especially frustrating in macro-modeling, where one would like to create only one model using the SPICE sub-circuit feature and basic circuit elements, which then could be used in any SPICE version. Instead, a separate and slightly different model file must be created for each circuit simulator.

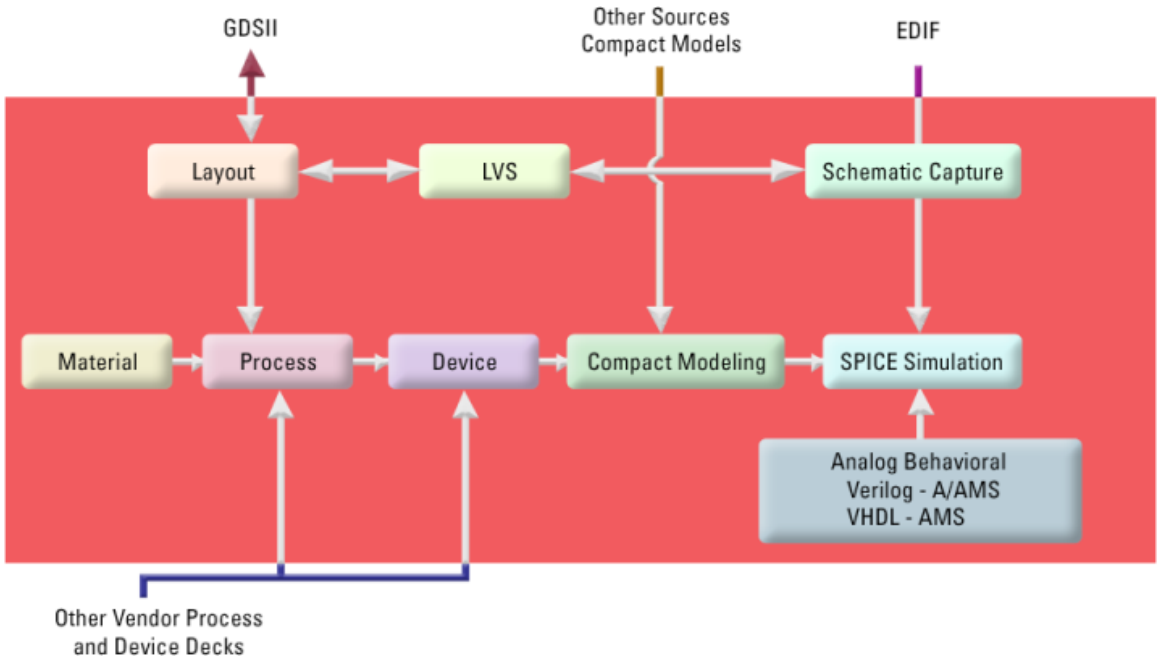

Figure 9: Integration of design tools that provide a design flow for radiation hardened electronics.

Physical Models Versus Macromodels

Any circuit simulator is only as good as its device models, which map the real world into the simulator. The term model, however, has distinct meanings to different people. In this dissertation, it refers to the equivalent circuit and the model equations that describe a given class of devices, such as diodes or transistors and their technology such as bipolar or MOS field effect. Correspondingly, the term modeling is used to indicate the effort of creating a model for a given class of devices. Model parameters are numbers that must be put into the model to describe a given instance of the class. Parameter extraction refers to the process of obtaining the model parameters from measurement data or manufacturer specifications. The term physical model refers to a device model in which the model equations describing charges and currents are more or less derived from the physical behavior of the device. This usually means that the model is too complex to be described in the input language of a circuit simulator. It has to be implemented into the simulator code by programming. This also makes it possible to use various mathematical short-cuts and programming tricks to make the model as fast as possible. However, the term physical model is somewhat arbitrary, and should actually be read as complex model, since there are many semiconductor device models that are markedly non-physical, but still so complex that code implementation is the only feasible way to use them. An example of such a model is the University of California, Berkeley, BSIM

compact model family[13] for MOSFETs.

All circuit simulators of today have the capability to use sub-circuits. Elements that are repeated many times in a circuit description can be put inside a sub-circuit block with a specific name and a number of external nodes. Only the sub-circuit name and the connecting nodes need to be repeatedly written in the circuit description. The elements in the sub-circuit could form the equivalent circuit of a device model, in which case the sub-circuit is the macro-model of the device. A macro-model utilizes the elements already defined in the circuit simulator, like resistors, capacitors, inductors, voltage and current sources, and also semiconductor models like diodes and Field Effect Transistors (FETs). Advanced circuit simulators offer the possibility to use mathematical expressions within the macro-model. This capability gives the designer the ability to achieve characteristics that could have been described by a mathematical equation. Recent advances, supported by this research, now allow certain circuit simulators to support analog behavioral constructs, inclusive of languages such as Verilog-AMS and VHDL-AMS. This capability supports very complex macro-modeling while still within the SPICE simulation domain. Combining this technology with proven physical models now allows a circuit designer to use macro-models to explore designs for very specific environmental conditions.

The advantages of retaining the physical model implemented in a specific circuit simulator are accuracy and simulation speed, though the latter depends very much on the device complexity, and on how well the code has been written. Generally, implementing a model in a simulator by programming offers a great deal of freedom in describing the device behavior, limited only by the programming language. The drawbacks consist of the special knowledge necessary about the internal structure of the simulator code, and the fact that in most cases the code is simply not available. Additionally, errors and convergence problems are easier to fix for a macro-model than for a physical model because of the difference in complexity.

Outline of This Dissertation

This dissertation presents a radiation-resistant electronic design methodology providing data flow from *ab initio* physics to circuit simulation that is consistent with the design flow of commercial integrated circuits. Amorphous silicon dioxide (a-SiO_2) remains a dominant isolation oxide, and plays a significant role in the total ionizing dose response of a semiconductor device[14, 15]. Chapter II describes the basic mechanisms of MOS radiation response. Chapter III provides an

overview of a-SiO_2, summarizing the basic properties, defects and the thermodynamic properties of defects at equilibrium. This chapter examines the equilibrium concentration of total defects, given the semiconductor's processing history. This chapter will also introduce the method used to approximate the device-level behavioral properties of capture cross-section.

Chapters IV and V examine typing and the statistical nature of defects within a-SiO_2. Using Density Functional Theory (DFT), described in Appendix A, the structure and energetic configurations of defects, as well as their electrical behaviors within an amorphous structure is explored.

Using the theoretical foundations of Chapter III, the energetic and electrical behaviors described in Chapters IV and V allow the use of a device simulator supporting transport in the insulating material. Chapter VI discusses the implementation of a trapping model and the results of device simulations including the effects of total ionizing-dose. This chapter also discusses the utilization of Technology Computer-Aided Design (TCAD) in constructing compact models for circuit simulation.

Finally, in Chapter VII compact models will be presented that support circuit level simulation with effects of exposure to total ionizing-dose.

The technology chosen for demonstrating the multi-level approach to modeling the effects of total ionizing-dose was SOI MOS devices. Appendix B provides a review of basic MOS physics, while Appendix C provides an introduction to SOI technology.

CHAPTER II

BASIC MECHANISMS OF THE IONIZING-RADIATION RESPONSE OF MOS STRUCTURES

Introduction

The total-dose ionization problem that occurs in MOS systems is due to the radiation-induced charging, normally positive, of the thin gate-oxide region and isolation oxides, and in the buried oxide for Silicon On Insulator technology. The charge-induced fields result in voltage offsets or shifts in the turn-on voltages of the devices; these offsets or shifts lead to circuit degradation and failure. The incident radiation creates electron-hole (e-h) pairs. The energy required is approximately 17 ± 1 eV [16] to generate an e-h pair in SiO_2. This will result in a total number of e-h pairs generated per unit dose in SiO_2 of approximately $8.1 \times 10^{12} cm^{-3} rad^{-1}(SiO_2)$.

The radiation-induced oxide charging problem is complicated by the details of the time dependence of the radiation response of the simple MOS structure shown in Fig. 11, having to do with a wide variation in the characteristic time scales for the various physical processes involved. The complexity of the time-dependent response has implications in prediction of circuit response. This chapter provides an introduction to the basic mechanisms of the radiation response of MOS structures.

Response Mechanisms

There are four major processes contributing to the radiation response of MOS technology:

1. In a-SiO_2, the radiation-generated electrons are much more mobile than the holes, and they are swept out of the oxide in times on the order of picoseconds[2]. Within the first few picoseconds some fraction of the electrons and holes recombines. This fraction depends, to a great extent, on the applied field and on the energy and type of the incident particle. Two primary models of recombination have been developed. The columnar model applies when the e-h pairs are close together, and thus a large number recombine. The geminate model applies when the e-h pairs are widely separated, so that a much smaller number of carriers will recombine[2]. The surviving holes cause a negative voltage shift in the electrical char-

acteristics of MOS devices. These changes appear in the threshold voltage (V_T) or flatband voltage (V_{FB}) for MOS capacitors. These changes can be separated into two components: the voltage shift due to charge in the oxide, ΔV_{ot}, and that due to the interface traps, ΔV_{it}. The fractional yield of carriers, those escaping recombination in a-SiO_2, is discussed as a function of the applied field for various sources of radiation in [2].

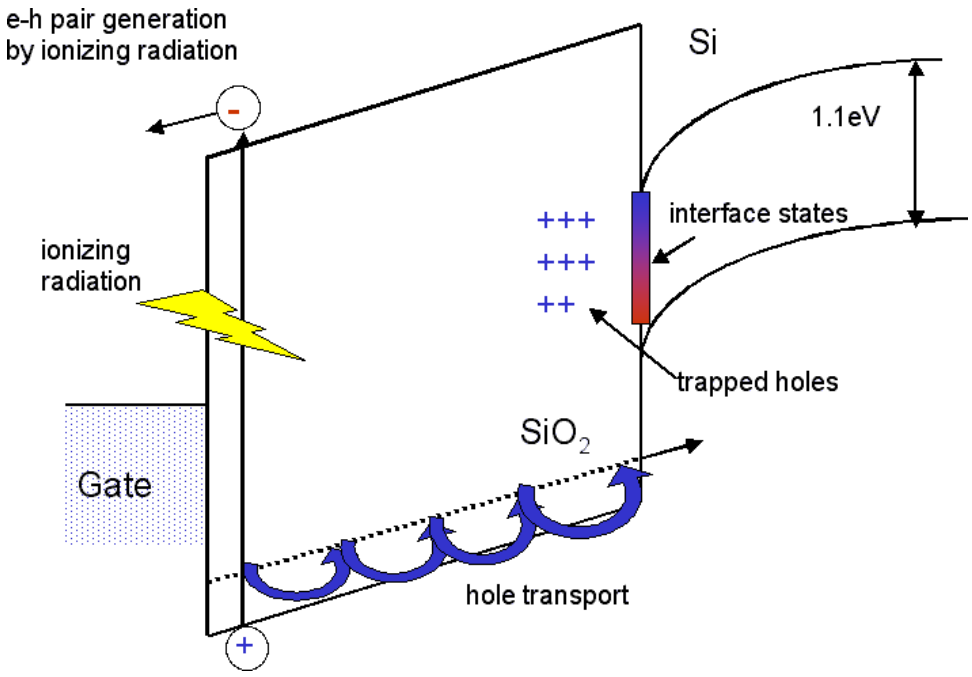

Figure 10: Schematic of radiation effects problem in MOS structures after [1].

2. Over a period of time on the order of tens of milliseconds, the holes transport through the oxide in response to any electric fields present. This hole transport process is dispersive in time. Two models have been proposed for this dispersive transport: a) hopping transport where the holes directly tunnel between localized trap sites within the SiO_2 band gap, and b) multiple trapping, where the holes are trapped at localized trap sites moving within the oxide due to drift and diffusion between trapping events. This dispersive transport process is sensitive to applied field, temperature and oxide thickness. Both of these models can be mathematically described by the continuous-time random walk (CTRW) model[2].

3. Some fraction of holes transporting through the SiO_2 to the SiO_2/Si interface under a positive applied gate bias are captured in long-term trapping sites, and cause a negative voltage shift

that continues in time for hours to years. Hole trapping and annealing are sensitive to the processing of the oxide, applied field, and temperature[17].

4. The remaining MOS structure response is determined by the buildup of interface traps at the SiO_2/Si interface. Both prompt interface traps, present immediately after a radiation pulse, and a delayed time-dependent buildup of states that can continue for thousands to tens of thousands of seconds at room temperature can be seen. The buildup of interface traps at the SiO_2/Si interface is also sensitive to the processing, applied field and temperature[18, 2].

The time-dependent recovery curve in Fig. 11 shows the radiation-induced shift in threshold voltage as a function of log time. The NMOS device is under positive gate bias at room temperature after exposure to an ionizing radiation pulse of $\sim$1 ms. This figure relates the major features of the response to each of the primary processes discussed earlier in this chapter. The initial shift (shown in red) is governed by the electron/hole pair creation in the SiO_2 bulk and by the initial recombination processes. The early annealing (shown in blue) is due to the hole transport process. The remaining shift in V_T is due to the deep hole trapping near the SiO_2/Si interface. This anneals linearly with log time. The solid curve in Fig. 11 corresponds to transport, trapping, and annealing of holes alone. In addition to long-term annealing of trapped holes, however, a buildup of radiation-induced interface traps may occur, typically in the time regime between $\sim 10^{-2}$ and 10^3 s, which is indicated by the green curve in Fig. 11. If the interface trap contribution is large, the change in threshold voltage becomes positive, giving rise to what is called super recovery or rebound[2].

Bulk a-SiO_2 Charge Trapping

The number of deep hole traps in the bulk of a thermally grown silicon dioxide layer given today's techniques is usually fairly small. Most of the traps are located near the Si/SiO_2 interface, or near the gate electrode/SiO_2 interface. The holes generated by ionizing radiation in the bulk of an oxide layer will be swept under a positive gate bias towards the SiO_2/Si interface, and some fraction of them will be trapped, depending on the hole trap density and capture cross-section. It is the E′-center that has been shown to be the dominant defect responsible for the radiation-induced positive charge[2] even though it is not the sole factor[19]. These trapped holes give rise to a

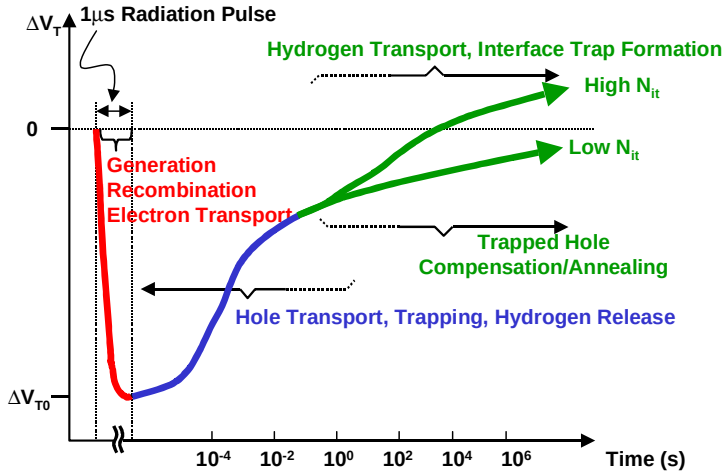

Figure 11: Summary of the transient response of an NMOS transistor's threshold voltage to a radiation pulse.

threshold voltage shift, ΔV_{ot}, given by:

$$\Delta V_{ot} = -\frac{1}{C_{ox}} \int_0^{t_{ox}} \frac{x}{t_{ox}} \rho(x) dx = -\frac{q}{\varepsilon_{ox}} t_{ox} \Delta N_{ot} \tag{1}$$

Here q is the electron charge, $C_{ox} = \varepsilon_{ox}/t_{ox}$ is the oxide capacitance, ε_{ox} is the dielectric constant of the a-SiO_2, t_{ox} is the thickness of the oxide, $\rho(x)$ is the oxide charge density, and ΔN_{ot} is the areal trapped charge density referred to the Si/SiO_2 interface.

Trapped holes can be removed or neutralized by compensating electron trapping, either by thermal annealing, or by tunneling of electrons from the silicon substrate or gate. Complete thermal annealing often requires temperatures above 300°C. The temperature for annealing depends on the distribution of energies inside the SiO_2 band gap for the trapped holes, as shallower trap levels emit charge at lower temperature[2].

The tunneling annealing process is roughly linear with log(t) dependence, where t is the time after irradiation. Tunneling probability decreases with distance, as seen in Fig. 12.

Because of this decrease in probability due to distance, only defects within 4-5 nm from either interface are neutralized due to tunneling. However, this also means that for very thin oxides ($< 10\ nm$), significant neutralization of trapped holes could occur via tunneling in a relatively short time interval.

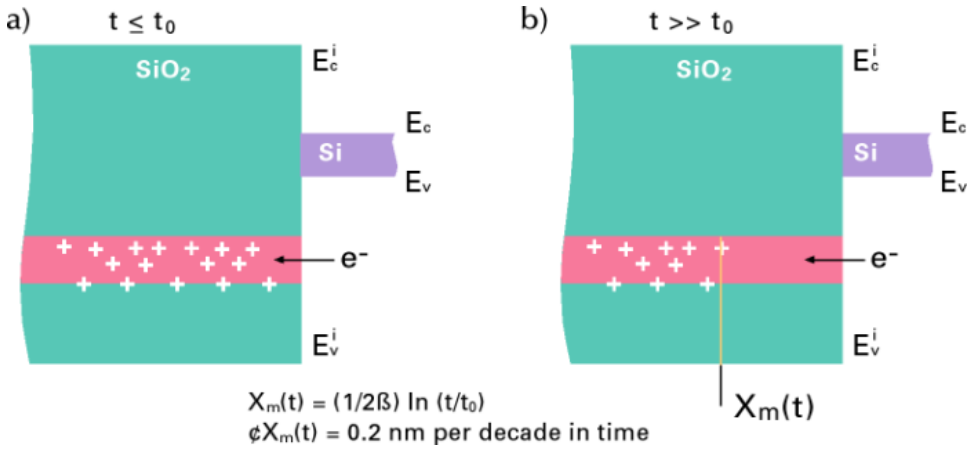

Figure 12: Trapped hole removal by tunneling.

Interface Charge Trapping

Interface traps have energy levels within the forbidden band gap at the SiO_2/Si interface. They are located spatially at or very near that interface, and freely exchange charge with the silicon. Electron Spin Resonance (ESR) results[20, 21, 22] have shown that the P_b center is generated in MOS structures by ionizing radiation. This center is trivalent silicon at the Si/SiO_2 interface with a dangling orbital perpendicular to the interface[2]. The net charge of these interface traps can be neutral, negative or positive. Defects are classified as donors if they are positively charged when above the Fermi level and neutral when below, or acceptors if they are neutral when above the Fermi level, and negatively charged when below. ESR work[20] has shown that the primary interface trap, the P_b defect, is amphoteric. The interface trap levels below midgap are donor like, whereas those above midgap are acceptor like. The P_b-center was first identified as an interface defect by Poindexter *et al.*[23]. One center, the P_b, is observed at the (111) interface while two centers, the P_{b0} and P_{b1}, are present at the (100) interface, as shown in Figs. 13(a) and 13(b), respectively. These P_b-like defects represent a dominant part of early interface states[2].

Years of research[24, 25, 26, 27] have helped to establish hydrogen's key role in interface trap formation. Three model categories have been proposed to explain the buildup of interface traps over time: injection, stress and hydrogen models. In the hydrogen model, the model most associated with irradiation, a trivalent Si atom at the SiO_2/Si interface is bonded to a hydrogen (H)

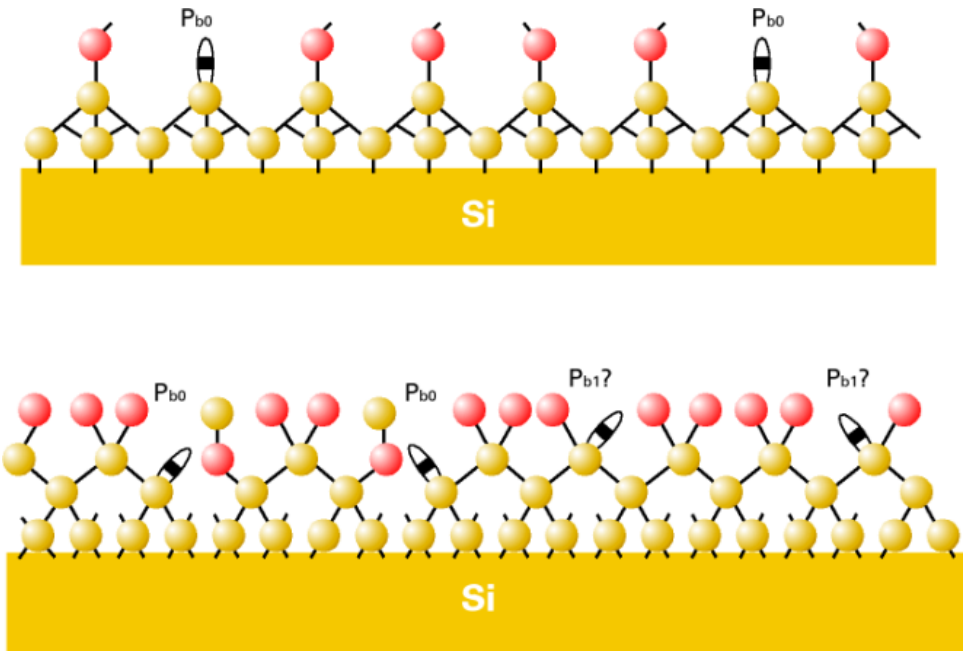

Figure 13: P_b-centers at Si/SiO_2 interface.

atom. Papers[28, 29] have shown that there are two possible reactions:

$$H^+ + Si \equiv Si - H \longrightarrow H_2 + Si \equiv Si^+ \tag{2}$$

or,

$$H + Si \equiv Si - H \longrightarrow H_2 + Si \equiv Si\cdot \tag{3}$$

$$Si \equiv Si\cdot + \text{hole} \longrightarrow Si \equiv Si^+ \tag{4}$$

A recent paper[30] shows that Eq. 2 is the only possible reaction. The buildup of interface traps is dependent on the applied electric field and temperature, with higher rates at higher positive fields and higher temperatures.

The radiation induced interface traps degrade the mobility of the carriers in the channel of the MOS device and lead to a reduction in channel conductance and transconductance. This degradation has been parameterized[31, 32] over a wide range of experimental conditions and is given by :

$$\mu = \frac{\mu_0}{1 + \alpha \Delta N_{it}} \tag{5}$$

where μ_0 is the pre-irradiation value of carrier mobility, α is an empirical constant, and ΔN_{it} is the increase in interface traps. This mobility model is implemented in the device simulator discussed in Chapter VI.

Field oxides used to isolate MOS devices, inclusive of isolation layers used in SOI technology, all suffer the same type of changes described in the above sections. These changes result in parasitic leakage currents that must be correctly described in models used for radiation analysis.

Summary

The major effect associated with total-ionizing-dose irradiation of electronic materials is that of trapped charge buildup, which induces internal space-charge fields that may interfere with the designed operation of semiconductor devices. The problem is primarily associated with the insulating films used in manufacturing integrated circuits.

In Chapter III, we will explore the basic properties of amorphous silicon dioxide, and discuss defects that contribute to the radiation response of MOS technology.

CHAPTER III

AMORPHOUS SILICON DIOXIDE

Introduction

Amorphous silicon dioxide (a-SiO_2) has been, and continues to be, the dominant insulator in silicon integrated circuits. It is easily obtained through thermal oxidation of silicon, or Chemical Vapor Deposition (CVD) of silicon, and offers an excellent transition between the crystalline structure of the silicon device layer and the amorphous structure of oxide, due to the structural flexibility of the amorphous network.

a-SiO_2 has a well-defined local structure with four oxygen atoms arrayed at the corners of a tetrahedron around a central silicon atom. The bond angles around O-Si-O are essentially the tetrahedral angle of 109 degrees. The average Si-O bond distance is 1.61 Å with variations on the order of 0.1 Å. The oxygen atoms are electronegative, with a value of 3.4, supporting the transfer of some of the silicon valence electron density to the oxygen tetrahedron neighbors, as the silicon has a lower electro-negativity of 1.9.

It is the oxygen bridge bonds, Si-O-Si, that give a-SiO_2 many of its properties. The bond angle for Si-O-Si is nominally about 145 degrees, but can vary from about 100 to 170 degrees with very little change in bond energy with an almost completely free rotation of the bond about the axis. Some of the properties of a-SiO_2 are summarized in Table 1.

Table 1: a-SiO_2 properties.

Density	2.0–2.3 g/cm^3
Bandgap	$\sim$8.9 eV
Breakdown field	$> 1.0 \times 10^{17}$ V/cm
Thermal conductivity	0.01 W/cm-K
Thermal diffusivity	0.009 cm^2/sec
Coefficient of thermal expansion	0.5 ppm/K
Refractive index	1.46
Dielectric constant	3.9

In this chapter the basic properties and defects within the a-SiO_2 structure will be discussed. A method will be introduced to relate manufacturing conditions to the generation of defects within the volume of a-SiO_2.

Oxide Growth

Process steps to form oxide vary. A brief introduction to growth methods is presented. This introduction presents the complexity of processing. Temperature plays a key role as its profile (ramp-up, stable, ramp-down) is used in our algorithm to calculate defect concentration.

Oxide Growth Processes

Thermal Oxides

Thermal a-SiO_2 is typically grown at temperatures in the range of 800-1100°C. This use of high temperature for oxidation of silicon facilitates the breaking of Si-Si bonds. A typical growth cycle includes annealing steps at high temperatures, and at low oxygen (or no oxygen) pressure in order to reduce fixed charge. The Post Oxidation Anneal (POA) often includes H_2 to passivate interfacial defects at the Si/a-SiO_2 interface.

The high growth temperatures have the unwanted processing effect of enhanced dopant diffusion. The broadening of dopant profiles may be on the order of micro-meters which, with today's MOS channel lengths of 0.1 μm, is an issue of concern. Semiconductor manufacturing processes carefully control thermal budget for this very reason.

The presence of water (H_2O) in the oxidizing ambient facilitates the breaking of dangling bonds, and speeds up the oxidation of Si to produce an a-SiO_2 layer more rapidly. Since the solubility of water in a-SiO_2 is about three orders of magnitude higher than that of O_2, oxidizing by "bubbling" O_2 gas through hot water allows higher oxidation rates. Another fast production technique for a-SiO_2 is exposing Si to 700-1000°C pyrogenic steam, made by burning hydrogen in an oxygen ambient. These rapid oxidation techniques are advantageous when thick field oxides are to be grown.

The quality of the oxide, in terms of defect density, is process dependent[2, 18]. The sequences of dry/wet/dry, the temperature profile, and the assisting gas flow rates and pressure profiles all impact the quality of oxide. The use of POA, and the use of gases like nitrogen, hydrogen, chlorine, fluorine, and argon all play a part in determining the final quality of the oxide. These oxidizing ambients are used to improve interfaces, dielectric strength, or reduce interfacial roughness[33].

Deposited Oxides

Oxide films can also be deposited. Numerous techniques have been developed, such as sputtering, high-density plasma (HDP) Chemical Vapor Deposition (CVD), sub-atmospheric and atmospheric pressure CVD with TEOS/O_3 chemistry, low-pressure CVD with TEOS/O_2 chemistry, or Electron Beam Deposition. The advantages of deposited oxides are: 1) the process temperatures can be limited to a few hundred degrees centigrade lower than in the thermal oxidation of silicon, 2) fast film growth, and 3) the flexibility to control density, chemical compositions, and stress.

Deposited oxides are used as isolating, masking, or protecting layers, or as charge storage films in non-volatile memory cells. Deposition of a few nanometers of oxide on top of a thermal gate oxide may significantly improve the dielectric strength of the film by disrupting micro-pores, which thread through the oxide[34, 35, 36]. Quality at the interface between the thermal and the deposited oxide can be controlled by re-oxidizing in an oxygen atmosphere.

In certain process designs, such as shallow trench isolation, the deposited SiO_2 may be separated from the silicon substrate only by a thin layer of a thermal oxide. The deposited film can be a source of stress, which can lead to the formation of defects and deterioration in reliability of the oxide.

Growth by Oxygen Implantation

For completeness, and because of its use as a buried isolator, we will also mention the formation of an a-SiO_2 layer by implantation of oxygen into a silicon wafer. The implanted oxygen dopant concentration profile has a Gaussian shape with its peak distance determined by the energy of the implant. A high temperature ($\sim$1350°C) anneal allows the oxygen atoms to react with the silicon to form a buried oxide layer around the peak of the implant. This process is known as Separation by IMplantation of OXygen (SIMOX).

Defects in a-SiO_2

Independent of the process of oxide growth, defects will be present in the material due to thermodynamic constraints like Gibbs free energy. Defects in a-SiO_2 can be classified into two categories: intrinsic and extrinsic. For electronics one is interested in those defects that are electrically active[37].

Intrinsic Defects – The Oxygen Vacancy (V_o)

The oxygen vacancy is, without a doubt, the most studied defect in a-SiO_2 [38, 39, 40, 41, 42]. A simple model of this electrically active defect in its neutral state is given by Eq. (6):

$$O_3 \equiv Si - Si \equiv O_3 \tag{6}$$

The defect is made up of two neighboring tetrahedra whose bonding oxygen atom is missing. The behavior of this defect, when presented with a hole, is to trap the hole, and become a positively charged center. This trapping is represented by Eq. (7):

$$O_3 \equiv Si - Si \equiv O_3 + h^+ \longrightarrow O_3 \equiv Si\bullet \quad {}^+Si \equiv O_3 \tag{7}$$

The V_o center is also reported to be able to trap an electron[20], as described by Eq. (8):

$$O_3 \equiv Si - Si \equiv O_3 + e^- \longrightarrow O_3 \equiv Si - \bullet - Si \equiv O_3 \tag{8}$$

For a predictive model of radiation-induced oxide charging one needs to relate oxide processing conditions to the concentration of oxygen vacancies, the precursor to E′ defect centers induced by radiation.

Lenahan *et al.*[18] introduced a predictive model for radiation-induced oxide charging based on statistical thermodynamics (Appendix D) and electron spin resonance measurements of E′ defect centers. This work assumes that the dominant hole traps in thermally grown a-SiO_2 are from the family of E′-centers.

Lenahan *et al.*'s efforts established a link between process conditions and intrinsic defects in terms of thermodynamics and the oxide growth experiments necessary to calculate S_F and H_F used in the expression for the concentration of intrinsic defects:

$$C_v = \exp\left(\frac{S_F}{k}\right)\exp\left(-\frac{H_F}{kT}\right) \tag{9}$$

This expression needs S_F and H_F calculated for each process using the experimental suite described in[18] and a method to calculate the temperature T. Our work concentrated on the analysis of oxide growth temperature profiles and the algorithm required to calculate T. This work allowed the implementation of an algorithm that is standalone and integrated into Silvaco's process simulator. The Temperature Profile Module (TPM) allows direct input of temperature profile or can

use read a process description file used for process simulation. The TPM weighs the temperature based on time spent at that temperature to obtain a weighted average temperature that the oxide is exposed to during processing. The temperature algorithm takes into account the proportional relevance of each component of ramp-up, hold, and ramp-down processing temperatures as well as later annealing exposures in the integrated process flow.

Our work uses the same foundry as Lenahan *el al.*[18], the SPAWAR System Center, San Diego, California. This allows us to use their experimentally calculated values of $\exp(S_F/k)$ and H_F, which are 4.8×10^{18} and 1.5 eV respectively.

Using the TPM and the experimental calibration data we are now able to estimate the concentration of E′-center pre-cursors, the intrinsic oxygen vacancy defect, using the expression:

$$[\text{Family of E}'\text{-center precursors}] = 4.8 \times 10^{18} \exp\left(-\frac{1.5}{kT}\right) \tag{10}$$

The [Family of E′-center precursors] will be used later in the device simulator. Using our results from *ab initio* simulations, the [Family of E′-center precursors] will be partitioned into the specific defect type as percentage of occurrences.

A statistical analysis of the behavior of oxygen vacancies in the presence of free carriers (electrons and holes) will be presented in Chapter IV using four representative amorphous structures.

Extrinsic Defects - Hydrogen Related

Hydrogen is ubiquitous in the semiconductor manufacturing process. The presence of hydrogen in oxide can create new defects and passivate existing ones. One example is an E'_β center given by Eq. (11). This defect starts as a neutral Vo center that is diamagnetic and is transformed to a neutral paramagnetic center by atomic hydrogen.

$$O_3 \equiv Si - Si \equiv O_3 + H \longrightarrow O_3 \equiv Si\bullet \quad H - Si \equiv O_3 \tag{11}$$

In Chapter V, results will be presented for interaction of defects with hydrogen in neutral atomic and molecular form, and as a proton.

Examination of Defect States

One would like to explore defects in various local structural arrangements representative of those grown by the methods described above. In this exploration, one hopes to gain an understanding of these defects in terms of their energy states, the percentage or probability of this energetic

defect state, and their associated electrical behavior as determined by their capture cross sections for carriers. These results will then flow into our device simulation discussed in Chapter VI.

The study of defects in amorphous SiO_2 (a-SiO_2) may be addressed by *ab initio* calculations on a-SiO_2 cells using density functional theory (DFT)[43]. Unlike conventional quantum theory in which the system's ground state energy is calculated as a function of many electron wave functions, DFT calculates the system energy as a function of the electron density. The significance of this ground state energy calculation is that nearly all physical properties of a system can be related to its total energy, and systems can be compared through the difference between their total energies, E(N), where N represents the number of electrons for the system under consideration in its neutral charge state. The use of electron density to describe the system's properties in DFT allows one to separate the Schrödinger equation for a many-electron system with interacting electrons into a set of independent one-electron Schrödinger equations. The details of the DFT-based approach can be found in Appendix A.

The geometry of the system is selected such that both long and short range environments of the defects under investigation can be taken into account with the same level of accuracy. The computational advantage in this approach is that periodic boundary conditions allow the electron wavefunctions to be expanded in terms of plane waves.

Definition and Classification of Defects as Traps

The intrinsic and extrinsic defects introduced above are associated with energy levels or states within the bandgap having electrical behaviors determined by position within this bandgap.

It is often convenient to define defects as "shallow" or "deep" states. In this work, shallow states are arbitrarily defined to be within 1 eV of a band, either conduction or valence[2]. Thus, trap states within 1 eV of the valence band are termed shallow hole traps or deep electron traps while trap states within 1 eV of the conduction band might be termed shallow electron traps or deep hole traps.

A trap state is characterized for device simulation by establishing its concentration per unit volume (N_{Defect}), its energy level (E_{Defect}), the spatial distribution, and the ability of this trap to capture a carrier, given as capture cross-sections, σ_p or σ_n, for hole and electron capture, respectively[2]. The units of capture cross section of a defect state are generally cm^2.

Capture Cross Section Estimation

The capture cross section of a defect for an electron, (σ_n) or for a hole (σ_p) can be thought of as the area of a target that a carrier must hit to be captured in a trap state. Defects create a perturbation of the local electrostatic field and the corresponding potential. In other words, estimation of the capture cross section involves the calculation of the size of the target area that the defect presents to a carrier. This target area has thermal, coulombic, and electric field dependence. Assume for a moment that the target area for probable capture is circular. In this case, the capture cross-section for a carrier ($\sigma_{capture}$) can be represented by Eq. (12):

$$\sigma_{capture} = \pi R^2_{capture}. \tag{12}$$

$R_{capture}$ is the radius of the circular target.

As a free carrier moves within a-SiO_2, a mean free path is associated with the travel. This statistically determined free path is the average distance between scattering events. If, while traveling on this path, a carrier approaches the capture radius ($R_{capture}$) of the trap, then capture is probable. The trapped carrier will lose energy either through a radiative or non-radiative transition. In a radiative transition, energy is converted to light. In a non-radiative capture, the energy is converted to heat.

In the Auger process, the energy is dissipated through carrier-carrier interaction. The carrier loses its energy by transferring it to another electron or hole, and the carrier is captured by the defect state. In a phonon process, the carrier energy loss process is by a one-phonon interaction, possibly followed by a transition down a ladder of available states, or through lattice distortion upon transition to the defect state[44]. The result of trapping a carrier at the defect site involves electrostatic perturbation and lattice distortion to conserve this energy.

Once captured, a carrier must lose its energy, which is of the order of the difference between total energy states of the untrapped and trapped states. To estimate the defect site's ability to trap/capture electrons or holes, the difference in energy was calculated for the charged state (E(N+1)), representing the cell capturing an electron and obtaining a negatively charged state and, E(N-1) representing the cell capturing a hole and obtaining a positively charged state. This estimation represents a non-radiative transition to a new state. Eqs. (13) and (14) define the electron

and hole energy differences, $\Delta E(N+1)$ and $\Delta E(N-1)$, respectively.

$$E_{\text{delta,electron}} = \Delta E(N+1) = [E(N)_{\text{bulk}} + E(N+1)_{\text{defect}}] - [E(N+1)_{\text{bulk}} + E(N)_{\text{defect}}] \tag{13}$$

$$E_{\text{delta,hole}} = \Delta E(N-1) = [E(N)_{\text{bulk}} + E(N-1)_{\text{defect}}] - [E(N-1)_{\text{bulk}} + E(N)_{\text{defect}}] \tag{14}$$

Here, $E(N)_{\text{bulk}}$, $E(N-1)_{\text{bulk}}$, and $E(N+1)_{\text{bulk}}$ denote the total energy of the neutral, positively and negatively charged cells of the bulk (defect free a-SiO_2) structures. Similarly, $E(N)_{\text{defect}}$, $E(N-1)_{\text{defect}}$, and $E(N+1)_{\text{defect}}$ denote the total energy of the neutral, positively and negatively charged a-SiO_2 structures with a defect. The neutral defect cell is capable of capturing an electron or a hole if the corresponding delta energies are negative, indicating a net energy lowering of the cell after capturing the charge carrier.

Using Eqs. (13) and (14) to estimate E_{delta} and a simple quantum well model of a neutral defect potential[45], R_{capture} can be estimated using Eq. (15) and substituted into Eq. (12), giving Eq. (16).

$$R_{\text{capture}} = \frac{\hbar}{\sqrt{2mE_{\text{delta}}}} \tag{15}$$

$$\sigma_{\text{capture}} = \pi R_{\text{capture}}^2 = \frac{\pi\hbar^2}{2mE_{\text{delta}}} \tag{16}$$

Eqs. (15) and (16) form the basis for estimation of capture cross section for neutral defect states in Chapters V and VI. In the next chapter we will examine the statistical nature of the oxygen vacancy defect. This study will explore the structural variation of defects and the energy distribution of these defects. The device simulator will then take a spatial and energy distribution with the calculated σ_{capture} as applied through differential equations to be discussed in Chapter VI.

Summary

This chapter describes the process used to calculate the concentration of defects within an oxide for given processing conditions and the method used to calculate the capture-cross section of a defect. With the algorithm implemented within our process simulator for the calculation of

the concentration of defects, given a process temperature profile, one can now explore the defect structure and energy distributions within the bandgap of the oxide. The results will also provide E_{delta} for the estimation of $\sigma_{capture}$. We examine intrinsic defects in the next chapter.

CHAPTER IV

INTRINSIC DEFECTS: OXYGEN VACANCIES

Introduction

Oxygen vacancies have long been known to be the dominant intrinsic defect in amorphous SiO_2 [46, 41, 47]. They exist, in concentrations dependent on processing conditions, as neutral defects in thermal oxides without usually causing any significant deleterious effects, with some spatial and energy distribution. During irradiation they can capture holes and become positively charged E′ centers[25], contributing to device degradation. Over the years, a considerable database[46, 25, 48, 39, 49, 50] has been amassed on the dynamics of E′ centers in bulk SiO_2 films, and near the interface under different irradiation and annealing conditions. Theoretical calculations[51, 52, 53] so far have revealed the basic properties of prototype oxygen vacancies, primarily as they behave in either a crystalline quartz environment, or in small clusters that serve as a substitute for a real amorphous structure. To date at least three categories of E′ centers, existing at or above room temperature, have been observed in SiO_2 [54]. The unifying feature is an unpaired electron on a threefold coordinated silicon atom, having the form $O_3 \equiv Si\bullet$. Feigl *et al.*[49] identified the E_1' center in crystalline α-quartz as a trapped hole on an oxygen vacancy, which causes an asymmetrical relaxation, resulting in a paramagnetic center. The unpaired electron in the E_1' center is localized on the threefold coordinated Si atoms, while the hole is localized on the other Si atom.

This model was improved by Rudra and Fowler[55] to include the stabilization of this relaxation by the Si atom back-bonding to an O atom. This oxygen atom is now threefold coordinated, while the puckering Si atom is once again fourfold coordinated, as depicted in Fig. 14. It is this structure that has been the center of many theoretical calculations using cluster[54, 51] and supercell[29] approaches. The E_1'-center, in crystalline α-quartz, has a counterpart in a-SiO_2, the E_γ'-center. The E_γ'-center is identical in behavior to the E_1'-center, exhibiting an electron paramagnetic resonance (EPR) g-tensor signature, g_{11}=2.0018, g_{22}=2.0006 and g_{33}=2.0003[46, 56].

Another variant of the E′-center is the E_δ'-center discovered by Griscom and Friebele[57]. The g-tensor values obtained from EPR for this defect are g_{11}=2.0018, g_{22}=g_{33}=2.0021[58]. This sig-

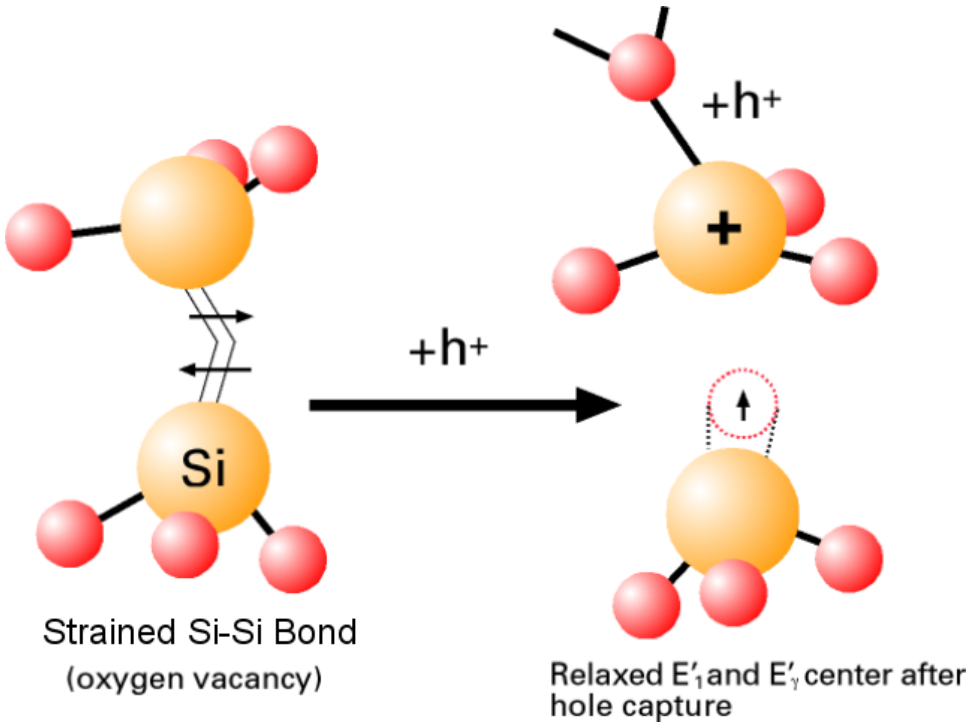

Figure 14: The model of the E'_1 and E'_γ centers in crystalline α-quartz and amorphous SiO_2.

nature suggests that the unpaired electron is not localized on a single Si atom. Recent theoretical calculations using clusters by Chavez *et al.*[52]have supported that the lone electron is shared by the two silicon atoms involved in the defect, as depicted in Fig. 15. This positively charged dimer configuration increases the Si–Si bond distance upon hole capture, as the Si atoms symmetrically relax. Theoretical calculations suggest that the Si–Si bond distance in E'_δ-centers varies around 2.6 ± 0.1 Å[59].

In this chapter, we will discuss the analysis of a population of oxygen vacancies in amorphous SiO_2 networks using first-principles calculations based on Density Functional Theory (DFT)[60, 61, 62], in an attempt to improve models for spatial and energy distributions of defects for use in a device simulator. In particular, we find that there is a variant of the E'_γ-center behavior that depends on the local topology. In addition we find that the E'_δ-center configuration supports a distribution of Si–Si bond distances from 3.0 to 4.4 Å. This distribution of Si–Si bond distances results in energy levels between 0.5 and 1.0 eV above the valence band and a small group at 2 ± 0.1 eV above the valence band when the Si–Si bond distance is stretched to greater than 4.0 Å.

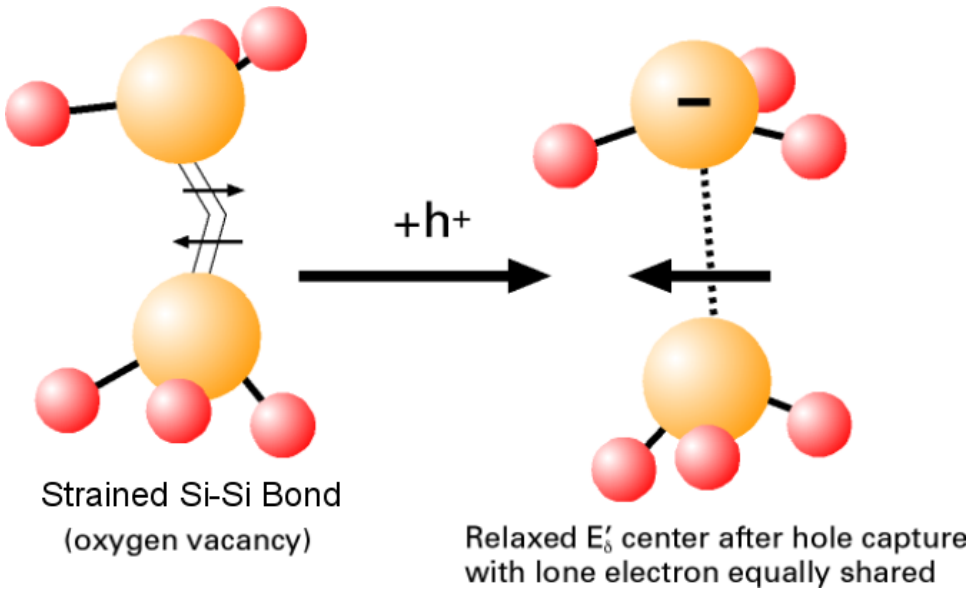

Figure 15: The model for an E'_{δ}-center in amorphous SiO_2.

Theoretical Analysis

The study of a population of oxygen vacancy defects in amorphous SiO_2 (a-SiO_2) was addressed by *ab initio* calculations on a-SiO_2 cells using DFT[63].

The calculations reported here were performed using the Generalized Gradient Corrected local-density approximation (PW-91)[60, 64]. Electronic minimization was accomplished using the conjugate-gradient (CG) algorithm with plane-wave cutoff energy of 380 eV, and ultrasoft pseudopotentials. Integrations over the Brillouin zone were done using four special k-points[60] in the irreducible wedge. The examination presented here was performed using four initial defect-free amorphous SiO_2 (a-SiO_2) structures, S_1 through S_4. The supercells were created using the Cerius-2 molecular dynamics code from Accelrys Inc. guided by references[65, 66]. The number of atoms in the classical simulation supercells varied from 72 to 576 atoms. All supercells were relaxed using *ab initio* methods after construction.

The periodic structures used in our DFT calculations consist of a base 72-atom unit cell, with volume and density properties given in Table 2.

Density and volume variations allow for the type of structural variation that might occur in any finite volume, noting that a macroscopic a-SiO_2 sample contains a very large number of local atomic configurations. The structures were confirmed to be representative of a-SiO_2, by comparing their behaviors with the results reported by M. Boero *et al.*[67].

Table 2: Volume and density properties of the four a-SiO_2 structures used in this study of defects.

Structure	**Density** (g/cm^3)	**Volume** ($Å^3$)
S_1	2.06	1160.9
S_2	1.99	1197.4
S_3	2.04	1173.6
S_4	2.13	1122.9

To perform an investigation of the microstructure of oxygen vacancies in a-SiO_2, we randomly generate oxygen vacancies in the four a-SiO_2 structures by removing an oxygen atom. After removal of the selected oxygen atom, the cell was allowed to relax, forming the $O_3 \equiv Si - Si \equiv O_3$ dimer configuration. This ground state defect structure has a total energy, E(N), where N is the neutral number of valence electrons for a given arrangement of atoms within the cell. This process was repeated for different oxygen atoms in each amorphous cell, creating a population of one hundred twenty (120) oxygen vacancy structures in which defect energy states were examined. This relaxation was achieved with a plane wave cut-off of 380 eV, an energy change of 0.0001 eV/atom, an RMS force of 0.15 eV/atom, and an RMS displacement of 0.01 Å/atom.

This population of neutral oxygen vacancies was examined in positive and negative charge states by subtracting or adding an electron, and allowing the structure to relax. The same criterion was used in the neutral structure to produce total energies of E(N-1), and E(N+1) respectively.

The calculation of percentages was accomplished using the number of occurrences divided by the population of oxygen vacancies (120) multiplied by 100 and rounded to the nearest integer.

Orbitals, Energies, and Energy Levels

The molecular orbitals are occupied from the lowest up until one runs out of electrons. The meaning of the empty orbitals is that they would be the next available energies and distributions of the next electron if another were added. The density functional framework has no simple and reliable method for the estimation of electronic excitation energies. The importance of excitation energies derives from the existence of a large body of experimental spectroscopic data and also from the fact that they contain information on the electronic dynamics.

The Kohn-Sham Lagrange multipliers (see Appendix A) ε_i are not excitation energies as are

the orbital energies of Hartree-Fock theory. Instead, they reflect the response of the total electronic energy to changes in occupation number (n_i), i.e.,

$$\frac{\partial E}{\partial n_i} = \varepsilon_i \tag{17}$$

This equation implies that a knowledge of the ε_i provides information about the electronegativity of the system. Indeed, the electronegativity can be obtained from $\varepsilon_{\mathrm{HOMO}}$ and $\varepsilon_{\mathrm{LUMO}}$. Although no Koopmans'-like theorem exists in Kohn-Sham theory, excitation energies can be derived from the ε_i. For instance, the first ionization energy can be found from:

$$-I = E_N - E_{N-1} = \int_0^1 \varepsilon_{\mathrm{HOMO}}(n)dn \tag{18}$$

Slater (see Appendix A) has derived useful numerical approximations to this expression, namely:

$$-I \approx \varepsilon_{\mathrm{HOMO}}\| \left(n = \frac{1}{2}\right) \tag{19}$$

That is, the first ionization energy is found by removing $\frac{1}{2}$ an electron from the highest occupied Kohn-Sham molecular orbital. Similarly, the electron affinity is given by:

$$-A = E_{N+1} - E_N = \int_0^1 \varepsilon_{\mathrm{LUMO}}(n)dn \tag{20}$$

which may be approximated by:

$$-A = \varepsilon_{\mathrm{LUMO}}(n = \frac{1}{2}) \tag{21}$$

where $\frac{1}{2}$ an electron has been added to the LUMO, the lowest occupied Kohn-Sham molecular orbital.

The simplest DFT scheme for the computation of excitation energies (and in particular, electron removal energies), has been the evaluation of the total energy difference between the initial and final states. For all energy states described within this dissertation we will use this method. Energy states will represent the difference between the initial and final states mapped from the valence band edge.

Theoretical Results

The analysis described above found three categories of oxygen vacancy behaviors, which are now described:

Category 1

The oxygen vacancies in all the amorphous cells studied had a dimer configuration in their neutral state, E(N). Approximately eighty percent (80%, 96 out of 120) of the population maintained this dimer configuration in their positively charged state, E(N-1). These cells that have a dimer configuration in both the neutral and positively charged states will be referred to as Category 1 cells (Fig. 17).

Category 1 defects can be classified into two sets depending on whether they can or cannot at least meta-stably capture an electron in the neutral state. The two sets can also be distinguished in terms of the Si–Si bond distances, and energy levels in the positively charged state. The set of Category 1 defects that could not capture an electron in the neutral state had Si–Si distances ranging from 2.5 to 3.0 Å in the neutral state, and from 3.0 to 4.0 Å in the positively charged state. The positively charged states of these defects introduced energy states ranging from 0.5 to 1.0 eV above the valence band. On the other hand, the set of Category 1 defects which could capture an electron in the neutral state had Si–Si distances ranging from 3.0 to 3.2 Å in the neutral state, and from 4.0 to 4.4 Å in the positively charged state. The positively charged states of these defects had energy levels at 2.0 ± 0.1 eV above the valence band. The properties of the subsets of Category 1 defects described above are summarized in Table 3.

Table 3: Category 1 defects can be classified in two sets depending on their ability to capture an electron in the neutral state.

	Cannot Capture Electron	Can Capture Electron
Si–Si Bond Length, E(N)	2.5–3.0Å	3.0–3.2Å
Si–Si Bond Length, E(N-1)	3.0–4.0Å	4.0–4.4Å
Energy Levels, E(N-1)	0.5–1.0eV	1.9–2.1eV

The deep positive states are a result of local structure, in that the silicon atoms relax asymmetrically. One of the relaxing Si atoms has void space into which to relax. This can be seen in Fig. 16. These dimer states, with neutral Si–Si bond distances between 3.0 and 3.2 Å, exhibited an ability to capture an electron in a state near the midgap.

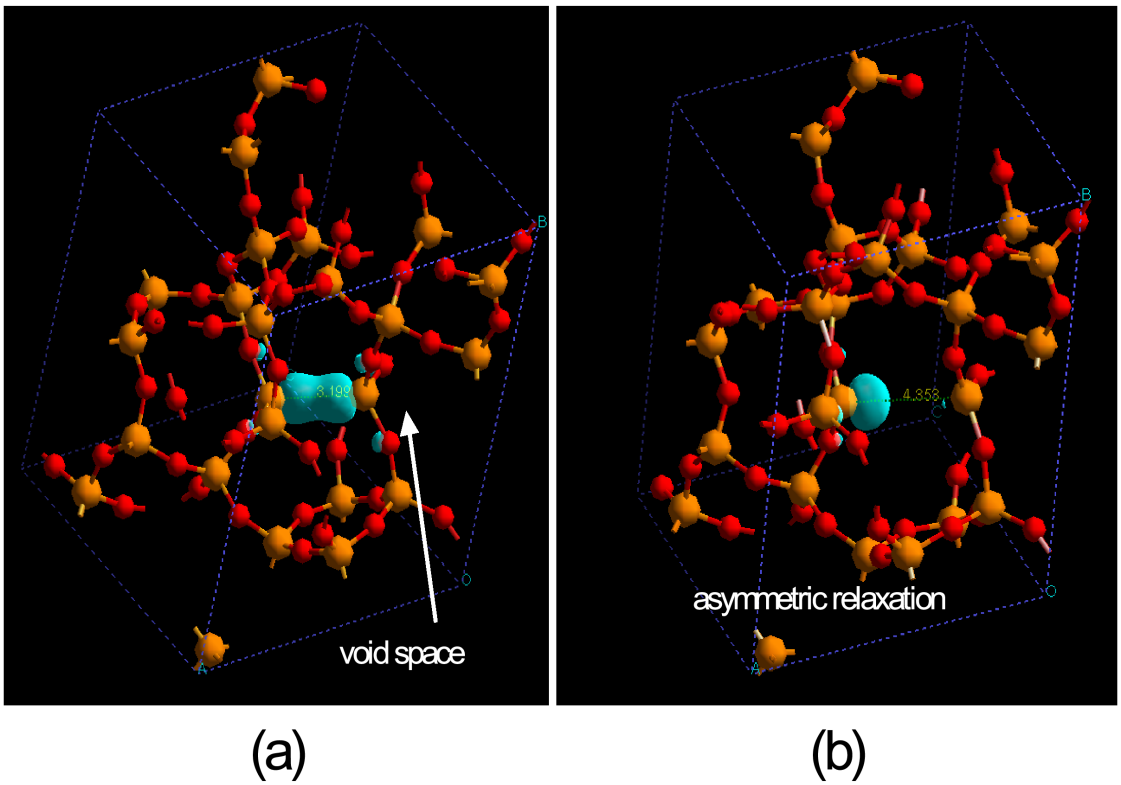

Figure 16: An oxygen vacancy in a) neutral dimer configuration with a Si–Si bond of 3.2 Å, and b) an E'_δ with the electron localized due to asymmetric relaxation. The orange atoms are Si and the red atoms oxygen. The light blue cloud represents the electron orbital.

Category 2

Category 2 cells comprise ten percent (10%) of the population of oxygen vacancy centers. They have a dimer configuration in the neutral state, which puckers in the positively charged state with significant lattice relaxation (Fig. 17). One of the Si atoms relaxes back past the plane defined by its three oxygen neighbors, and bonds with another network oxygen atom. This oxygen atom now becomes threefold-coordinated, whereas the puckered Si atom becomes fourfold-coordinated. This structure is known as an E'_γ-center. This positive charge state is approximately 4.3 eV from the valence band. When an electron is given back to this center, it stays in a puckered configuration with an energy barrier for Si–Si bond reformation spanning 0.5 to 1.2 eV, as calculated by incrementally moving the Si–Si atoms along the bond line, and plotting the difference in total energy. In fact, the electron goes to fill the dangling bond, whereas the hole is still left on the puckered Si side. The resulting dipole separation can be as large as 5 Å in the structures we have examined.

This neutral dipole configuration, upon capturing a hole, provides a positive defect state around 3.5 eV above the valence band.

The Category 2 structure also has the ability to capture an electron, having a state upon electron capture at $\sim$ 4.4 eV above the valence band. However, the neutral dipole state, upon capture of an electron, has a state $\sim$ 5.6 eV above the valence band. This behavior is consistent with the work of Walters and Reisman[68], in that the second electron is captured by the puckered Si atom.

Category 3

The other ten percent (10%) of the examined population of oxygen vacancy centers are unstable after electron capture, and represent Category 3 defects. In the positively-charged state, the puckered Si atom now bonds both to a network oxygen and a network Si atom, becoming fivefold-coordinated with the localized positive state at $\sim$ 3.8 eV (Fig. 17). When an electron is given back to this center, it collapses immediately to the dimer configuration without an energy barrier. This neutral defect type did not demonstrate the ability to capture an electron.

Discussion

The cumulative electrical energy states of the studied oxygen vacancies are summarized in Fig. 18. These electrical states are determined from the difference of the total energies of charged and neutral structures.

The Category 1 defects map to the structural behavior usually associated with an E'_δ-center, exhibiting a sharing of the electron between Si atoms involved in the oxygen vacancy defect. The calculated distribution of shallow E'_δ-centers spanning 0.5 to 1.0 eV is responsible for the temporal dispersion of the hole transport through a-SiO_2 after exposure to ionizing radiation or high-field stress. The emission times for the trapped holes is expected to be on the order of $\exp(-E_T/kT)$[69, 70], where E_T is the trap energy in eV.

The ability of some neutral E'_δ precursor centers to achieve a positive dimer state with the localization of the lone electron on just one of the Si atoms has not been reported before. This localization is seen in 20% (19 out of 96) of the Category 1 dimers with a neutral Si–Si bond distance of approximately 3.0 Å and greater than 4.0 Å upon capture of a hole. These positive charge states

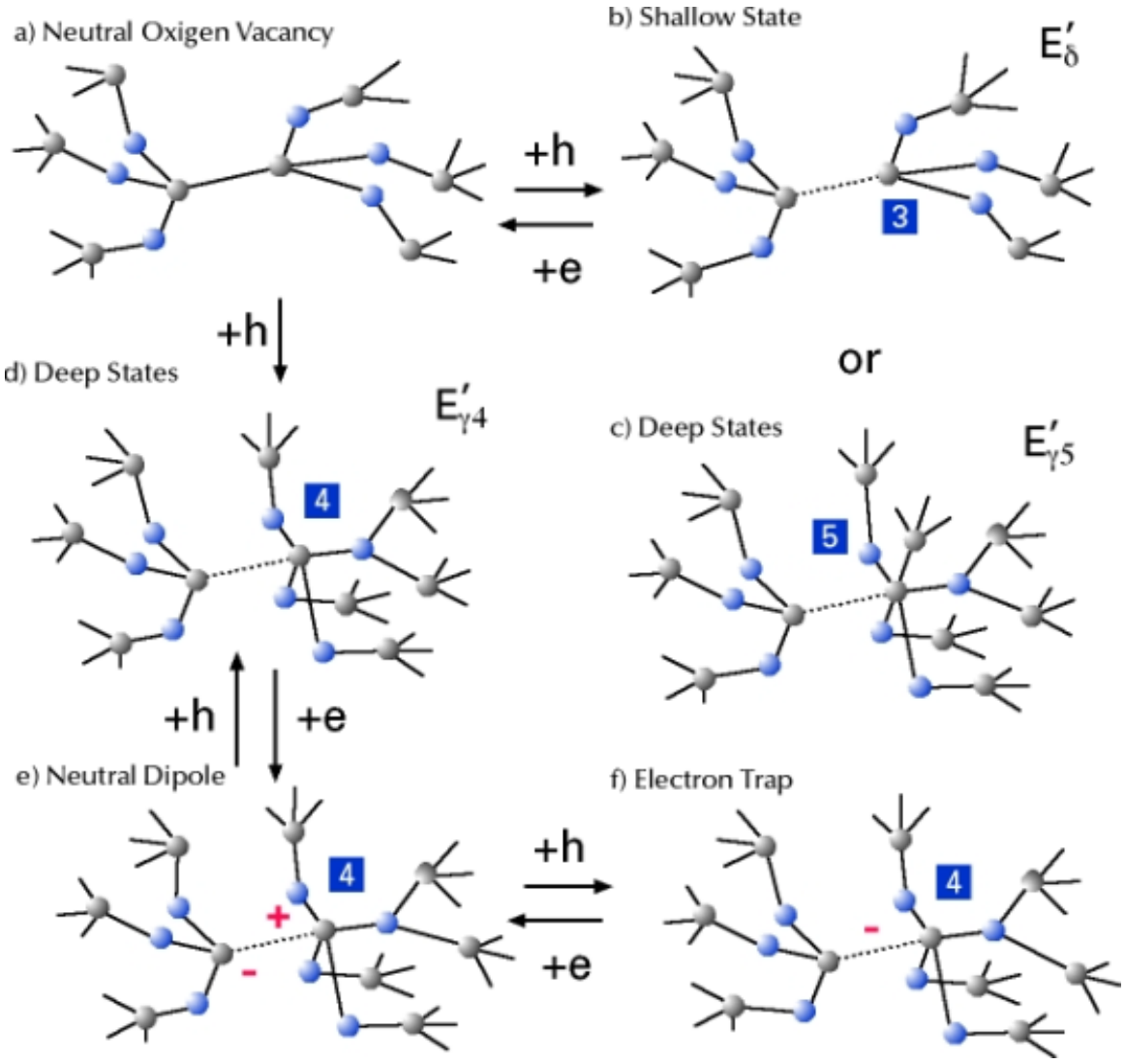

Figure 17: State diagram of oxygen vacancies charged state behavior. The numbers (in squares) represent the coordination of the silicon atom.

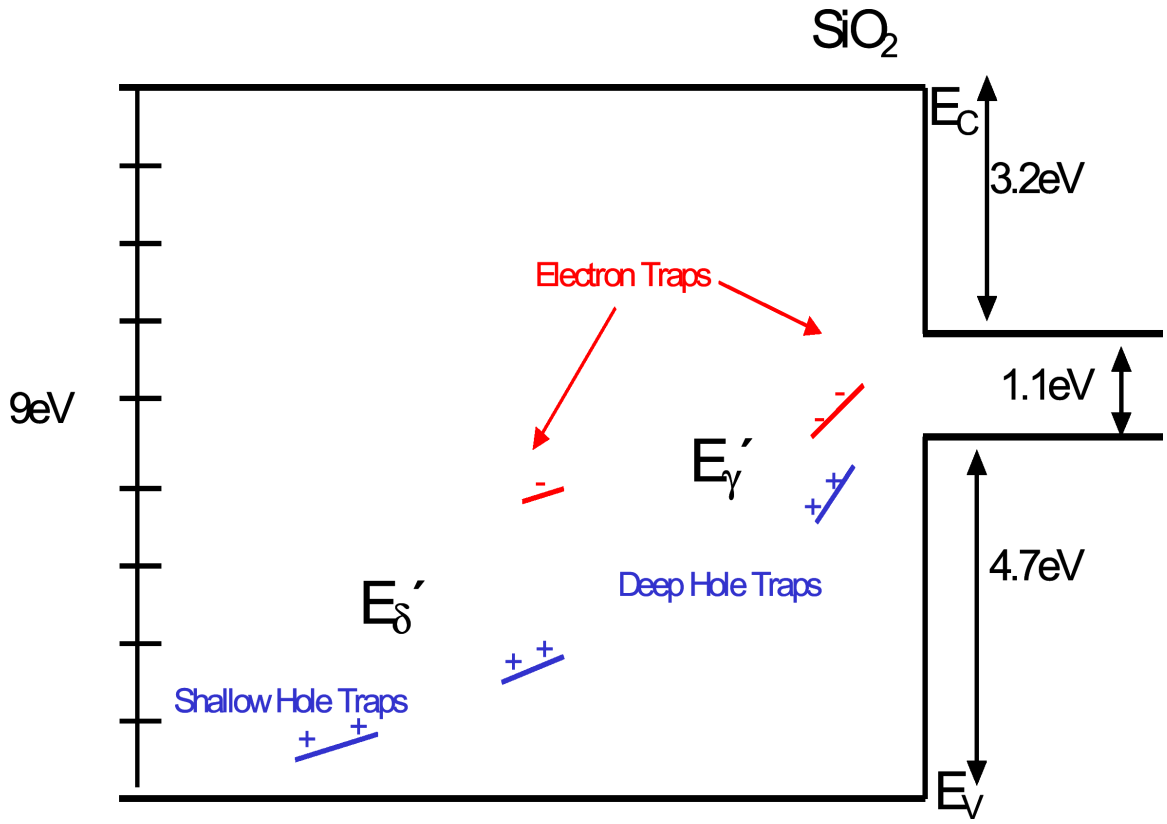

Figure 18: The electrical state energy distribution of E'_{δ} and $E'_{\gamma 4}$-centers are shown in blue, while the electron trap states are in red. The lines under the charges represent the distribution of energy levels.

are deep, being centered at 2 ± 0.1 eV. These deep positive dimer defects have structural void space behind the Si atoms involved in this oxygen vacancy. This void space prevents this structure from relaxing symmetrically upon hole capture, as in the other dimer states. The increased Si–Si distance, and asymmetric relaxation, allows for deeper positive states.

It is these neutral dimer structures, with a larger neutral Si–Si bond distance (~ 3.0 Å) and void space due to local arrangement behind relaxing Si atoms, that also provide an electron trapping capability. These defect sites, upon capture of an electron, provide a negative charge state at approximately midgap. If spatially located near the Si/SiO_2 interface, this defect type provides states to exchange electrons with the silicon. The transitions of electrons and holes between band states and bound states is a contributor to low frequency noise. This exchange could be one source for 1/f noise[71].

The two types of puckering structures, the $E'_{\gamma 4}$-center for the four-fold coordinated, and the $E'_{\gamma 5}$-center for the five-fold coordinated structure, described by Categories 2 and 3 respectively, exhibit different responses after electron capture. The Category 2 type, the $E'_{\gamma 4}$-center with a four-fold Si configuration, remains puckered after capturing an electron. This electron is captured on the Si atom not involved in the pucker. Lelis et al.[72, 73] proposed a model for the charge switching dynamics of the E'_{γ}-center. They have suggested that the switching behavior is accomplished by capturing and emitting an electron from the $\equiv$ Si$\bullet$ orbital without changing the electrical structure of the positively charged ($\equiv$ Si$+$) silicon atom. As presented by Lelis[73], the capturing and emission of an electron from the $\equiv$ Si$\bullet$ orbital is supported by our results. The structural relaxation, from the neutral dimer structure, which occurs when a hole is captured, changes the structure significantly, forming a dipole that can be on the order of 5 Å in length. The variation in dipole lengths changes the dipole field.

The Category 3 type, the five-fold $E'_{\gamma 5}$-center, collapses back to a dimer configuration after capturing an electron. Hence, this defect can function as a stable hole trap, but does not form a stable dipole defect in SiO_2. With no potential barrier to reforming the dimer configuration, annealing can be accomplished by electron capture from the positively charged state.

The combined behaviors of the $E'_{\gamma 4}$ and $E'_{\gamma 5}$-centers provide a natural explanation for the varying degrees of reversibility for trapped-hole annealing in previous switching bias work[74, 73, 75, 21, 39]. Fig. 19 shows a general case of reversibility for trapped-hole annealing consistent with

the work of Conley *et al.*[39]. During these switched bias experiments, an NMOS transistor is irradiated, and its change in threshold voltage is monitored. After irradiation, the threshold change (ΔV_{tn}) is negative, as positive charge is accumulated. Upon the first positive bias application, the precursor $E'_{\gamma 4}$-centers capture electrons, tunneling in from the Si, reducing the net positive charge through the creation of neutral dipoles. As reverse bias switching anneals continue, one anneals the $E'_{\gamma 5}$-centers, reducing the net positive charge, and leaving the $E'_{\gamma 4}$-centers. The population of E'_{γ}-centers is now skewed toward $E'_{\gamma 4}$-centers. Continuing to cycle the bias conditions, the $E'_{\gamma 4}$-centers also begin to collapse as their barrier to reforming the weak Si–Si bond spans 0.5 to 1.2 eV. The net result is that V_{tn} begins to anneal, and gradually progresses toward the pre-irradiation value.

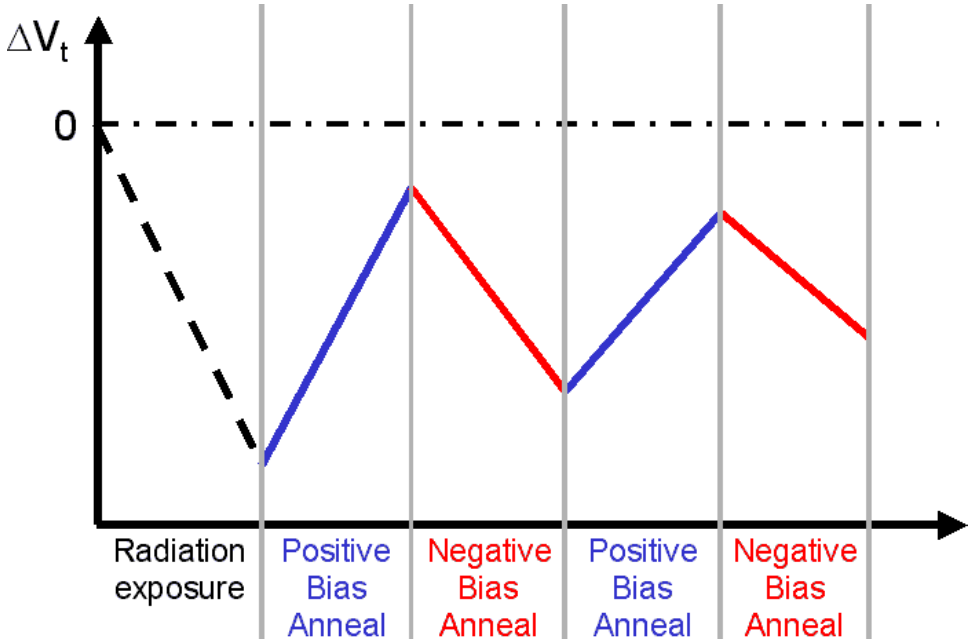

Figure 19: A general pictorial description of reverse bias switching anneals on an NMOS transistor. After irradiation the gate bias is switched repeatedly over time in an attempt to anneal the trapped positive charge in the oxide.

In the past two decades, research on radiation or high-field-stress induced defects in the amorphous SiO_2 layer of MOSFETs has revealed a broad range of complex dynamics in both the bulk oxide film and near the Si-SiO_2 interface. The origin of many of these phenomena has been traced to oxygen vacancies[2, 76]. The phenomena are often associated with the dynamics of the E'_{γ}-center, and of a second EPR-active defect that has been labeled E'_{δ} and identified as an O vacancy in the dimer configuration[54, 51]. Examples of these behaviors are as follows:

- E'_γ centers are found to be more stable thermally than E'_δ centers; at room temperature, after irradiation or hole injection, the density of E'_δ centers is nearly alway observed to decrease. In some cases, this decrease is accompanied by a corresponding increase in E'_γ centers[54].

- After irradiation or high-field stress, the accumulated positive charge in the oxide can often be neutralized by a high-temperature anneal with a large positive bias, but a reverse-bias anneal can also remove much of the positive charge[74, 72, 77]. Switched bias annealing also gradually removes positive charge as the total positive charge that gets restored during the cycling gradually decreases with repeated cycling.

Oxygen Vacancy Summary

The *ab initio* simulation study provides the following data:

a) The vast majority (∼80%) of the examined population is not bistable like O vacancies in quartz. Instead, the dimer configuration (Fig. 17(a)) is the only stable configuration in both the neutral and positively charged state. The dimer energy level containing one or two electrons is shallow (within ∼1 eV from the SiO_2 valence-band edge).

b) Roughly 10% of the examined population is bistable in the same way as an oxygen vacancy in quartz: in the neutral state, the dimer configuration is stable; in the positively charged state one of the adjoining Si atoms relaxes back past the plane defined by its three O neighbors and bonds with another network O atom; the latter becomes threefold coordinated whereas the puckered Si atom becomes fourfold coordinated (Fig. 17(b)). The localized energy level is quite deep, nearly in the middle of the SiO_2 energy gap (∼4.5 eV). When this center is given an electron back, it stays in a metastable puckered configuration, with an energy barrier ranging from 0.5 to 1.2 eV. The electron fills the dangling bond, making it negatively charged, whereas the hole, a positive charge, is still left on the puckered Si side, resulting in a dipole[78].

c) Roughly 10% of the examined population is also bistable, but with the following key differences: In the positively charged state, the puckered Si atom now bonds both to a network O and a network Si atom, becoming fivefold coordinated. The localized energy level is again deep (∼4.5 eV) and the unpaired electron has essentially the same distribution as before,

suggesting a nearly identical EPR signature. However, when this center is given back an electron, it collapses immediately to the dimer configuration without an energy barrier. This result can account for many complex dynamical phenomena associated with electron capture and release after hole trapping in irradiated or stressed SiO_2.

The wave function of the unpaired electron in the dangling bond is essentially the same in the two cases (see Figs. 17(b) and 17(c)) so that they would be indistinguishable by EPR as E'_γ. Thus, the same EPR signal corresponds to two point defects with differing structures.

The dynamics of O vacancies in irradiated or stressed thermal oxides in the context of the experimental data can be explained using the findings of this chapter. Thermal oxides usually contain significant concentrations of O vacancies. Our statistics suggest that as many as 80% of these O vacancies may be precursors of E'_δ centers. As we saw above, the holes captured in dimers have a short lifetime. Those holes that are released either get recaptured at other dimer precursor sites or at puckered-precursor sites. Since the latter capture holes in stable states, the process will gradually lead to a reduction of the density of E'_δ centers, as observed experimentally[73]. Moreover, the metastable trapping of holes in dimer defects may be difficult to distinguish from the "retarded" hole transport observed in oxides with high vacancy densities[74, 72, 77]. We note that hydrogen and O vacancy-hydrogen interactions can also play a significant role in determining MOS oxide trap charge, as discussed elsewhere[2, 79, 76].

The behavior of puckered positively charged O vacancies near the Si-SiO_2 interface during post-irradiation under switched-bias annealing is:

- Under positive bias, driving electrons to the fivefold-puckered configurations causes them to collapse to neutral dimers. Further negative or positive bias annealing has no effect.

- In contrast, driving electrons to the fourfold-puckered configurations simply places an electron into the dangling bond, while the puckered configuration remains, but a dipole complex forms. Reverse-bias annealing can easily destroy the dipole, driving the electron away, "restoring the hole." Of course, the hole on the puckered Si atom has been there all along. This is consistent with the data of both Schwank et al. and Lelis et al., as well as much other work on the reversibility of trapped positive charge in irradiated or stressed SiO_2 [74, 72, 77]. The results further confirm the model proposed by Lelis et al. to account for the cycling of

the restored positive charge by bias switching[74, 72, 77]. The cycling positive charge can diminish over time because the barriers for the collapse of metastable neutral puckered four-fold configurations are typically not large.

If the $E'_{\gamma 4}$ defect was near the interface so it could exchange charge with the Si on a time scale of the measurements being performed, (1) it would be a candidate for the border trap[21]. This charge exchange is typically slower than that for interface traps (2)-(4). Border traps are often referred to as slow states, anomalous positive charge, and switching oxide traps. Their impact on device behavior is proposed to be enhanced MOS 1/f-noise and stress induced leakage current. As MOS gate insulators have scaled down in thickness below ~30-50 Å, the bulk oxide trap behaviors becomes less important, except in field oxides and the buried oxides of SOI devices. This increases the relative importance of near-interfacial oxide traps, the $E'_{\gamma 4}$, in determining MOS performance, reliability, and radiation response.

The presented theoretical results help in the understanding of the underlying physical mechanisms involved in switched-bias annealing, and electron paramagnetic resonance (EPR) studies that suggest a common border trap, induced by trapped holes in SiO_2, is a hole trapped at an O-vacancy defect, which can be compensated by an electron, as originally proposed by Lelis and co-workers at Harry Diamond Laboratories [5]. Lelis and co-workers [5,21] proposed that the reversibility of the positive-charge annealing was caused by an electron tunneling into and out of an Si atom adjacent to a second, positively charged Si atom, associated with an $E'_{\gamma 4}$ defect in the near-interfacial SiO_2. A schematic diagram of this interaction is shown in Fig. 20. It was argued by Lelis *et al.* that this defect is stabilized by strain near the Si/SiO_2 interface.

Using the results from the statistical simulation examination of the behaviors of oxygen vacancies, a summary of the electronic states of pre-cursors and E'_{δ}, $E'_{\gamma 4}$, and $E'_{\gamma 5}$ states and their neutral capture cross-sections are given in Table 4. This table represents an average of the precursor states for the E'_{δ}, $E'_{\gamma 4}$, and $E'_{\gamma 5}$.

Summary

Using the results of Table 4 we will write differential equations for these defects and implement them in our device simulator. These equations will be discussed in Chapter VI.

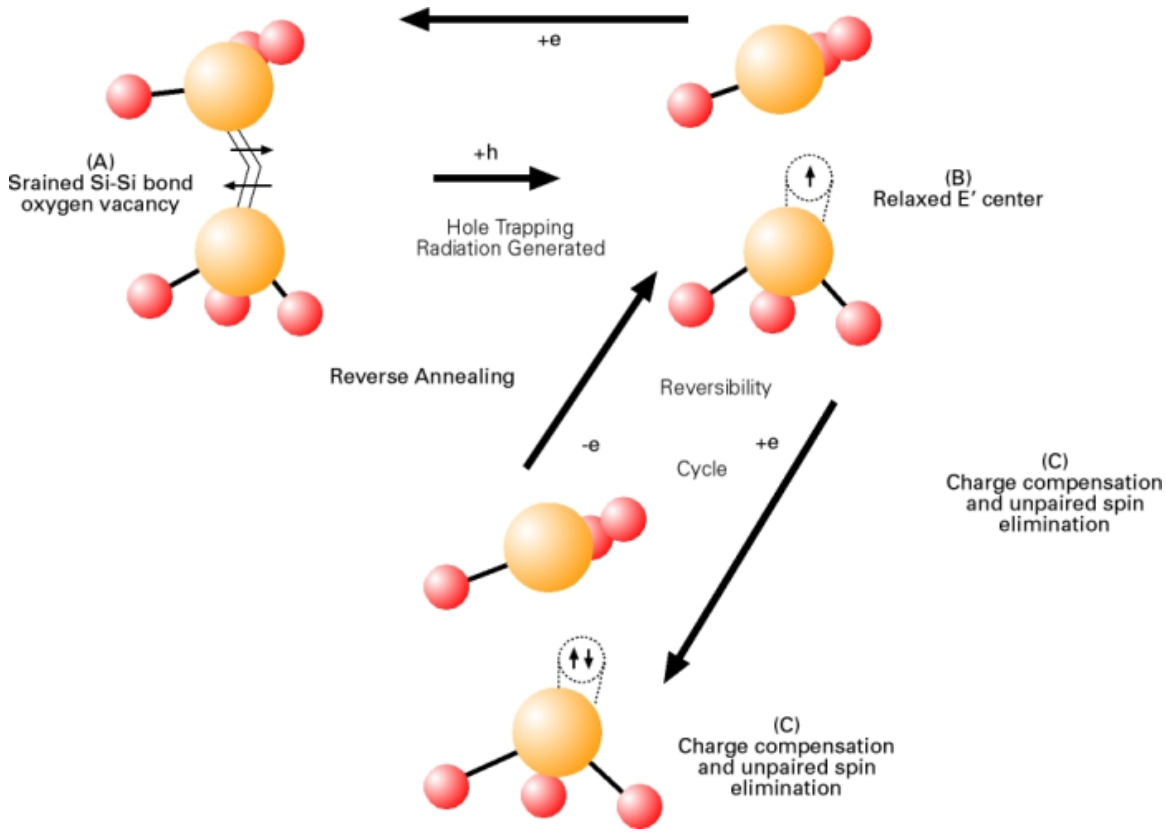

Figure 20: Schematic diagram of interaction suggested by Lelis and co-workers.

Table 4: A summary of the electronic states of pre-cursors and E'_{δ}, $E'_{\gamma 4}$, and $E'_{\gamma 5}$ states and their neutral capture cross-sections derived using the approach described in Chapter III.

Structure	%	Positive State	σ_p (cm^2)	σ_n (cm^2)
OV^1	80%	E'_{δ}	3×10^{-15}	2×10^{-15}
OV^2	10%	$E'_{\gamma 4}$	5×10^{-15}	1×10^{-16}
OV^3	10%	$E'_{\gamma 5}$	5×10^{-15}	1×10^{-16}

CHAPTER V

EXTRINSIC DEFECTS: HYDROGEN RELATED

Introduction

The presence of hydrogen (H) in a-SiO_2 is a consequence of the semiconductor manufacturing process. Its introduction is due to the ambient used in the oxidation process, or to the hydrogen anneals used to passivate Si dangling bonds that would otherwise act as traps at the a-SiO_2-Si interface. Irradiation releases hydrogen in the bulk of the oxide, which can depassivate these traps[80, 81, 82, 83, 84]. The effects of interface traps induced by ionizing radiation (or hot electrons) on semiconductor devices are well understood, and associated with the stretch-out of MOSFET sub-threshold and capacitor CV characteristics, threshold-voltage shifts, increased surface recombination, and reduced inversion layer mobility[32]. A generally accepted model is that hydrogen, in the form of mobile protons, is an important element in models of total dose interface trap buildup. However, the interaction of hydrogen with defects in the oxide is not completely understood. Discussions remain about which defects act as a source of hydrogen, which conditions yield protons, and which produce neutral hydrogen[82, 80] or trapped protons that may account for a fraction of trapped charge in the oxide[85]. This chapter will use *ab initio* simulation to help understand the roles of H and H^+ in charge buildup within a-SiO_2. The results will then be applied to an improved hydrogen model.

In the simplest model of interface trap buildup, originally proposed by McLean[86], protons (H^+) are released upon hole capture (h^+) from unspecified hydrogen complex defects (DH). This process can be represented by the following reaction:

$$h^+ + DH \longrightarrow D + H^+ \tag{22}$$

The protons are then transported to the interface under the influence of an applied bias[15, 20]. The proton arrives at the interface, captures an electron from the Si side, and becomes neutral H. It then reacts with a hydrogen-passivated dangling bond to form a center[15] via the reaction:

$$Si_3 \equiv Si - H + H^+ + e^- \longrightarrow Si_3 \equiv Si\cdot + H_2 \tag{23}$$

A variation on this model by Shaneyfelt *et al.*[87, 88] suggests that holes are trapped at defects near the interface prior to releasing a proton. Recent work by Rashkeev *et al.*[30] showed that the electron from the Si is not needed and that the reaction is:

$$Si_3 \equiv Si - H + H^+ \longrightarrow Si_3 \equiv Si^+ + H_2 \tag{24}$$

This allows the hydrogen molecules to then diffuse away from the interface, leaving the charged defect state to be controlled by the surface potential of the Si. The $Si_3 \equiv Si^+$ defect is also known as the P_b center[20] as depicted in Fig. 13. This result simplifies the reaction at the interface, and demonstrates that the depassivation of precursors (P_b centers) is independent of the available electrons at the interface.

Mrstik and Rendell proposed a model in which neutral, rather than ionic, hydrogen is released from the defects[82, 89]. In this scheme, the buildup of interface traps is mediated by the formation and subsequent cracking of molecular hydrogen as seen in:

$$h^+ + DH \longrightarrow D^+ + H \tag{25}$$

$$2H \longrightarrow H_2 \tag{26}$$

$$H_2 + D^+ \longrightarrow H^+ + DH \tag{27}$$

The two types of evidence supporting this model are the increase in trap density after both irradiation and the subsequent introduction of molecular hydrogen[90, 91, 92], and the correlation with changes in electron paramagnetic (EPR) signals for specific defects. Some issues related to these models involve the role of defects in determining proton transport properties, which seem to depend strongly on processing[18, 2, 76], and also sources of hydrogen other than the oxide, which may be important for latent buildup of interface traps. At low temperatures, neutral hydrogen can be produced directly by radiation via the reaction:

$$DH + \gamma \longrightarrow D + H \tag{28}$$

where DH is thought to be a Si-O-H group[89]. While there have been many quantum mechanical calculations of defect structures in SiO_2, these have either focused on properties for the

individual defects, or have only considered specific aspects of these models, such as transport mechanisms or the cracking of H at defect sites[80, 89, 93].

Understanding the interactions between electrical charges, hydrogen, and defects in the oxide is important for improving the radiation hardness and reliability of MOS devices. Hydrogen's presence in a-SiO_2 clusters, described as extrinsic defects in Chapter III, is explored using DFT to examine its interaction with defect free a-SiO_2 cells, and a-SiO_2 cells with an oxygen vacancy in various charge states. The initial defect-free cell simulations were conducted with H in various initial positions, with the cell given neutral, negatively and positively charged states. Additional ab initio experiments were conducted with H in H_0, H_2 and H^+ states in the four amorphous cells, and with existing oxygen vacancy (V_0) centers in neutral and positive charge states. The intent is to provide more insight into the behaviors of H within a-SiO_2 and to improve the models for H within a-SiO_2 and H^+ generation.

Hydrogen in Defect Free a-SiO_2

Results from DFT calculations suggest that hydrogen atoms form trap states for holes or electrons in the four a-SiO_2 cells studied. The H atom's behavior in the a-SiO_2 cells depends very much on the local structure. When the cell is neutral, the H atom can remain in a void, Fig 21(a), attach itself to a Si atom, Fig. 21(b), which then becomes fivefold coordinated, or attach itself to a bridging oxygen atom, Fig. 21(c). This examination shows the H atom prefers to attach to a bridging oxygen atom 80% of the time. The H atom bonding to a Si atom is preferred 10% of the time and the H atom remains in a void the remaining 10% of the time.

When the H atom remains in a void, a neutral electrical state centered around 3.1 eV above the valence band is produced. In this local arrangement the defect state is allowed to capture an electron, forming an Si-H^- bond of 1.5 Å and a negative electrical state centered around 3.8 eV above the valence band.

When a neutral H atom bonds to a Si atom, the bond length of Si-H on the $O_4 \equiv Si - H$ structure is 1.6 Å. The neutral electrical state is centered around 1.7 eV above the valence band. In this local arrangement, a positively charged electrical state, formed by capturing a hole, moves the electrical state to 2.5 eV above the valence band. The H atom moves across the void to form a $Si - (OH^+) - Si$ complex. The calculations show that the distance between the H^+ and O atoms is

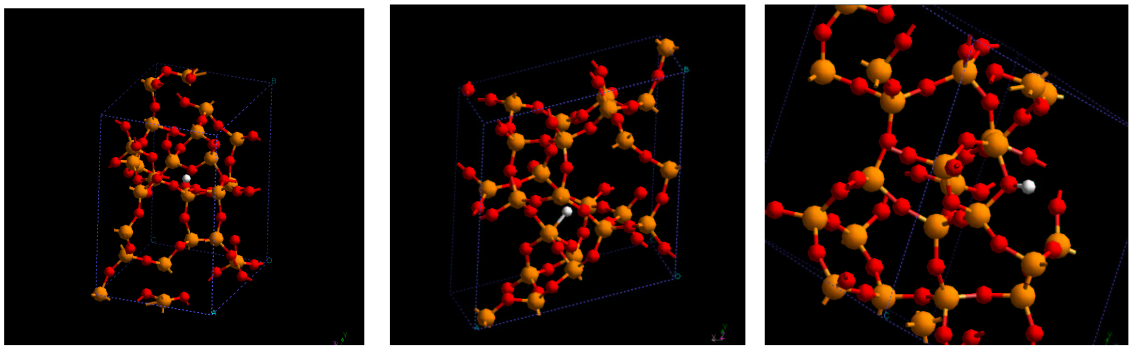

Figure 21: Possible positions of neutral H in the a-SiO_2 cells, (a) remaining in a void, (b) attached to a Si atom, and (c) attached to a bridging O atom.

about 1.0 Å. This is slightly longer than that of the neutral O-H bond length of 0.95 Å. The length of the Si-O bond near the H^+ atom is elongated, going from 1.6 to 1.7 Å, suggesting that the H^+ atom weakens the neighboring Si-O bond to form an $O-H^+$ bond. This sequence is shown in Fig. 22. A negatively charged state is produced by electron capture, forming an $Si-H^-$ bond of 1.0 Å and an electrical state at 3.5eV above the valence band.

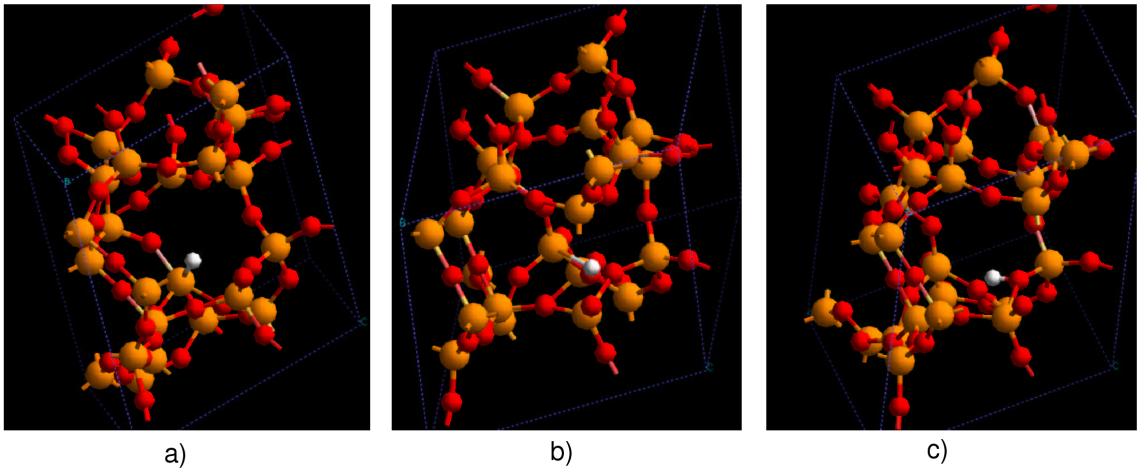

Figure 22: An $O_4 \equiv Si-H$ structure transforming to an $Si_2 \equiv O-H^+$ bond upon hole capture.

This defect structure has a hole capture cross section of 4.8×10^{-15} cm^2, and an electron capture cross section of 2.1×10^{-15} cm^2, obtained using the equations in Chapter III.

If an H atom interacts with a $O_3 \equiv Si-O-Si \equiv O_3$ structure, where the $Si-O-Si$ angle is

greater than 160°, the resulting structure will form an $O_3 \equiv Si - O - H \quad \bullet Si \equiv O_3$ structure as shown in Fig. 23. Upon capturing a hole, the resulting $O_3 \equiv Si - O - H \quad {}^{+}Si \equiv O_3$ structure is no longer paramagnetic. If an electron is returned to the system, the electron associates with the Si-OH to form a dipole.

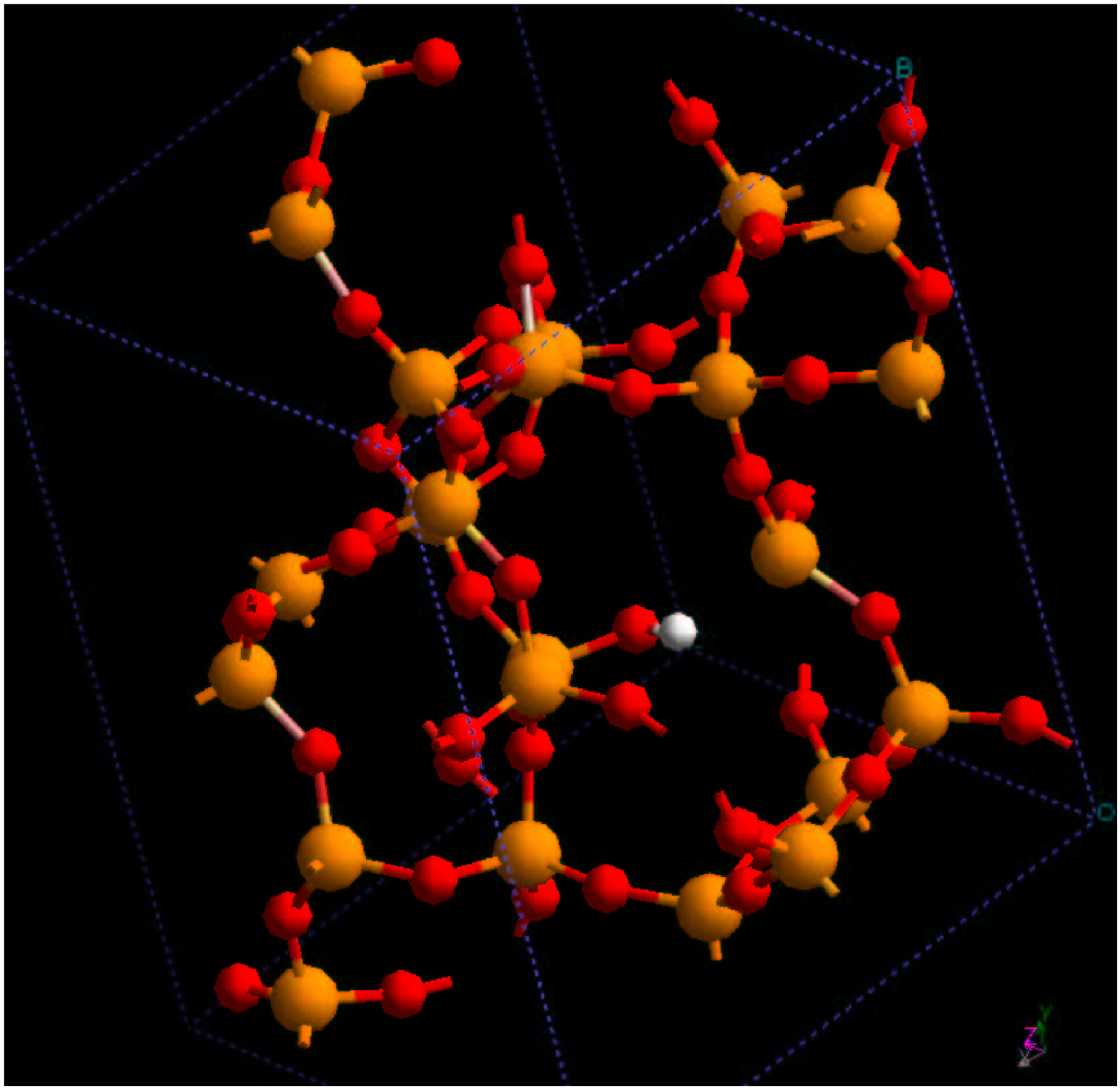

Figure 23: A $O_3 \equiv Si - O - Si \equiv O_3$ structure where the $Si - O - Si$ angle is greater than 160°, the resulting structure will form an $O_3 \equiv Si - O - H \quad \bullet Si \equiv O_3$ structure.

This defect type has a hole capture cross-section of 4.1×10^{-15} cm^2, and an electron capture cross section of 3.1×10^{-15} cm^2. This defect's neutral electrical state is at 4.5 eV, it transitions

to within 0.5 eV of the valence band when it captures a hole[94, 95, 96, 2], and it transitions to 4.7 eV when capturing an electron.

For structures where the $Si-O-Si$ angle is less than 160°, the H bonding to a bridging oxygen atom is shown in Fig. 24. This $O-H^+$ bond ranges from 1.0 to 1.12 Å when neutral, and 0.95 Å when it traps a hole. This defect type has a hole capture cross section varying from 4.0×10^{-15} to 6.5×10^{-15} cm^2, and an electron capture cross section varying from 2×10^{-15} to 2.3×10^{-16} cm^2. This defect type has neutral energy states between 4.8 and 8.1 eV. The state transitions between 4.3 eV and 0.5 eV from the valence band upon hole capture, and between 4.9 eV and 8.4 eV upon electron capture.

With the $O-H^+$ structure formed when the cell captures a hole, a numerical experiment was conducted to determine the barrier to H^+ hopping to a nearest neighbor oxygen. A proton (H^+) was moved along a straight line to the next nearest oxygen atom. The proton, and the two involved oxygen atoms were frozen for each iteration of the total energy calculation, while the rest of the structure was allowed to relax. The calculated barrier to this diffusion is 0.67 eV. This barrier implies that hopping transport requires an applied electric field.

Hydrogen Interaction with Oxygen Vacancies

Hydrogen's interactions with existing neutral oxygen vacancies, precursor $E'_{\gamma4}$, $E'_{\gamma5}$, E'_{δ} centers, and these centers in positively charge states, were examined. Atomic hydrogen (H), molecular hydrogen (H_2), and a proton (H^+) were introduced into the cells.

Starting from the neutral E'_{δ} pre-cursor, when neutral hydrogen (H^0) was added to a cell, a reaction given by Eq. (29) and depicted in Fig. 24 occurred.

$$O_3\equiv Si-Si\equiv O_3+H^0\longrightarrow O_3\equiv Si\bullet(E'_{\beta})+H-Si\equiv O_3 \tag{29}$$

These same neutral E'_{δ} pre-cursor sites would also "crack" molecular hydrogen (H_2) and form the structure given by Eq. (30), as depicted in Fig. 25.

$$O_3\equiv Si-Si\equiv O_3+H_2\longrightarrow O_3\equiv Si-H\quad H-Si\equiv O_3 \tag{30}$$

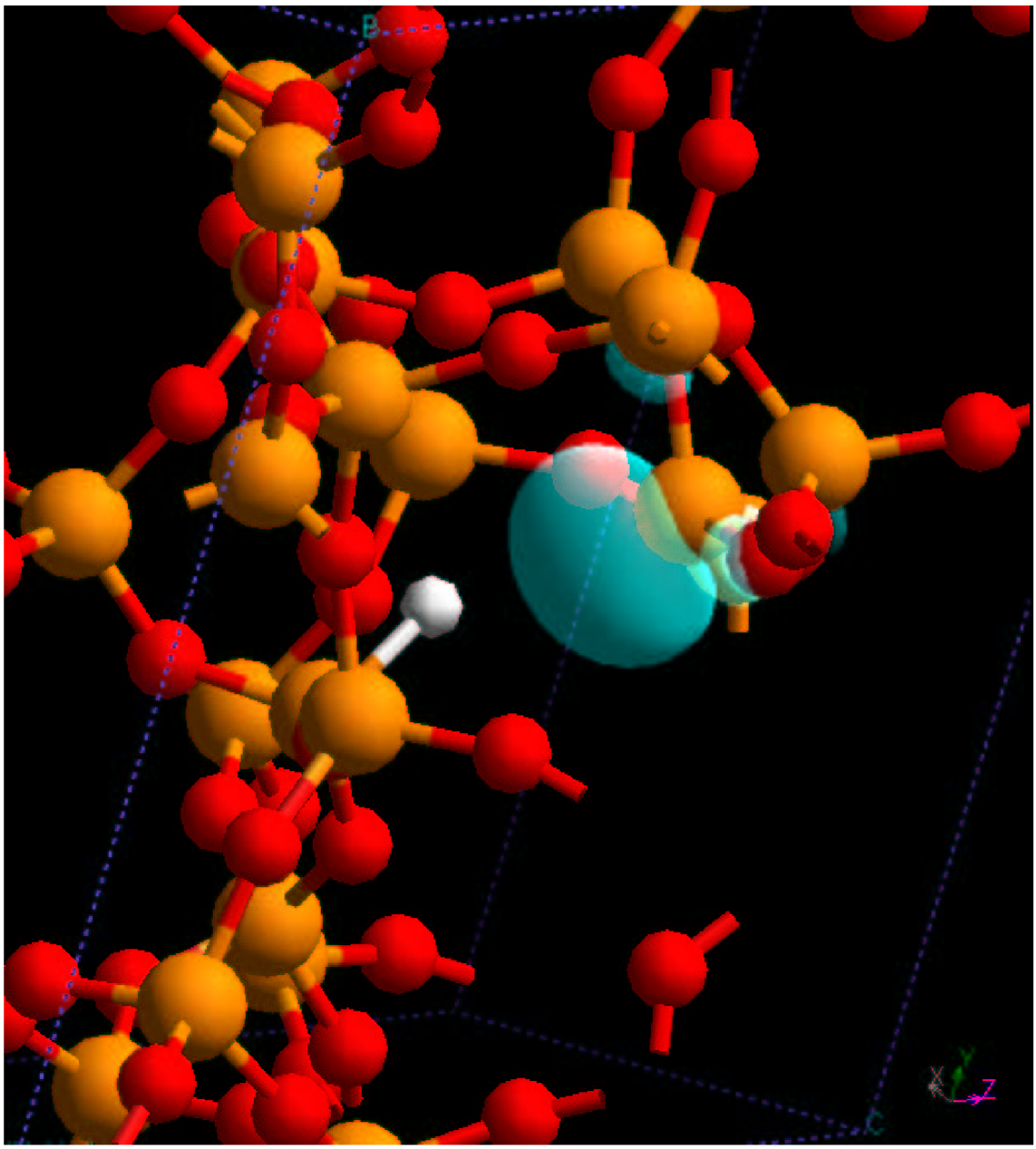

Figure 24: An E'_{β} center generated by a neutral oxygen vacancy capturing a neutral hydrogen, H^0.

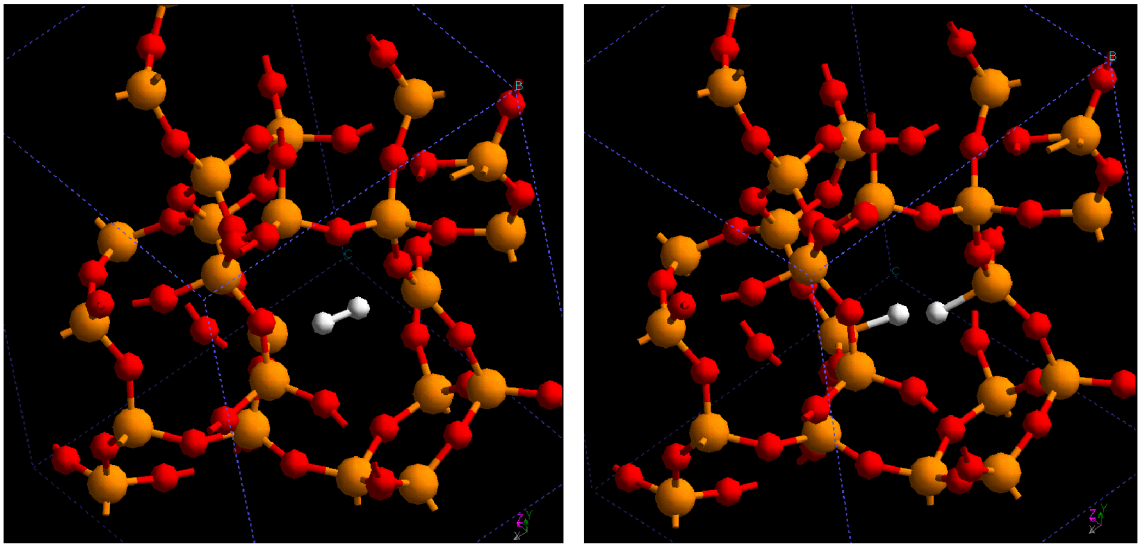

Figure 25: A E'_{δ} pre-cursor site that "cracks" molecular hydrogen.

These passivated E'_{δ} pre-cursor sites were no longer able to trap carriers. If H was introduced to these passivated E'_{δ} pre-cursor sites, an E'_{β} site was generated as given in Eq. (31).

$$O_3 \equiv Si - H \quad H - Si \equiv O_3 + H \longrightarrow O_3 \equiv Si\bullet \quad H - Si \equiv O_3 + H_2 \tag{31}$$

These passivated E'_{δ} pre-cursor sites also can interact with a proton, producing the state defined by Eq. (32).

$$O_3 \equiv Si - H \quad H - Si \equiv O_3 + H^+ \longrightarrow O_3 \equiv Si + \quad H - Si \equiv O_3 + H_2 \tag{32}$$

When molecular hydrogen is introduced to positively charged centers $E'_{\gamma 4}$ and $E'_{\gamma 5}$, the result is described by Eq. (33) and shown in Fig. 26.

$$E'_{\gamma 4} + H_2 \longrightarrow O_3 \equiv Si - H \quad {}^+Si \equiv O_3 + H \tag{33}$$

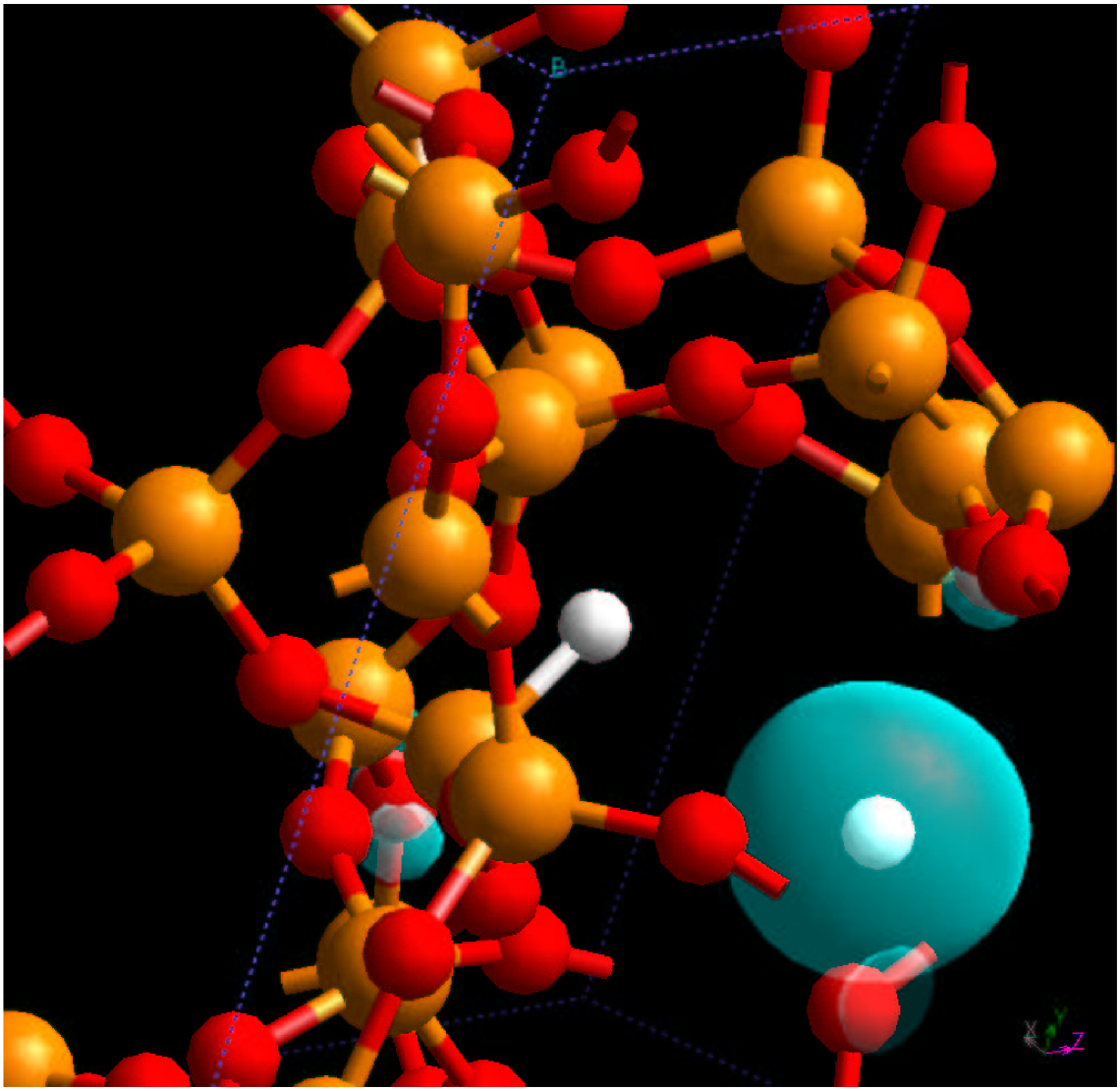

Figure 26: An $E'_{\gamma 4}$ center when presented two separate neutral hydrogen atoms or H_2, produced an Si – H bond and a lone hydrogen atom remained. The positive charge is located on the puckered Si atom.

When an electron was added it produced a dipole:

$$O_3 \equiv Si - H \quad {}^{+}Si \equiv O_3 + e^{-} \longrightarrow O_3 \equiv Si - H^{-} \quad {}^{+}Si \equiv O_3 \tag{34}$$

None of the DFT calculations conducted with oxygen vacancy defect states D_0, D_1, D_2, P_0, or P_1 in neutral or positive charge states, and H in atomic or molecular form, produced a lone proton.

Hydrogen Summary

Hydrogen's behavior in the studied a-SiO_2 cells is complex. H^0 transporting through the oxide acts as an electron trap, with an occurrence of approximately 10%, having a capture cross-section of 2.5×10^{-15} cm^2. Upon electron capture, a $Si - H^{-}$ bond is produced with a negative charge state distributed about 3.8 eV. In 10% of the experimental cases, H interacted with the cell to form a $Si - H$ bond, given that the cell was in a neutral state.

The DFT calculations show that a significant excess electron density can be included on the H atom of an Si-H. For a transporting proton, coulombic attraction leads to the formation of an interface trap, through a direct chemical reaction between the H^{+} and the Si-H (59),(60).

$$Si - H^{-} + H^{+} \longrightarrow Si^{+} + H_2 \tag{35}$$

However, if there is a hole nearby, there may not be enough energy to break the Si-H bond and/or transfer the negative charge from the H to the positively charged site in the SiO_2. Supporting this equation, the DFT data show that hydrogen does not form states within the a-SiO_2 bandgap when bonded to Si. This would make the electronic transfer from the Si-H to the trapped positive charge extremely difficult, even when the two are in close proximity since the negative charge residing on the H produces a lower ground state.

The negative charge in the Si-H defect would screen a trapped positive charge from a tunneling electron from the Si. This screening changes the capture cross-section of positively charged defects near this negative charge in the Si-H defect. This net charge transfer from the Si to the H may allow an extra electron to reside in this location as long as it is stabilized by the nearby positive charge, as long as the Si-H is at or near-enough to the Si/SiO_2 interface that the Si is in communication with the channel.

Seventy-five percent of the observed cases for neutral hydrogen's interaction with the a-SiO_2 cells created an $O - H^{+}$ bond upon hole capture. These neutral $O - H$ centers have hole capture

cross sections ranging from 4×10^{-15} to 6.5×10^{-15} cm^2. These positively charged defect states ranged from 4.3 to 0.5 eV above the valence band. In approximately 5% of the cases studied, H formed an $Si-O-H \quad \bullet Si$ defect structure. The originating $Si-O-Si$ structure bond angle was above 160°. The $Si-O-H \quad \bullet Si$ defect structure presented a neutral defect state centered around 4.5 eV above the valence band. This defect state has electron and hole capture cross sections of 3.1×10^{-15} and 3.1×10^{-15} cm^2, producing states at 4.9 and 0.5 eV above the valence band, respectively. Table 5 summarizes atomic H interaction with the a-SiO_2 cells.

Table 5: Summary of hydrogen's, H^0, interaction with the a-SiO_2 cells, where H_{D0}, H_{D1}, H_{D2}, and H_{D3} represent a classification of this behavior.

	STRUCTURE	%	NEUTRAL STATE	POSITIVE STATE	NEGATIVE STATE	σ_p	σ_n
H_{D0}	VOID Si—H-	10%	3.1eV		3.8eV		2.5E-15
H_{D1}	Si—H O—H+ Si—H-	10%	1.7eV	2.5eV	3.5eV	4.8E-15	2.1E-15
H_{D2}	O—H O—H+ O—H-	75%	4.8-8.1eV	4.3-0.5eV	4.9-8.4	4-6.5E-15	2E-15-2.3E-16
H_{D3}	Si-OH •Si Si-OH +Si Si-OH -Si	5%	4.5eV	0.5eV	4.9eV	4.1E-15	3.1E-15

H^0 and H_2 interacted with existing oxygen vacancies, Eqs. (29) and (30), to produce a structure of the form $O_3 \equiv Si-H \quad \bullet Si \equiv O_3$ when neutral, and $O_3 \equiv Si-H \quad {}^{+}Si \equiv O_3$ or $O_3 \equiv Si-H^{-} \quad \bullet Si \equiv O_3$ when negatively charged. This structure has a neutral state around 5.1 eV with hole and electron capture cross sections of 4.1×10^{-15} and 2.4×10^{-15} cm^2, respectively. Upon capturing a hole, this state moves to within 0.5 eV of the valence band and to a state around 6.1 eV upon electron capture.

The complexity of hydrogen behavior within a-SiO_2 makes it difficult to implement models. Current device level defect models rely on either McLean[17] or Mrstik and Rendell[89], as given in the equations below:

$$h^+ + DH \longrightarrow D + H^+ \quad \text{(McLean)} \tag{36}$$

$$2h^+ + DH \longrightarrow D^+ + H^+ \quad \text{(Mrstik and Rendell)} \tag{37}$$

where D represents a generic defect of unknown concentration. This leaves the device simulator with the following variables:

- concentration of defects D,
- concentration of free H, and
- concentration of bonded H.

The process of proton generation in the oxide is related to the transport of holes through the a-SiO_2 system. The holes react with hydrogen-containing defects, DH centers, which, in our simulations, are primarily the Si-OH-Si structures.

Our proton generation model is:

$$\frac{d[H^+]}{dt} = \frac{1}{2}\sigma_{\mathrm{DH}} v_{th} p N_{\mathrm{DH}} \tag{38}$$

where N_{DH} is the concentration of hydrogen containing defects in the bulk and σ_{DH} is the capture cross-section for holes that release the protons. Interface-trap formation is described by:

$$\frac{dN_{it}}{dt} = k_1 [Si - H] \frac{J_{H^+}}{q} \tag{39}$$

where N_{it} is the surface concentration of interface defects, $[Si - H]$ is the density of passivated interface defects, k_1 is the rate constant, and J_{H^+} is the proton current density at the interface.

Summary

The features of interface trap generation in irradiated MOS devices, especially the post-irradiation interface trap buildup process, have experienced some scientific insight recently[28, 29] but remain issues requiring more investigation for predictive modeling.

The improvement in the multiple carrier transport within the oxide and Eqs. (38) and (39) are this Chapter's contributions to TID effects modeling.

CHAPTER VI

FIRST PRINCIPLES TO DEVICE PHYSICS

Introduction

One of the main effects of radiation on metal-oxide-semiconductor (MOS) structures is the buildup of positive charge in the oxide regions. This positive charge is primarily due to the trapping of mobile holes that are generated during radiation exposure. We have modeled the processes of radiation-induced carrier generation, transport and trapping using a device simulator. The recombination of carriers generated by the radiation exposure is modeled using the geminate recombination model. The transport of carriers which survive geminate recombination is modeled using drift-diffusion and continuity equations similar to those used in semiconductor materials. The carrier trapping at defect energy levels described in Chapter IV is modeled using a set of first order differential equations. This chapter describes all of the above models in detail, and presents a study of the radiation exposure of MOS capacitors based on these models. The various issues associated with the implementation of device-level models capable of simulating time-dependent radiation response are highlighted throughout the chapter. Finally, the study also presents an example of the data required to extract analog behavioral models from such device simulations. The resulting analog behavioral model is combined with a compact model to generate a macro-model of a partially depleted SOI NMOS device.

Device Simulation Framework

Introduction

The TCAD simulation framework developed to run the radiation-exposure simulations is based on tools for 1D, 2D, and 3D simulation of semiconductor technologies. These tools have a full tetrahedral meshing engine for simulation of complex 3D geometries. Built-in and user-defined mesh refinement criteria can be used for problem-specific customization of the mesh during a simulation. Physical models for device phenomena, such as impact-ionization, interface and bulk defects, and carrier generation and transport in the semiconductor and insulator regions are available. All physical models are highly customizable through user-defined C-language functions, which can be loaded by the simulator through a C-interpreter interface or as object code. Finally,

this framework provides a transparent interface to all existing SILVACO TCAD simulation tools.

Physical Models

The device simulator implements a comprehensive set of physical models required for simulation of modern semiconductor materials and structures. All physical models, which are available in SILVACO's Atlas simulation tool, are also available under this framework. Additionally, several models required specifically for simulating the radiation response of semiconductor structures under various radiation environments are also available.

Total Dose Simulation Models

The device simulator includes modules for simulation of total-dose effects in a variety of semiconductor technologies, including bulk and SOI CMOS. In particular, methods for simulating carrier generation, transport, trapping and detrapping in insulator regions of a device have been included. The user can specify various characteristics of a total-dose exposure such as the dose rate, total dose, electron-hole pair generation rate, and recombination rates. The carrier trapping and detrapping parameters can be specified by the user through a C-language interface.

User-Defined Models Using C-Interpreter and Dynamic Loader

The SILVACO simulation tools have provided a mechanism for defining arbitrary models for a select set of physical mechanisms through the use of C-programming language functions. In the past, these functions have been interpreted using a C-interpreter built into the simulator. However, this approach has several disadvantages. First, the C programming language was not designed to be an interpreted language. This is a significant challenge for the C-interpreter implementation, and usually results in a large performance hit. Additionally, the C-interpreter implementation has to support all the features of the programming language.

In order to mitigate the limitations of the C-interpreter, the new device simulation framework implements a shared object library interface as an alternative. This interface allows users to implement arbitrarily complex models for various physical mechanisms in programming languages of their choice including C, C++, and Fortran. The simulator requires these models to be compiled as shared objects which can be dynamically loaded by the simulator at run time. This interface has been tested with the C and C++ programming languages. It also was used to implement an interface between the simulator and the Python programming language interpreter[97].

Device Simulation Models

In our simulations, the oxide regions of interest are treated as wide-bandgap semiconductors with appropriate carrier mobilities in order to simulate the generation, transport, and trapping of carriers due to radiation exposure. This results in the following set of equations to be solved in the oxide regions during device simulations:

Poisson's Equation

$$\nabla^2\psi = -\frac{q}{\varepsilon_{ox}}\left(p - n + \sum_{i=1}^{n} p_t^{(i)} - \sum_{i=1}^{n} n_t^{(i)}\right) \tag{40}$$

Here, $p_t^{(i)}$ and $n_t^{(i)}$ represent the densities of trapped holes and trapped electrons respectively in the i-th trap level.

Electron Continuity Equation

$$\frac{\partial n}{\partial t} = \frac{1}{q}\nabla\cdot\mathbf{J_n} + G_{\text{ehp}}(E) - \sum_{i=1}^{n}\frac{dn_t^{(i)}}{dt} \tag{41}$$

$$\mathbf{J_n} = qn\mu_n\mathbf{E} + qD_n\nabla n \tag{42}$$

Here, $G_{ehp}(E)$ is the net electron-hole pair generation rate after geminate recombination. Geminate recombination is taken into account using the curve of yield as a function of the electrostatic field calculated by Ausman[98]. The net generation rate is obtained at each point in the oxide after multiplying this yield by the generation rate obtained from the dose rate.

The rate of trapping of electrons at the i-th trap level is given by:

$$\frac{dn_t^{(i)}}{dt} = \sigma_n^{(i)}\frac{J_n}{q}\left(f^{(i)}N_{Tn} - n_t^{(i)}\right) \tag{43}$$

Here, $\sigma_n^{(i)}$ is the electron capture cross-section at the i-th trap level, and $f^{(i)}$ is the fraction of the total trap density (N_{Tn}) that represents the i-th trap level in the oxide.

Hole Continuity Equation

$$\frac{\partial p}{\partial t} = -\frac{1}{q}\nabla\cdot\mathbf{J_p} + G_{\text{ehp}}(E) - \sum_{i=1}^{n}\frac{dp_t^{(i)}}{dt} \tag{44}$$

$$\mathbf{J_p} = qp\mu_p\mathbf{E} - qD_p\nabla p \tag{45}$$

The rate of trapping of holes at the i-th trap level is given by:

$$\frac{dp_t^{(i)}}{dt} = \sigma_p^{(i)} \frac{J_p}{q} \left(f^{(i)} N_{Tp} - p_t^{(i)} \right) \tag{46}$$

Here, $\sigma_p^{(i)}$ is the electron capture cross-section at the i-th trap level, and $f^{(i)}$ is the fraction of the total trap density (N_{Tp}) that represents the i-th trap level in the oxide.

The hole and electron mobilities used during the simulations were 1.0×10^{-5} cm^2/Vs and 20 cm^2/Vs respectively[2]. The capture cross sections ($\sigma_n^{(i)}$ and $\sigma_p^{(i)}$) and the trap fractions ($f^{(i)}$) were obtained from our theoretical calculations as shown in Table 4. The trap densities N_{Tn} and N_{Tp} were set to 4.19×10^{18} cm^{-3} during our simulations[18]. The emission of trapped electrons and holes, as well as recombination of mobile carriers with trapped carriers of the opposite kind, were neglected in these simulations.

Experimental Structures

The simulation approach described above was used to model the effects of total-dose radiation exposure in a set of MOS capacitor structures with various oxide thicknesses under various applied fields. The oxide thicknesses ranged from 15 nm to 380 nm. A dose rate of 140 rad(SiO_2)/s was used during the simulations, while the capacitors were biased with voltages ranging from -10 V to +10 V. All simulations were performed to a total dose of 1 Mrad(SiO_2).

Simulation Results

The decrease in threshold voltage as a function of total-dose in the case of an nMOS capacitor with 380 nm gate oxide is shown in Fig. 27. As seen here, the high geminate yield at larger electric fields results in higher trapping rates in the oxide. As expected, the threshold voltage decreases with total dose, and saturates at high doses when a dynamic equilibrium has been reached between carrier trapping and detrapping. The saturation level, as well as the rate of buildup of charge, depends on the gate voltage, due to the dependence of geminate yield on the applied electric field. In the case of radiation exposure at negative gate biases, the holes are trapped closer to the gate electrode and result in a smaller threshold voltage shift compared to the corresponding positive gate bias exposure. In other words, even though the oxide electric fields are the same in both cases, the location of the trapped holes is significantly different, resulting in markedly different effects on

the device parameters. This can be seen more clearly in Fig. 28, which shows the threshold voltage shift after 1 Mrad(SiO_2) total-dose exposure at various gate biases.

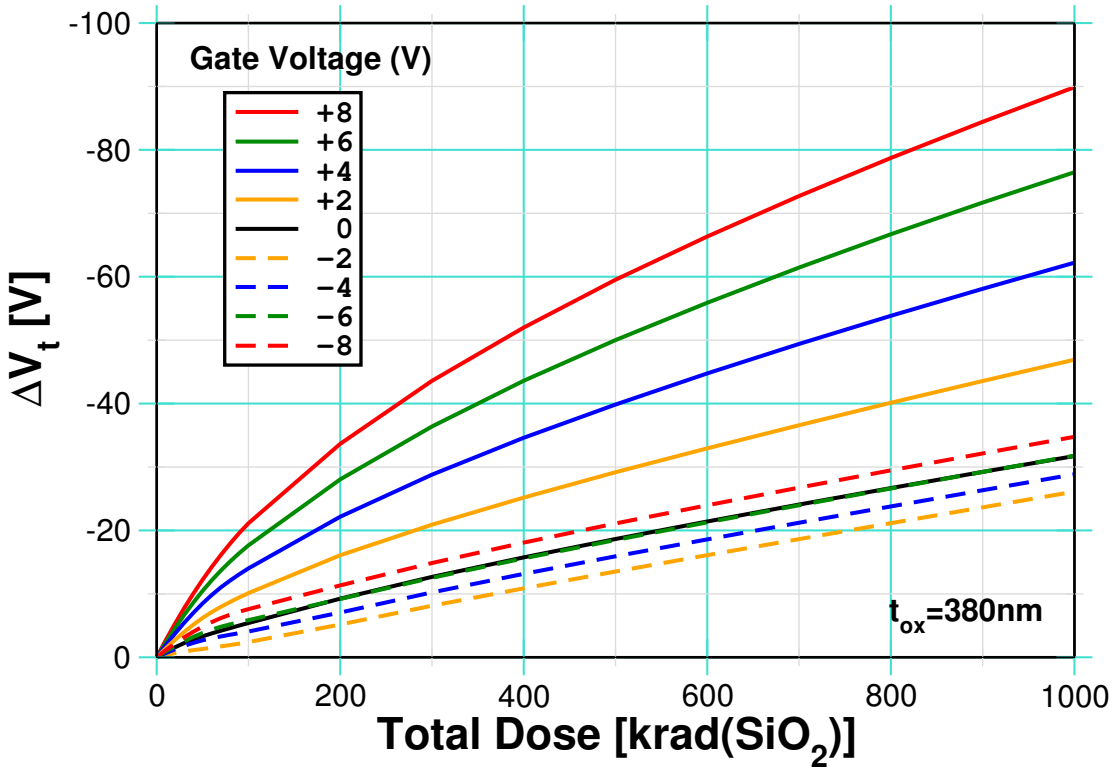

Figure 27: Threshold voltage decrease as a function of total-dose at various gate biases in an nMOS capacitor with a 380 nm gate oxide.

The simulated ΔV_t shows a linear-to-cubic variation with oxide thickness. The linear variation occurs at large thicknesses. This is because at larger thicknesses there is a large number of free holes in the oxide, both due to lower fields for the same voltage, and a larger total number of generated holes. This leads to higher trapping rates, and the traps quickly get almost completely filled. Further increase in the oxide thickness makes no difference to the amount of trapped charge. Since most of the traps are concentrated near the interface, ΔV_t varies linearly with t_{ox}. At medium thicknesses, the traps never get completely filled, and trapping is limited by the total number of holes generated in the oxide. As the thickness increases, ΔV_t increases not only due to the trapped charge, but also because the number of holes generated increases with thickness, giving a t_{ox}^2 dependence. At lower thicknesses, the field in the oxide is very large. Thus, the drift velocity of holes is fairly large, and a greater number of them tend to get swept out of the oxide before getting

trapped. For these thicknesses, there is yet another t_{ox} dependence due to the fact that for larger thicknesses the total number of holes decreases due to lowered fields.

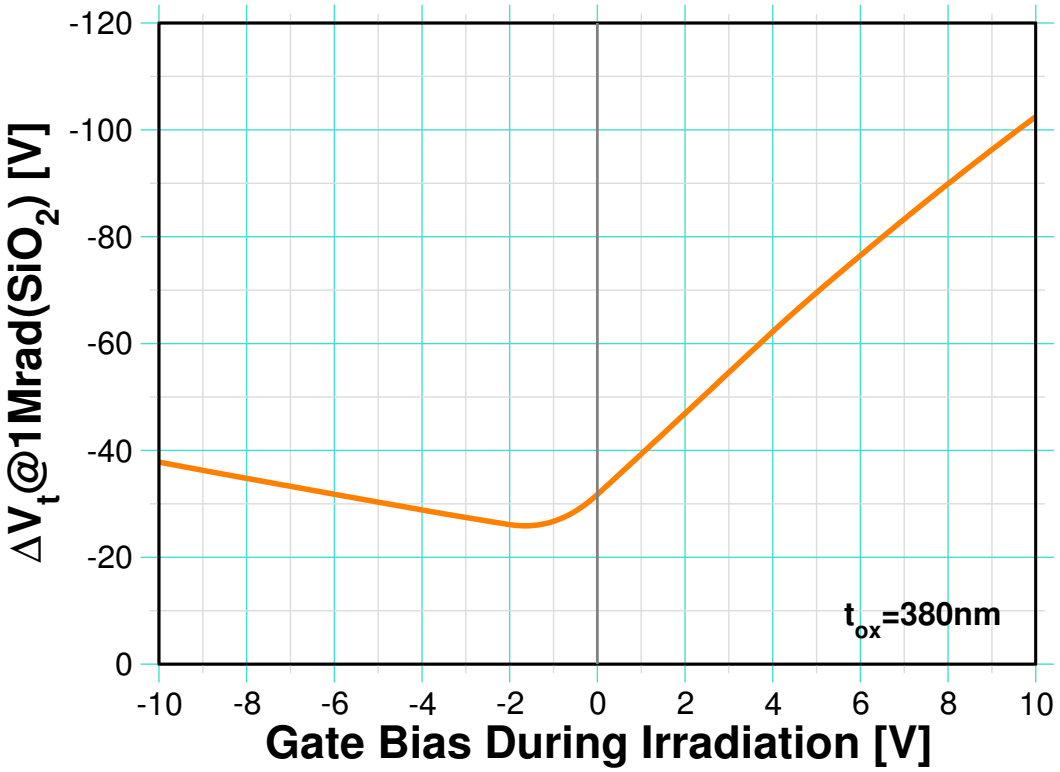

Figure 28: Threshold voltage decrease as a function of gate bias at a total-dose of 1 Mrad(SiO_2) in an nMOS capacitor with a 380 nm gate oxide.

These results are in general agreement with the analytical results of Viswanathan and Maserjian who have predicted a t_{ox}^2-to-t_{ox}^4 dependence of ΔV_t on oxide thickness[99]. However, it should be noted that they have used a uniform trap density in the oxide and the drift velocity of holes instead of the thermal velocity in the trap rate equation. The use of v_d in the trap rate equation reduces the field dependence of the trapping rate, and hence decreases the thickness dependence. If v_{th} is used in the simulations described here with a uniform trap density, a t_{ox}^2-to-t_{ox}^4 dependence is obtained.

As the gate voltage becomes more positive, ΔV_t decreases sharply, goes through a minimum, and then begins to rise. This is because when the gate voltage increases beyond the oxide flat-band condition, more and more holes are driven to the interface, leading to a rise in the flat-band voltage shift. ΔV_t continues to rise until it reaches a point when the increase in the hole concentration at

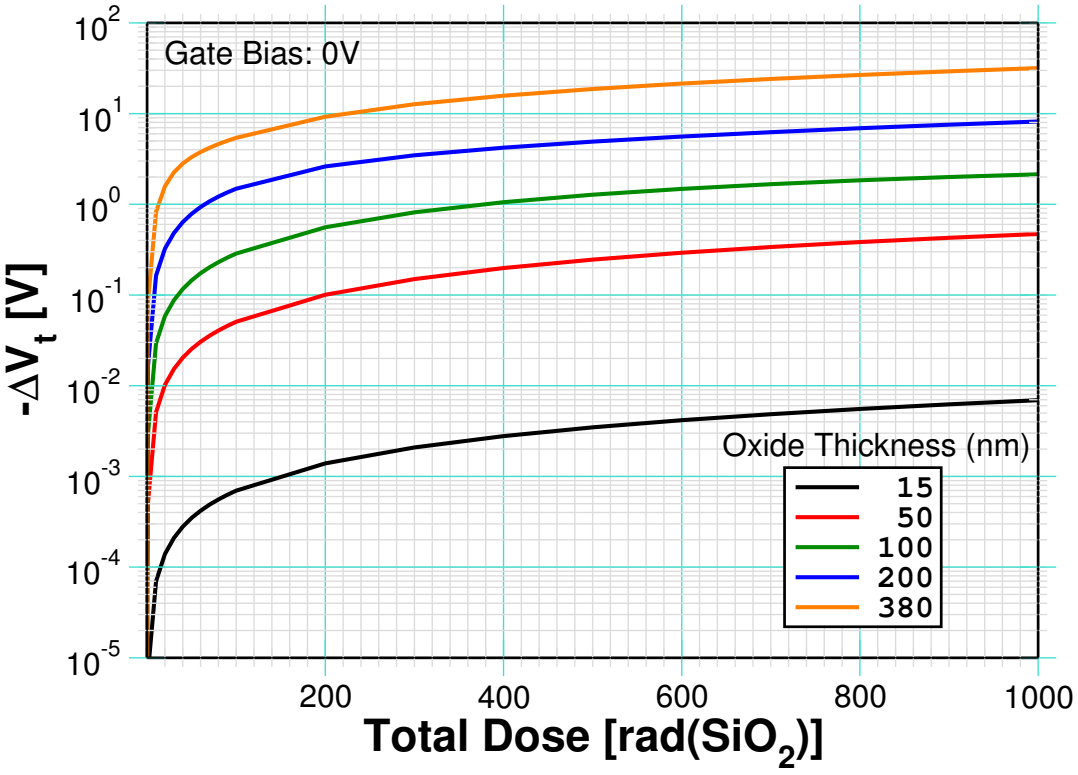

Figure 29: Dependence of ΔV_t on the oxide thickness, t_{ox}, during radiation exposures at gate biases of 0 V.

the interface due to a positive gate voltage is offset by a decrease in the hole concentration due to high electric fields. Since the electric fields are lower for larger thicknesses at the same gate voltage, this maximum occurs at larger voltages for higher oxide thicknesses. This decrease of ΔV_t is commonly observed in experiment, and it has been previously attributed to a reduction in capture cross section with the electric field. However, our simulation shows that lower cross sections are not the sole reason for a decreasing ΔV_t at higher fields. The decrease could be simply due to the fact that holes are swept out of the oxide faster at higher fields. This decrease will continue up to fairly large fields, as the mobility measurements of holes show almost a constant mobility up to 5.5 MV/cm with no signs of velocity saturation[100].

With negative voltages, ΔV_t shows a similar decrease at large negative voltages. In addition, beyond a certain amount of trapped charge, the threshold voltage shift goes through a minimum near the oxide threshold voltage.

The peak of the trap density is located approximately at the point where the potential is a

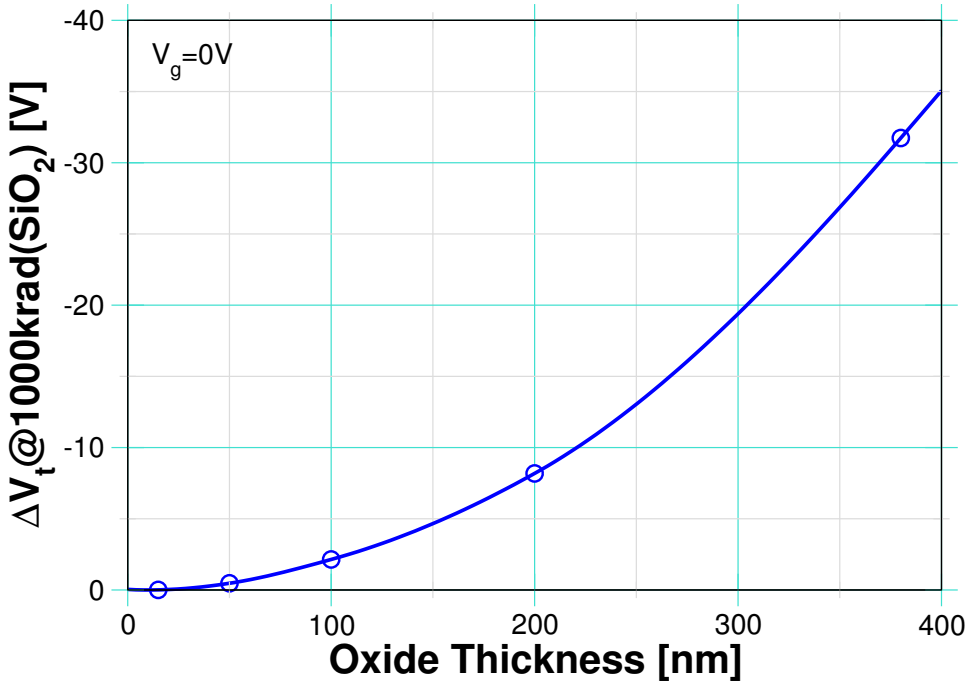

Figure 30: Variation of ΔV_t with oxide thickness at a total dose of 1 Mrad(SiO_2) with 0 V on the gate during radiation exposure.

maximum. Thus, the holes generated in the oxide tend to move away from the traps, leading to low values of ΔV_t.

Fig. 32 shows a curve (dashed line) with equal number of electron and hole traps in the oxide. This curve also has a minimum near zero oxide field. It is to be noted that although the yield is very low at low fields, zero field is almost never obtained throughout the oxide due to the large fields created by the trapped charge itself. However, at these low fields the initial trapping rate is very low, and it takes a long time for the trapped charge to build up. Fig. 32 shows the effect of shifting the centroid away from the Si-SiO_2 interface. It is seen that the ratio of the average at positive voltages to the average at negative voltages decreases. This is expected as for positive voltage the hole concentration increases towards the interface. But for negative voltages, the hole concentration reduces towards the interface, reducing the amount of trapped charge as the centroid is shifted toward the interface.

Fig. 32 shows a simulation in which electron traps have been included. The simulation was done using an oxide thickness of 380 nm with uniform distribution of electron and hole traps.

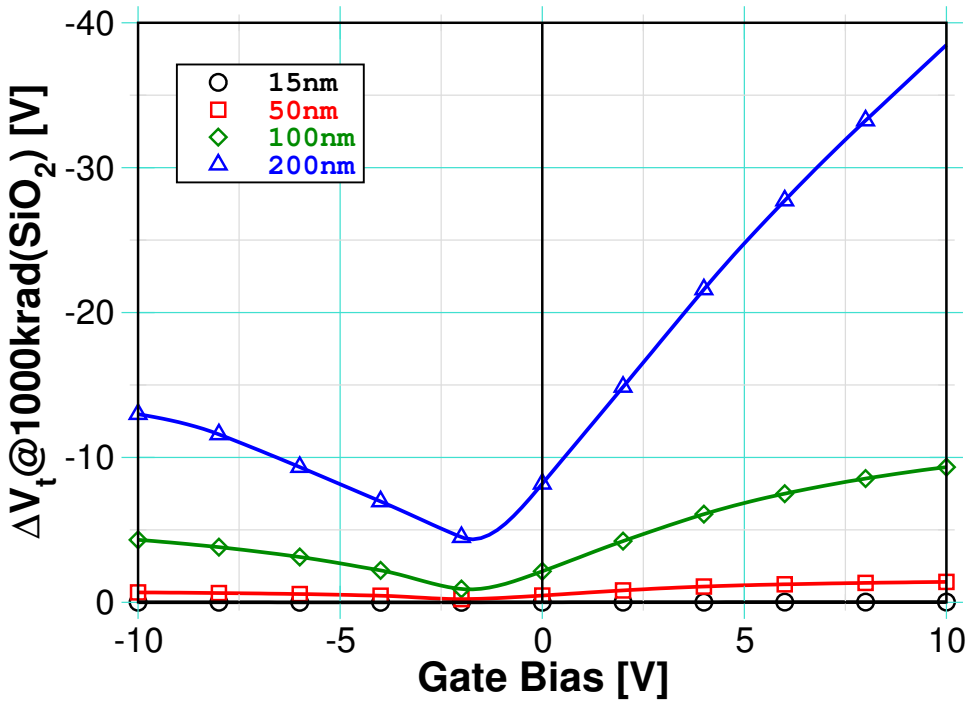

Figure 31: Variation of ΔV_t with gate voltage used during radiation exposure for various oxide thicknesses and after a total dose of 1 Mrad(SiO_2).

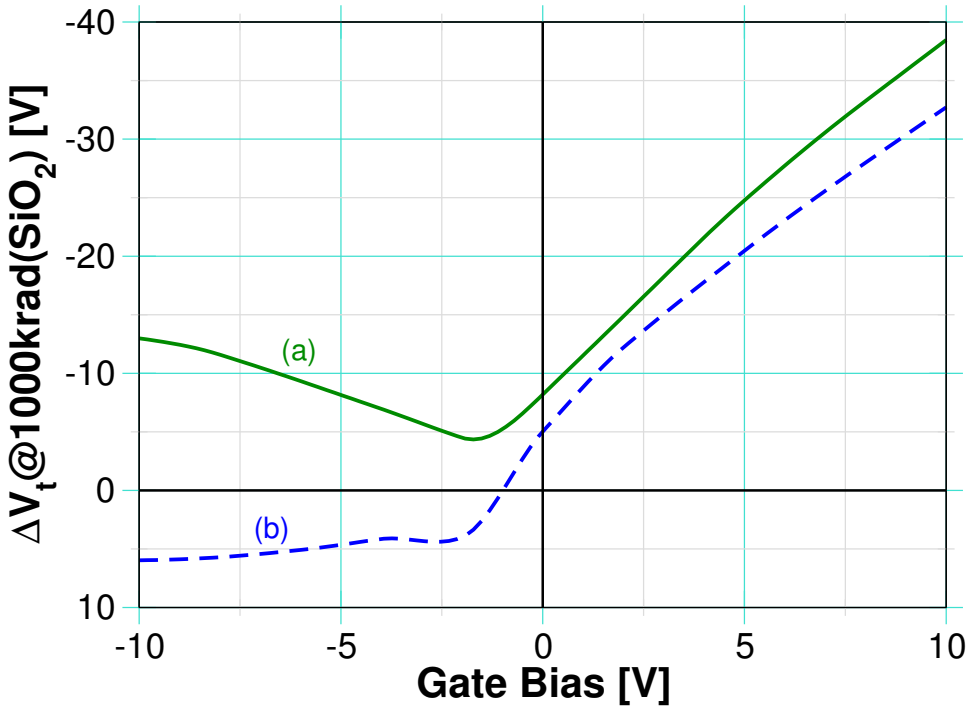

Figure 32: Dependence of ΔV_t on V_g for $t_{ox} = 200\ nm$ when electron traps are included in the simulation model. Curve (a) is obtained without electron traps for a total dose of 1 Mrad(Si), (b) is obtained with nearly equal electron and hole trap density using the same conditions as for (a).

Curve (a) was obtained without electron traps, and curve (b) was obtained for the same conditions with nearly equal electron and hole trap densities. It is seen that the addition of electron traps significantly alters ΔV_t at near-zero fields in the oxide. Elsewhere, the electron traps have no effect on ΔV_t. This is due to the relatively large mobility of electrons (20 cm^2/Vs as compared to 10^{-5} cm^2/Vs for holes), which leads to low electron concentrations in the oxide except when the field is low. At V_g = 0 V, ΔV_t is negative, indicating a greater shift due to electrons. It is seen that after increasing for a considerable amount of dose, ΔV_t begins to fall and eventually becomes positive. This decrease begins to occur when the field, due to the trapped charge, compensates for the applied and built in oxide field. If the positive charge builds up further, the oxide bands become concave with the potential minimum for electrons located near the centroid of the hole traps, which is near the centroid of the electron traps. Beyond this dose, electrons generated throughout the oxide move towards the minimum energy point of the conduction band and get trapped, thus compensating for the positive charge.

CHAPTER VII

DEVICE PHYSICS TO CIRCUITS

Development processes in microelectronics extend from specification of a system, to circuit and layout design, to questions of testability, reliability, and manufacturing. Due to the complexity of such systems, an efficient development process requires an overall design method and corresponding tool support. The modeling of circuit behavior has a pivotal role.

Circuit simulation programs, such as SPICE, are useful tools for the circuit or system designer, allowing the prediction of performance of complicated circuits and systems without building a breadboard. Simulation can save considerable time and money in the design cycle. However, the simulation of complex behaviors, such as device radiation response, requires model capability that is not included with the commercially available simulation framework.

This chapter discusses a generalized macromodeling methodology. This methodology is the capstone effort in the multi-level modeling of radiation effects, as it "propagates" the detailed physics captured in lower-level atomic, process and device modeling to a higher-level, the Compact Model (CM).

Macro Models

Besides modeling nominal device behavior, modeling space microelectronics requires the ability to explore designs capable of operation in a radiation environment. Macromodels should enable a designer to evaluate systems in the same manner, regardless of the system's subcomponents.

Types of Macro Models

Macromodels are divided into two types, primitive and composite. Primitives are either analytical (e.g., equations), empirical (look-up-table), or behavioral code (C, C++, Verilog-A/AMS or VHDL-AMS). Primitive models consist of base models, and a means in which their behavior can be modified and encapsulated. Composite models consist of a combination of other macromodels, either primitives or other composite models. Composite models provide not only the assemblage of other models, but the description as to how they interact. Creating a composite model of a system entails three steps:

1) The decomposition, or partitioning into subcomponents.

2) Associating these subcomponents with models to evaluate relevant issues.

3) The composition of these sub-components back into a single entity.

Models should be created and/or chosen based on a number of different properties. The major properties are:

- Accuracy
- Execution speed
- Creation time
- Adaptability

Knowledge of the important bounds of the input parameters is valuable in creating models. The following three sections detail the three superclasses of primitive models: analytical expressions, tables, and behavioral models.

Analytic Expressions

Once a behavior has been characterized, analytical expressions are usually the quickest means to analyze the impact on a design. An expression can range from a simple constant with no input parameters, to a complex expression with many inputs.

Analytical expressions can be derived either analytically or empirically, and can be used to model subcomponents at any level of hierarchy. Thus they can be used throughout the design process.

Equations are the fastest of all primitive models to evaluate and offer a wide range of accuracy.

Empirical (Look-up Table)

Tables are created empirically from either measurements or simulations. In addition, interpolation and extrapolation methods can be added to the model if the needed values are not precalculated. Tables are as accurate as the tool, or the measurement, utilized to create the table. Interpolation and extrapolation methods used to find things not in flow will increase the inaccuracy. Accuracy can be modeled in a number of different means for table look-up. If it is a consistent

error, a +/- of either a percentage or absolute amount could be included. If the accuracy is dependent upon the entry in the table, a second value can be included in the table to indicate the model accuracy.

Composite Models

Analyzing complex behaviors requires a partitioning of the system into manageable components. These components are than associated with appropriate sub-models, and than recomposed together for evaluation. This so called “divide and conquer” approach has been used at lower levels of abstraction. The goal of partitioning is to divide a behavior into manageable subparts, enumerating a list of the most important functions. A basic architecture, or pseudo-code, can be sketched of the behavior and components extracted in a list form.

The first step in the evaluation of the subcomponents of the behavior is to assign each subcomponent to either a primitive or composite macromodel using various methods. The direct method is simply to assign each component to a model. This is done by matching components with a macromodel from a list or done manually, using schematic capture or software parsing.

Compact Modeling Framework

The SILVACO SmartSPICE/Scholar tools provide the basic EDA mechanisms for implementation of macro-models at the primitive and composite level. Interfaces for C/C++ and Verilog-A/AMS were implemented, as well as some analog behavioral primitives that are detailed in Appendix E. Within this Compact Modeling Framework (CMF), one has the capability to draw from a library of primitive model components, associate behaviors, and look-up tables as time-value pairs, as described in Appendix F.

The CMF supports the creation of symbols used in schematic capture and associate the behaviors with C/C++ or Verilog-A/AMS. This framework also supports the association of expressions to parameters within a SPICE compact model.

Total Dose Composite and Primate Compact Macro Models

The design of electrical systems for military and space applications requires consideration of the effects of Total Ionizing Dose (TID), and Dose Rate (DR) radiation, as well as Single Event Effects (SEE) on system performance. Simulation of radiation effects using the Radiation Enhanced (RE) - Circuit environment helps to identify critical circuit components that could cause system

failure and gives guidance for radiation hardening of the system. The following information is intended to provide guidelines for those using the RE-Circuit environment for radiation effects analysis.

Within the RE-Circuit environment, all radiation effects analysis is done using models or macro models developed within the CMF. Symbols have been generated for both NMOS and PMOS devices for Total Ionizing Dose (TID), Dose Rate (DR), SEE, and the combination of DR given a TID, and SEE given a TID. A TID example will be described and then compared to our experimental data.

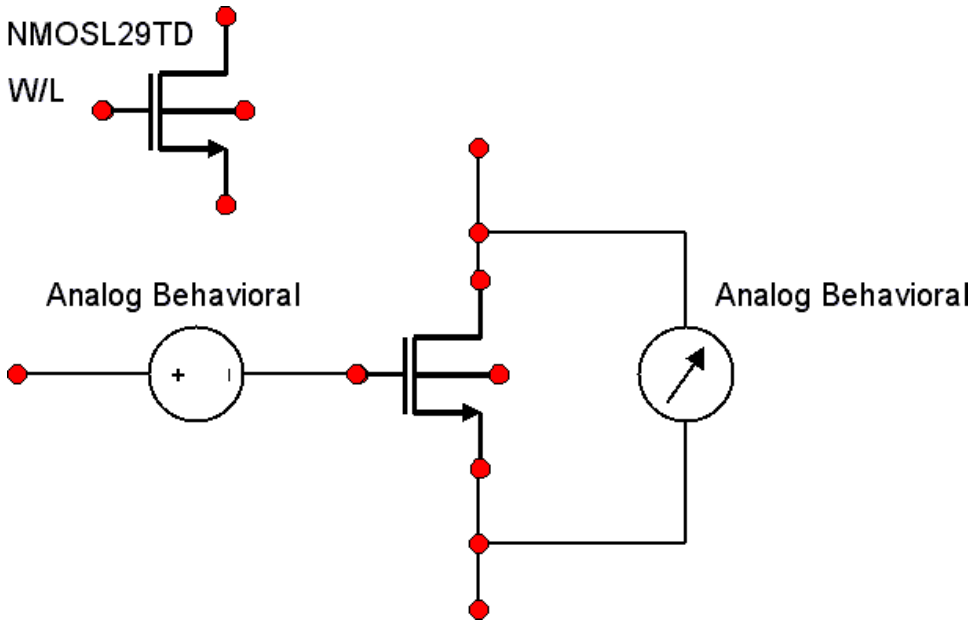

Figure 33: Underlying components of an analog behavioral macromodel for Total Ionizing Dose.

The composite Macro Models used to model total dose effects on SOI-MOSFETS in this work consist of three primitive elements: an SOI MOSFET Model and two analog behavioral elements as shown in Fig. 33.

The SOI MOSFET Model is a Partially-Depleted (PD) SOI MOSFET Model known as a Level 29 PD-SOI MOSFET in Silvaco's SmartSpice circuit simulator. It is a six terminal model with drain, gate, external body, internal body, source, and substrate terminals. The significance of the internal body terminal is the capability to inject charge into the body without the body resistance

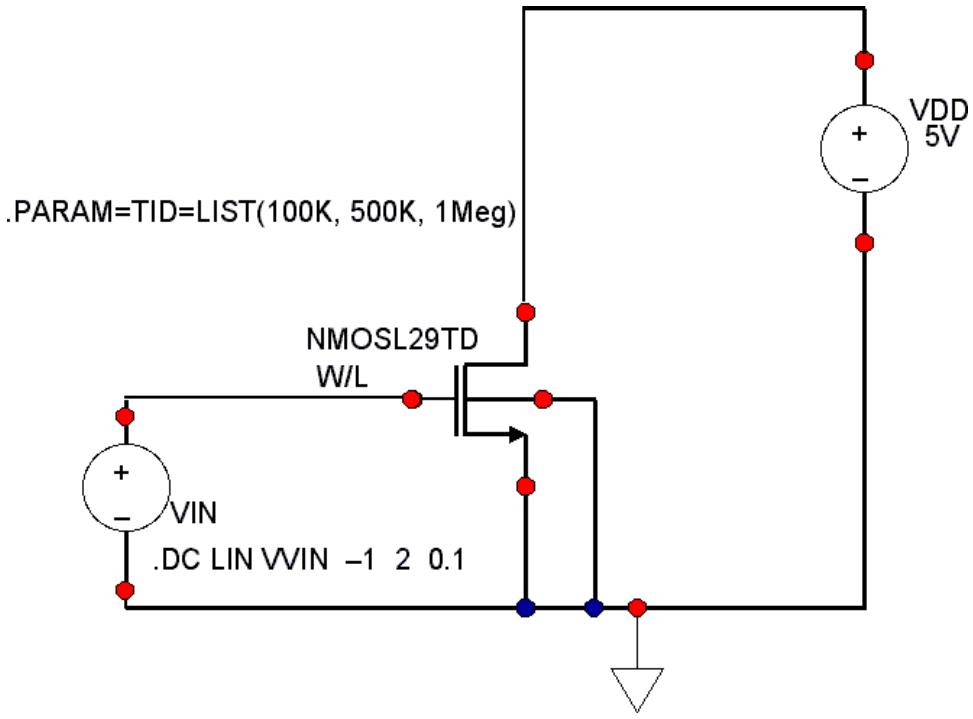

Figure 34: Circuit used to simulate the exposure of an NMOS-SOI transistor to a Total Ionizing Dose.

of the external body terminal. The model parameters listed in [101, 102, 103] are extracted and available within this composite model. The analog behavioral can be implemented as behavioral voltage/current source based on experimental data or from simulation data. In this illustration, simulation data from the previous chapter will be used.

A primitive model was developed using C/C++ and Verilog-A/AMS. Both implementations have a terminal symbol with substrate grounded that allows model use within schematic entry. The Verilog-A/AMS code is shown in Appendix G. This model has the most flexibility in that the charge in the oxide Q_{ox} is a variable that can be generated from the device simulator.

Both the composite and primitive compact models can be tied to a basic transistor symbol with Total Ionizing Dose as one of its parameters. This allows use of the .ST statement of SPICE, allowing TD to vary within the simulation, generating a family of curves for the designer to review. The simulation test circuit is shown in Fig. 34.

Experimental Results

Experimental data, presented in Tables 6 and 7 and Figures 35–37, were obtained from NAVSEA-CRANE on 0.8um PD-SOI devices manufactured at SPAWAR Systems Center, San Diego Cali-

fornia.

Table 6: Threshold voltage shift for device N2 ($V_D = 0.1$ V).

Dose	**Anneal Time**	ΔV_t	$\Delta\Delta V_t$
krad(SiO_2)	min	V	V
0	0	0	
100	1.5	-0.0562	
	10.0	-0.0520	0.0042
	18.5	-0.0504	0.0058
200	1.5	-0.0951	
	10.0	-0.0905	0.0046
	18.5	-0.0885	0.0066
500	1.5	-0.1899	
	10.0	-0.1808	0.0091
	18.5	-0.1691	0.0208
1000	1.5	-0.2513	
	10.0	-0.2287	0.0226
	18.5	-0.2252	0.0261

Simulation

A SPICE simulation was conducted using the Composite Macro-model, with the analog behavioral models implemented using a table generated from the device simulations from the previous chapter. The SPICE circuit simulation was carried out using a .DC sweep, with Total Dose(TD) test points at 0, 100 Krad, 500 Krad, 1000 Krad, at TNOM. The results are depicted in Figs. 35-37.

Methodology and Experimental Comparison

The objective of comparing experimental results with those numerically predicted, using the multi-level modeling methodology, was to obtain an objective measure of the level of confidence

Table 7: Threshold voltage shift for device N2 (V_D=5.0 V).

Dose	**Anneal Time**	ΔV_t	$\Delta\Delta V_t$
krad(SiO_2)	min	V	V
0	0	0	
100	5.5	-0.0557	
	14.0	-0.0531	0.0026
	22.5	-0.0527	0.0030
200	5.5	-0.0998	
	14.0	-0.0963	0.0035
	22.5	-0.0941	0.0057
500	5.5	-0.1945	
	14.0	-0.1907	0.0038
	22.5	-0.1881	0.0064
1000	5.5	-0.2638	
	14.0	-0.2502	0.0126
	22.5	-0.2461	0.0167

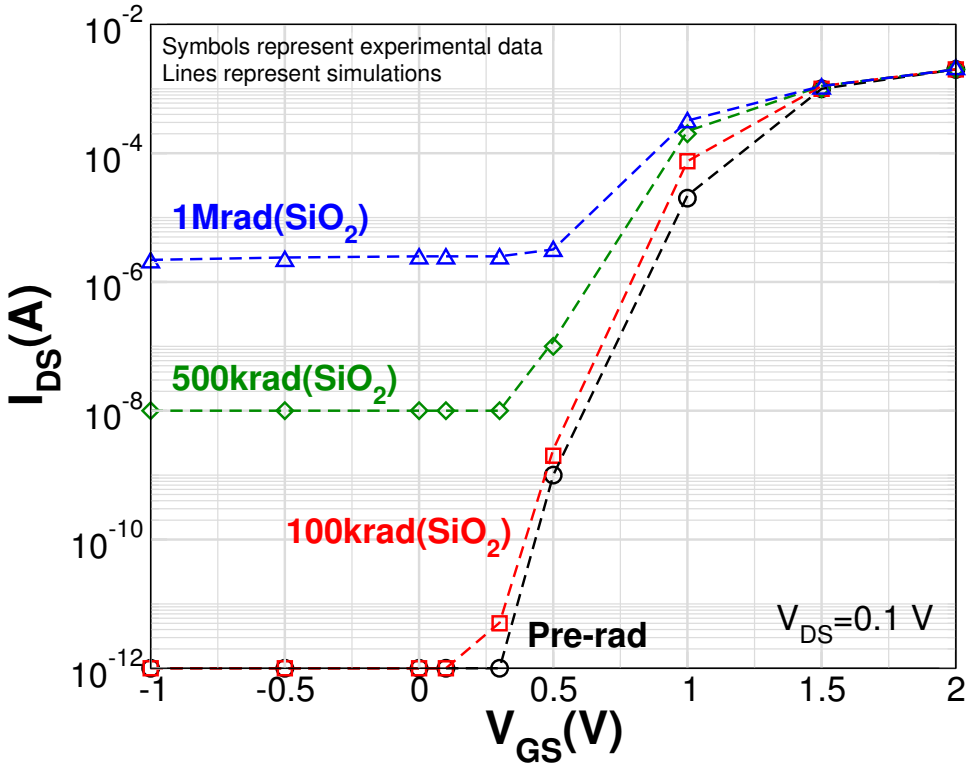

Figure 35: I_{DS} versus V_{GS} for device N2 at various dose levels and anneal times. The experiment was performed on 40 parallel $5.0\mu\text{m} \times 0.8\mu\text{m}$ with 1μm body ties resulting in an equivalent $200\mu\text{m} \times 0.8\mu\text{m}$ device. The irradiation was performed with $V_D = 5.0$ V, $V_G = V_S = V_B = V_{back} = 0.0$ V using a Co^{60} source at a dose rate of 140 rad(SiO_2)/s. The test sweep was performed at $V_D = 0.1$ V.

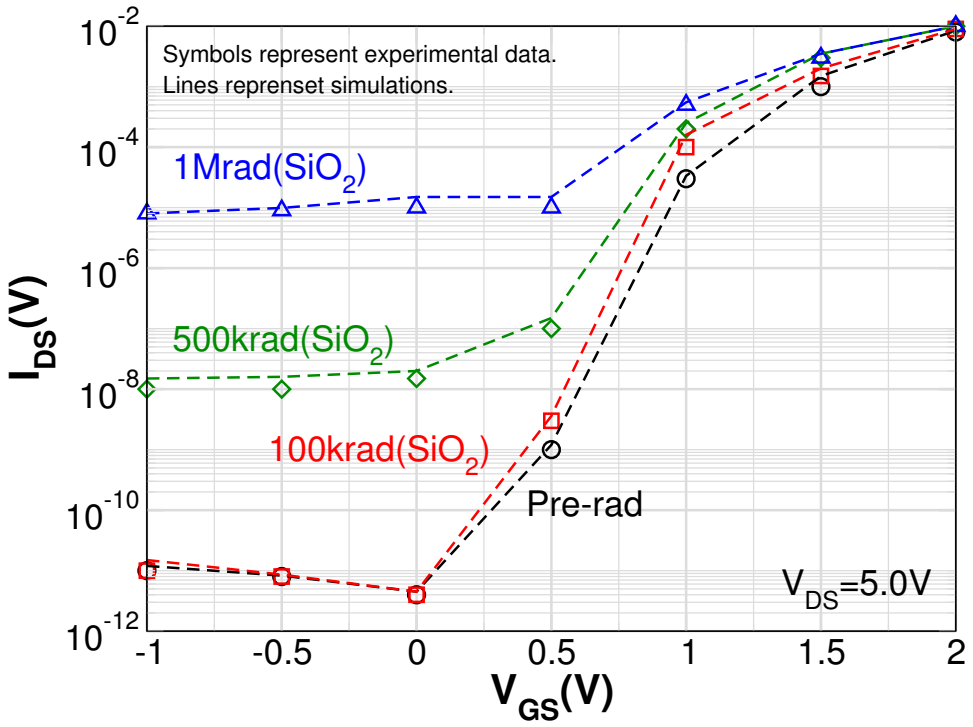

Figure 36: I_{DS} versus V_{GS} for device N2 at various dose levels and anneal times. The experiment was performed on 40 parallel $5.0\mu\text{m} \times 0.8\mu\text{m}$ with 1μm body ties resulting in an equivalent $200\mu\text{m} \times 0.8\mu\text{m}$ device. The irradiation was performed with $V_D = 5.0$ V, $V_G = V_S = V_B = V_{back} = 0.0$ V using a Co^{60} source at a dose rate of 140 rad(SiO_2)/s. The test sweep was performed at $V_D = 5.0$ V.

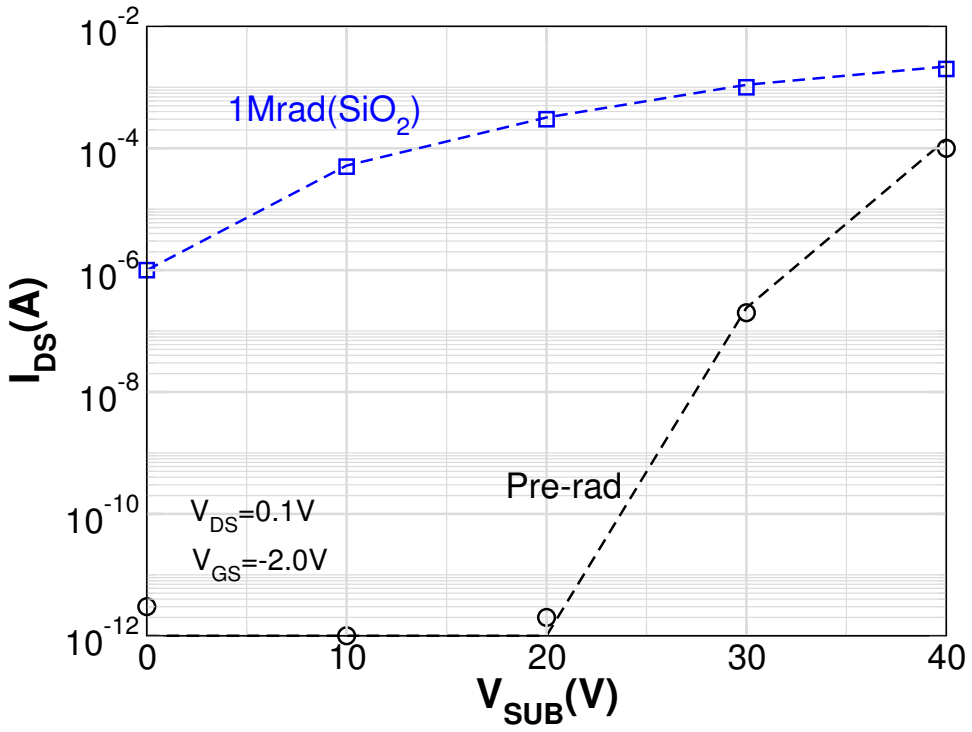

Figure 37: I_{DS} versus V_{sub} for device N2 prerad and postrad. Symbols represent experimental data while lines represent simulation results.

regarding correctness. These are two important types of information that are to be gained from the validation effort: 1) the establishment of the limits of the multi-level modeling methodology, and 2) the achievement of as narrow as possible limits on the accuracy of the methodology. It is equally important to quantify the accuracy of the methodology as it is to achieve a particular level of accuracy. Without the determination of the accuracy, satisfactory predictions cannot be made.

Sources of Error

There are four sources of error that need to be considered in performing an error analysis of the accuracy of the code. These are:

1) Numerical computation errors

2) Measurement and instrumentation errors

3) Fabrication errors

4) Theory errors

The numerical computation errors are errors in the computation that result from factors such as round off, truncation, convergence criteria, and approximations in the numerical method. Quantifying these errors is the task of a verification and benchmarking program, and is not dealt with here.

The measurement and fabrication errors are accounted for directly, while the errors of theory are, by definition, those errors not accounted for by the other possible error sources.

Comparison and Validation

For the purpose of the validation of the multi-level methodology, it is essential that our simulation be compared with experimental data. Data from the experiment described in the Experimental Results section are used.

The comparison of these simulations with experimental data shown in Figures 35–37 appears to validate the present multi-level methodology. The absolute percentage error between simulated and experimental results varies between 1-5%.

The simulations used no non-physical parameters. All information used to generate the multi-level models for the analysis of TID effects on SOI-MOS devices involved results generated from our simulations and actual processing data.

To analyze other devices and effects of TID it might be necessary to adjust:

- The weighting algorithm used to calculate maximum temperature at which the oxide is exposed. This affects the [Family of E′-centers].
- The percentage of E'_{γ}, $E'_{\gamma 4}$, and $E'_{\gamma 5}$ precursors within the [Family of E′-centers].
- Improve the current algorithm for approximating the neutral capture cross-sections for electrons and holes, as well as their emission rates.

It can therefore be concluded that the multi-level modeling methodology can be used to solve Total Ionizing Dose problems for similar geometries and conditions.

Conclusion

The time behavior of positive charge in a-SiO_2 after irradiation is a complex process involving trapping of holes in the oxide, the generation of interface states at the Si/SiO_2 boundary, the tunneling of electrons from the substrate into the oxide, and the subsequent annihilation of some of

the trapped holes. A continuing goal of radiation effects work has been the development of models that can predict the complex radiation response of MOS devices, and circuits based on the process parameters used to fabricate the devices. Implementation of these models into a CAD framework would create a powerful tool that would make rapid design of rad hard parts possible with a minimum of build and test cycles, while at the same time minimizing performance and cost tradeoffs. To this end, it is essential to develop models that are based on physical understanding.

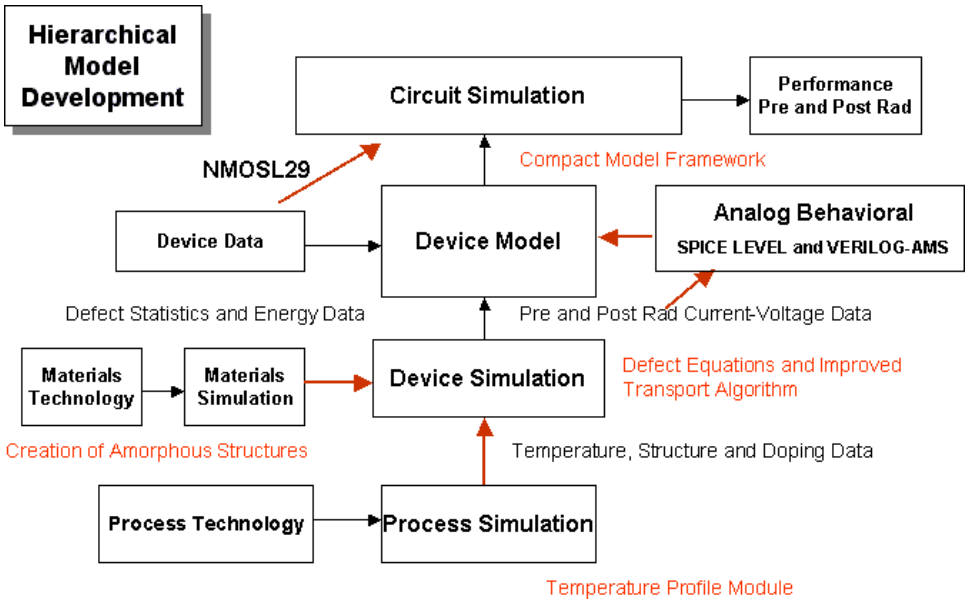

Figure 38: Hierarchical Model Development flowchart.

A multi-level methodology has been presented, as seen in Fig. 38 that allows one to examine TID effects on circuits. This multi-level methodology extends the work of Conley et al.[18] and of Milanowski[104]. This unified multi-level methodology uses the work of Conley et al. to define the initial concentration of precursors within the oxide. The population is then divided into E'_{γ}, $E'_{\gamma 4}$, and $E'_{\gamma 5}$ pre-cursors spatially and energetically using the results of Chapter IV. The results of Chapter V assist in resolving the role of hydrogen in interface trap formation, which involves the transport of several forms of hydrogen (H_0, H^+ and H_2).

The device simulator is an enhancement to the work of Milanowski [105]. The simulator also provides dispersive transport of all three carriers based on standard drift-diffusion equations, and incorporates the work described in Chapters III and IV providing dispersive transport models for holes as well as protons based on the theory of multiple trapping and detrapping (MTD) processes.

Chapter VI describes the unification process of Chapters II– V to achieve a macromodel capable of predictively modeling TID effects. This unification effort is depicted in Fig. 39 and is accomplished with a design flow used by commercial industry.

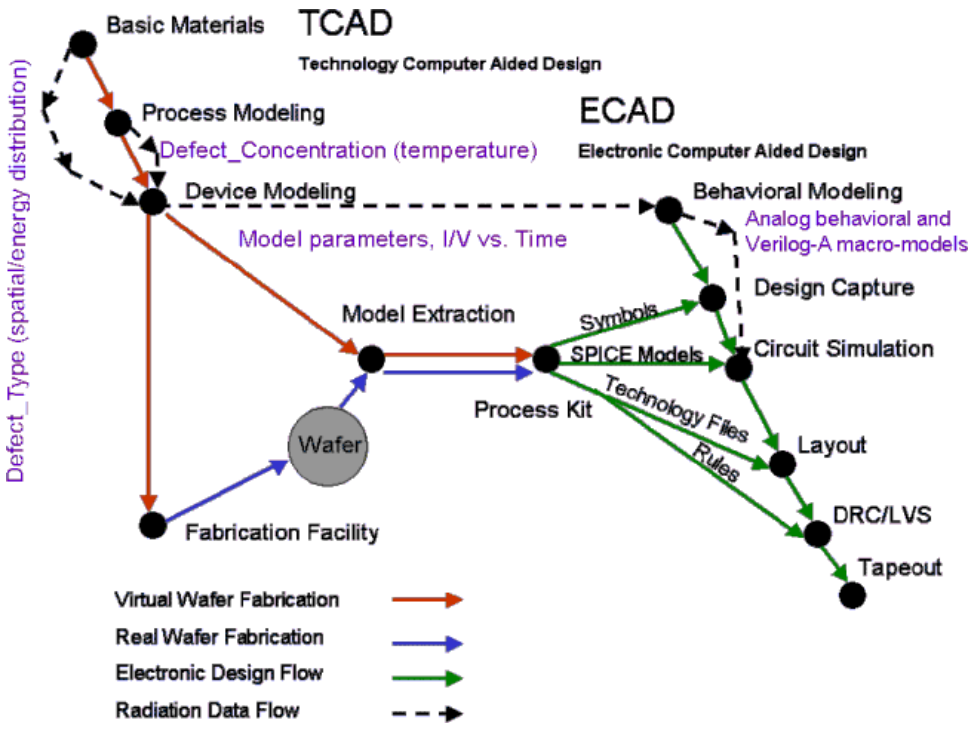

Figure 39: Design flow used by commercial industry for predictive modeling of TID effects.

The excellent quantitative agreement between our multi-level model, and experimental results, validates the hierarchical approach to modeling the radiation response of MOSFET's. Our results are particularly significant because they represent, to the best of our knowledge, the first multi-level physically-based model that allows quantitative predictions of radiation-induced performance changes. The match between the multi-level model's results and experimental data indicates that the ultimate goal of physically-based predictive modeling is attainable.

The past few decades have witnessed a dramatic advancement in integrated circuit technologies as a result our improved understanding of transistor physics, and the ability to model at various levels of abstraction. As the technology continues to scale to 130nm and below, it will become more difficult to model deep sub-micron effects, and the associated higher order physics that would ultimately lead to a unified compact model useful for circuit simulations. The multilevel methodology allows the integration of ab initio, technology computer-aided design (TCAD), and electronic de-

sign tools for designing and analyzing circuits operating in harsh environments. This multi-Level engineering approach supports the implementation of physics-based compact models (CM's) that allow one to bridge the gaps between basic mechanisms, technology developers and circuit designers, and provides the support for systems engineering.

The use of the multi-level engineering methodology described in this dissertation has allowed us to analyze and predict the behavior of a transistor exposed to radiation. The matching of experimental data provides the base on which to build upon and further refine this multilevel modeling methodology.

Appendix A

THE THEORY OF ELECTRONIC STRUCTURE CALCULATIONS

Introduction

It is ideal to solve the Schrödinger equation, Eq. (47), for N interacting electrons moving under the influence of an external potential due to atomic nuclei:

$$\left[-\frac{1}{2}\sum_{i=1}^{N}\nabla_i^2-\sum_{i,\alpha}\frac{Za}{|\mathbf{r}_i-\mathbf{R}_\alpha|}+\frac{1}{2}\sum_{\alpha\neq\beta}\frac{Z_\alpha Z_\beta}{|\mathbf{R}_\alpha-\mathbf{R}_\beta|}+\frac{1}{2}\sum_{i\neq j}\frac{1}{r_i-r_j}\right]\Psi=E\Psi \tag{47}$$

where Ψ is the N-electron wavefunction, $\mathbf{r}_i$ are the positions of the electrons, $\mathbf{R}_{\alpha,\beta}$ are the positions of the nuclei, and $Z_{\alpha,\beta}$ are the charges on the nuclei.

Hartree Theory

Hartree theory starts from the single particle Schrödinger equation (48):

$$-\frac{1}{2}\nabla^2\psi(r)+U(r)\psi(r)=E\psi(r) \tag{48}$$

where ψ is the one electron wavefunction, and U(r) is the effective potential. This effective potential is due to the nuclei at $\mathbf{R}_i$, and that of the other electrons. The electrostatic attraction of the nuclei is expressed by equation (49).

$$U_{nuc}(\mathbf{r})=-\sum_a\frac{Z_a}{|\mathbf{r}-\mathbf{R}_a|} \tag{49}$$

The effect of the other electrons is included by an approximation. It is assumed that the potential is dependent only on the average charge density of the other electrons, given by equation (50).

$$U_{el}(\mathbf{r})=\sum_{j\neq i}\int\frac{n_j(\mathbf{r}')}{|\mathbf{r}-\mathbf{r}'|}\mathbf{dr}' \tag{50}$$

where for each single particle electronic state, the charge density is given by:

$$n_i(\mathbf{r})=|\psi_i(\mathbf{r})|^2 \tag{51}$$

where ψ_i are the orthonormal one electron wave functions. The total electronic charge density is then given by:

$$n(\mathbf{r}) = \sum_i |\psi_i(\mathbf{r})|^2 \tag{52}$$

where the sum is over the occupied one electron states. $U(\mathbf{r})$ is replaced in Eq. (48) by Eq. (53).

$$U(\mathbf{r}) = U_{nuc}(\mathbf{r}) + U_{el}(\mathbf{r}) \tag{53}$$

This leads to N single particle equations, the Hartree equations (54):

$$-\frac{1}{2}\Psi_i(\mathbf{r}) + U_{\text{nuc}}(\mathbf{r})\Psi_i(\mathbf{r}) + \sum_{j\neq i}\int \frac{1}{|\mathbf{r}-\mathbf{r}'|}\left|\Psi_j(\mathbf{r}')\right|^2 \Psi_i(\mathbf{r})d\mathbf{r} = \varepsilon_i\Psi_i(\mathbf{r}) \tag{54}$$

Solving Eq. (54) iteratively gives the occupied energy levels.

The above Hartree equations, Eq. (54), are then minimized with respect to energy using a wave function of the form:

$$\Psi = \prod_i \psi_i(\mathbf{r}_i) \tag{55}$$

The total electronic wavefunction produced by Eq. (55) is always symmetric with respect to the interchange of particles. The Pauli principle states that the total wavefunction must be asymmetrical, which moves one to Hartree-Fock theory.

Hartree-Fock Theory

Hartree-Fock theory allows the total electronic wavefunction to be asymmetric with respect to the interchange of particles, resolving symmetry problems with Hartree theory. The total electronic wavefunction is represented by the determinant of the theory. The electronic wavefunctions are represented by the determinant of an $\mathrm{N}\times\mathrm{N}$ matrix of single particle wavefunctions, matrix of

single particle wavefunction:

$$\Psi(\mathbf{r}_1\mathbf{s}_1,\mathbf{r}_2\mathbf{s}_2,\ldots,\mathbf{r}_N\mathbf{s}_N) = \begin{vmatrix} Y_1(\mathbf{r}_1\mathbf{s}_1) & Y_1(\mathbf{r}_2\mathbf{s}_2) & \cdots & Y_1(\mathbf{r}_N\mathbf{s}_N) \\ Y_2(\mathbf{r}_1\mathbf{s}_1) & Y_2(\mathbf{r}_2\mathbf{s}_2) & \cdots & Y_2(\mathbf{r}_N\mathbf{s}_N) \\ \cdots & & & \\ \cdots & & & \\ \cdots & & & \\ Y_N(\mathbf{r}_1\mathbf{s}_1) & Y_N(\mathbf{r}_2\mathbf{s}_2) & \cdots & Y_N(\mathbf{r}_N\mathbf{s}_N) \end{vmatrix} \tag{56}$$

This Slater determinant is a linear combination of the permutations of the wave function obtained from Eq. (55).

$$\Psi = Y_1(\mathbf{r}_1\mathbf{s}_1)Y_2(\mathbf{r}_2\mathbf{s}_2)\ldots Y_N(\mathbf{r}_N\mathbf{s}_N) - Y_1(\mathbf{r}_2\mathbf{s}_2)Y_2(\mathbf{r}_1\mathbf{s}_1)\ldots Y_N(\mathbf{r}_N\mathbf{s}_N) + \ldots \tag{57}$$

Applying the variation principle to Eq. (47), and minimizing the energy with respect to a wavefunction of the form given by Eq. (56) leads to N single particle Hartree-Fock equations:

$$-\frac{1}{2}\nabla^2\Psi_i(\mathbf{r}) + U_{\text{nuc}}(\mathbf{r})\Psi_i(\mathbf{r}) + U_{\text{el}}(\mathbf{r})\Psi_i(\mathbf{r}) + \nu_i^{\text{HF}}\Psi_i(\mathbf{r}) = E_i\Psi_i(\mathbf{r}) \tag{58}$$

Here, ν_i^{HF} is the average potential experienced by the i^{th} electron due to the presence of the other electrons. This is the Hatree-Fock approximation which replaces the complicated many electron problem by a one electron problem in which the electron-electron repulsion is treated in an average way.

The Hartree-Fock potential (ν_i^{HF}) is the field seen by the electron. This field depends on the spin orbital's of the other electrons. This coupling produces non-linear equations that must be solved iteratively. This iterative procedure is called the Self-Consistent-Field (SCF) method. This method makes an initial guess at the spin orbitals calculating ν_i^{HF}, seen by each electron, and then solves the eigenvalue equation, Eq. (58), for a new set of spin orbitals. Using these new spin orbitals, it is possible to obtain new fields, and repeat the procedure until self-consistency is reached. Self consistency being defined as the point at which the fields no longer change from one iteration to another.

Thomas-Fermi Theory

Thomas-Fermi theory is an early form of density functional theory. The starting point for the theory is the charge density, **n**, of a uniform electron gas. The Pauli exclusion principle, together with boundary conditions, states that only two electrons with opposite spin can occupy a volume of h^3 in phase space. A uniform electron gas in its ground state has electrons with momenta up to p_f, the Fermi momentum corresponding to the Fermi energy (ε_f). Therefore, the phase space volume occupied by an electron gas enclosed in a box of volume V is $\frac{4}{3}\pi p_f^3 V$. The number of electrons is given by:

$$N = \frac{\frac{4}{3}\pi p_f^3 V}{h^3} \tag{59}$$

and the charge density is:

$$n = \frac{N}{V} = \frac{8\pi p_f^3}{3h^3} \tag{60}$$

An assumption is made that the charge density at a point **r** in a non-uniform electron gas can be approximated by a charge density of a uniform electron gas at the point, n(**r**). This allows Eq. (60) to be rewritten as:

$$n(\mathbf{r}) = \frac{1}{3\pi^2}\left(\frac{p_f(\mathbf{r})}{\hbar}\right)^3 \tag{61}$$

Using classical theory, the Fermi energy, ε_f, can be expressed as:

$$\varepsilon_f = \frac{p_f^2(\mathbf{r})}{2m} + V(\mathbf{r}) \tag{62}$$

Here, $\frac{p_f^2}{2m}$ is the classical kinetic energy of an electron with momentum p_f and $V(\mathbf{r})$ is the external potential. Substituting Eq. (61) into Eq. (62) to eliminate $p_f(\mathbf{r})$, and writing the energy in terms of the charge density gives:

$$\varepsilon_f = \frac{\hbar^2}{2m}\left[3\pi^2 n(\mathbf{r})\right]^{\frac{2}{3}} + V(\mathbf{r}) \tag{63}$$

This expression makes it possible to obtain the minimum total energy of an electronic system with respect to the charge density. An expression for the total energy of an electronic system gas

is given by:

$$E_{\text{el}} = E_K + U_{\text{el}-\text{el}} + U_{\text{el}-\text{nuc}} \tag{64}$$

Here, E_K is the kinetic energy, $U_{\text{el}-\text{el}}$ is the energy due to electron-electron interaction, and $U_{\text{el}-\text{nuc}}$ is the electron-nucleus interaction energy. The kinetic energy per unit volume at a point **r** is defined as:

$$E_K(\mathbf{r}) = \int_0^{pf(\mathbf{r})} n(\mathbf{r}) \frac{p^2}{2m} P(p) dp \tag{65}$$

Here, **P**(p) is the probability distribution or density of states of electronic momenta in the electron gas. The probability of an electron having momentum between p and p + dp is the ratio of the volume of the shell at radius p in momentum space of thickness dp to the volume of the sphere enclosing all the electrons of radius p_f:

$$P(p) = \begin{cases} \frac{4\pi p^2 dp}{\frac{4}{3}p^3 f(r)} & \text{for } p < pf(r) \\ 0 & \text{otherwise} \end{cases} \tag{66}$$

Substituting Eq. (66) into Eq. (65), we get:

$$E_K(\mathbf{r}) = \int_0^{pf(\mathbf{r})} n(\mathbf{r}) \frac{p^2}{2m} \frac{3p^2}{p^3 f(\mathbf{r})} dp \tag{67}$$

Using Eq. (61), the total kinetic energy is hence,

$$E_{K_T} = \int E_K(\mathbf{r}) d\mathbf{r} = \frac{3}{5}\frac{\hbar^2}{2m}\left(3\pi^2\right)^{\frac{2}{3}} \int [n(\mathbf{r})]^{\frac{5}{3}} d\mathbf{r} \tag{68}$$

The electrostatic interaction terms are given by:

$$U_{\text{el - nuc}} = \int n(\mathbf{r}) V_{nuc}(\mathbf{r}) d\mathbf{r} \tag{69}$$

$$U_{\text{el - el}} = \frac{1}{2} e^2 \int \frac{n(\mathbf{r}) n(\mathbf{r}')}{|\mathbf{r} - \mathbf{r}'|} d\mathbf{r} d\mathbf{r}' \tag{70}$$

where, $V_{nuc}(\mathbf{r})$ is the potential due to the nucleus. Substituting Eqs. (68), (69), and (70) into Eq. (64), we get:

$$E_{el} = \alpha \int [n(\mathbf{r})]^{\frac{5}{3}} d\mathbf{r} + \int n(\mathbf{r}) V_{nuc}(\mathbf{r}) d\mathbf{r} + \frac{1}{2} e^2 \int \frac{n(\mathbf{r}) n(\mathbf{r}')}{|\mathbf{r} - \mathbf{r}'|} d\mathbf{r} d\mathbf{r}' \tag{71}$$

where,

$$\alpha = \frac{3}{5} \frac{\hbar^2}{2m} \left(3\pi^2\right)^{\frac{2}{3}} \tag{72}$$

The minimization of Eq. (71) with respect to $n(\mathbf{r})$ is carried out under the constraint:

$$N = \int n(\mathbf{r}) d\mathbf{r} \tag{73}$$

Using a Lagrange multiplier, μ, to handle Eq. (73), we get:

$$\frac{\delta}{\delta n(\mathbf{r})} (E - \mu N) = 0 \tag{74}$$

We obtain the expression for the Lagrange multiplier:

$$\mu = \frac{5}{3} \alpha [n(\mathbf{r})]^{\frac{2}{3}} + V_{nuc}(\mathbf{r}) + e^2 \int \frac{n(\mathbf{r}')}{|\mathbf{r} - \mathbf{r}'|} d\mathbf{r}' \tag{75}$$

where, μ is also equivalent to the chemical potential of the system and can be seen from:

$$\mu = \frac{\partial E}{\partial N} \tag{76}$$

Density Functional Theory

Density functional theory is an accurate ab initio theory which has proven extremely powerful since its inception in 1964. In this appendix, we describe the basic ideas underlying the theory used to solve the many-body problem. This is not meant to be an in depth analysis of this theory. For a deeper understanding, refer to works by Hohenberg and Kohn[61, 62], Parr and Yang[64, 43]. and Jones and Gunnarsson[106].

Hohenberg and Kohn[61] proved two theorems which simplified the problem of calculating electronic structure. For a system of N electrons, the Schrödinger equation and density operators can be written as:

$$\hat{H}\Psi = E\Psi \tag{77}$$

$$\hat{H} = \sum_{i=1}^{N}\left(-\frac{1}{2}\nabla_i^2\right) + \sum_{i}^{N} v(\mathbf{r}_i) + \sum_{i<j}^{N}\frac{1}{r_{ij}} \tag{78}$$

$$\rho(\mathbf{r}_i) = N\int\cdots\int |\Psi(r_1, r_2, \ldots, r_N)|^2 dr_2 \ldots dr_N \tag{79}$$

where, $\Psi(r_1, r_2, \ldots, r_N)$ is the many electron wavefunction, $\hat{H}$ is the Hamiltonian, and $\rho(\mathbf{r}_i)$ is the electron density at $\mathbf{r}_i$. The ground state energy and wavefunction can be found by minimizing the energy with respect to Ψ; for a given system, the ground state wavefunction, and hence the charge density, is wholly determined by N, the number of electrons, and $v(\mathbf{r})$, the external potential, generally due to the atoms.

Hohenberg-Kohn theorem simplifies the many body problem by proving that to within an additive constant, $v(\mathbf{r})$ and N are determined by $\rho(\mathbf{r})$. This reverses the previous statement that $v(\mathbf{r})$ determines $\rho(\mathbf{r})$ allowing one to write:

$$E_v[\rho] = T[\rho] + V_{ne}[\rho] + V_{ee}[\rho] \tag{80}$$

$$V_{ne}[\rho] = \int \rho(\mathbf{r})v(\mathbf{r})d\mathbf{r} \tag{81}$$

where the square brackets denote functional, E_v represents the energy as a functional of ρ for a given $v(\mathbf{r})$ and T; V_{ne}, and V_{ee} are the kinetic, electron-ion, and electron-electron energies respectively.

The work of Hohenberg and Kohn shows that for any trial density, $\bar{\rho}(\mathbf{r})$, which satisfies the physical conditions that $\bar{\rho}(\mathbf{r}) \geq 0$ and $\int \bar{\rho}(\mathbf{r})d\mathbf{r} = N$:

$$E_{v,\text{Ground state}} \leq E_v[\bar{\rho}] \tag{82}$$

This allows the minimum system energy to be given by the ground state charge density only, and that charge density is formed from the ground state wavefunction. This allows for charge density to be treated as a variational parameter in minimization.

Kohn and Sham[62] continued the development of this reformulation to a point where the theory became useful. They performed additional reformulations, constructing non-interacting on-electron wavefunctions, and lumped all the many-body interactions into one functional, known as the exchange-correlation functional.

Recalling that system energy can be written as a functional of charge density:

$$E[\rho] = \int \rho(\mathbf{r})\nu(\mathbf{r})d\mathbf{r} + T[\rho] + V_{ee}[\rho] \tag{83}$$

Kohn and Sham defined a set of non-interacting wavefunctions, Ψ_i, which move in an effective potential:

$$\nu_{\text{eff}}(\mathbf{r}) = \nu(\mathbf{r}) + \int \frac{\rho(\mathbf{r}')}{|\mathbf{r}-\mathbf{r}'|}d\mathbf{r}' + \nu_{xc}(\mathbf{r}) \tag{84}$$

where $\nu_{xc}(\mathbf{r})$, the exchange-correlation potential is given by $\delta E_{xc}[\rho]/\delta\rho(\mathbf{r})$ and the Ψ_i's satisfy:

$$\left[-\frac{1}{2}\nabla^2 + \nu_{\text{eff}}(\mathbf{r})\right]\Psi_i = \varepsilon_i\Psi_i \tag{85}$$

$$\rho(\mathbf{r}) = \sum_i^N |\Psi_i(\mathbf{r})|^2 \tag{86}$$

The exchange and correlation energy can be written as:

$$E_{\text{xc}}[\rho] = T[\rho] - T_s[\rho] - V_{ee}[\rho] - J[\rho] \tag{87}$$

$$J[\rho] = \frac{1}{2}\int\int \frac{\rho(\mathbf{r})\rho(\mathbf{r}')}{|\mathbf{r}-\mathbf{r}'|}d\mathbf{r}d\mathbf{r}' \tag{88}$$

where, $T_s[\rho]$ is the kinetic energy for non-interacting electron gas, $T[\rho]$ is the kinetic energy for the full electron gas, and $J[\rho]$ is the Coulomb integral for the electrons. Now all the difficult calculations have been placed into a single term, $E_{\text{xc}}[\rho]$.

The exchange energy of a system of electrons is associated with the Pauli principle. In that, two electrons of the same spin must have a spatial separation, reducing the electron-electron repulsion energy. The correlation energy is defined to be the difference between the correct many-body energy and the Hartee-Fock energy, which puts in the exchange integral between two electrons, but assumes there is no correlation.

The simplest approach in DFT is Local Density Approximation (LDA), where for each point in space with a density $\rho(\mathbf{r})$, the exchange and correlation energy at that point is that of a uniform electron gas with density $\rho(\mathbf{r})$:

$$E_{xc}^{LDA}[\rho] = \int \rho(\mathbf{r})\varepsilon_{xc} d\mathbf{r} \tag{89}$$

$$V_{xc}^{LDA}(\mathbf{r}) = \frac{\delta E_{xc}^{LDA}}{\delta \rho(\mathbf{r})} \tag{90}$$

$$= \varepsilon_{xc}(\rho) + \rho(\mathbf{r})\frac{\delta \varepsilon_{xc}(\rho)}{\delta \rho} \tag{91}$$

where, $\varepsilon_{xc}(\rho)$ is the exchange and correlation energy for a uniform electron gas of density ρ. The exchange energy is represented by:

$$E_{x}^{LDA} = -\frac{3}{4}\left(\frac{3}{\pi}\right)^{\frac{1}{3}} \int \rho(\mathbf{r})^{\frac{4}{3}} d\mathbf{r} \tag{92}$$

and the correlation energy interpolated from the work of Ceperly and Alder[107].

Improvements to the exchange energy used by LDA can be done by considering the gradient of the density, ρ. This proposed correlation is called Generalized Gradient Approximation (GGA). There have been a number of GGA's proposed[43] which use an empirical form to include the gradient of the electron gas, as well as its value in the correlation calculations.

Appendix B

BASIC MOS PHYSICS

Introduction

Metal-oxide semiconductor (MOS) technologies have been the focus of radiation research over the past twenty years or so because of this technology's dominance in commercial and Department of Defense space market. A dominant effect associated with radiation induced ionization in electronic materials is trapped-charge buildup. This trapped charge induces internal fields that interfere with the designed operation and control of semiconductor devices. Insulating oxides, used in the manufacturing process of semiconductor technologies, determine the major effects of radiation associated with the technology. To understand the operational effects of radiation on a Metal-Oxide Semiconductor Field-effect Transistor (MOSFET), it is essential to grasp the physics of its operation with no irradiation. The second half of this chapter will discuss the physics of partially depleted silicon-on-insulator devices for which this dissertation analysis total ionizing dose effects.

Metal Oxide Semiconductor (MOS) System

The basic MOS system is shown in Fig. 40. It consists of a silicon substrate on which an oxide layer (SiO_2- an insulator) has been grown, usually using thermal oxidation. A metal is then deposited onto the oxide using physical vapour deposition, or other metalization process.

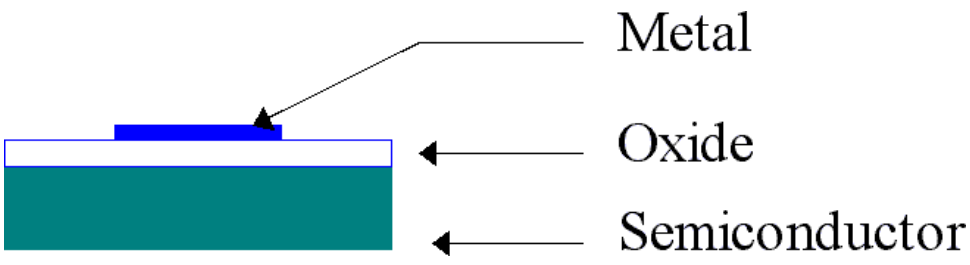

Figure 40: Structure of a MOS system.

Energy Band Structure

The energy band structure for an idealized system where the work function of the metal is equal to that of the semiconductor is shown in Fig. 42(a). Individual band diagrams are shown in

Fig. 42(b) for the common system Aluminum, Silicon Dioxide, and Silicon (p-type).

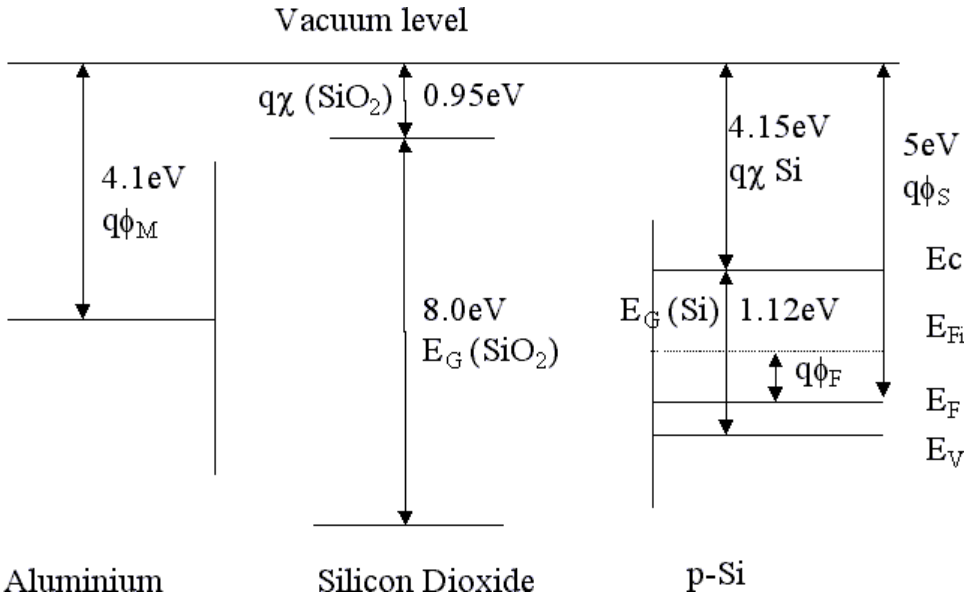

Figure 41: Band diagrams for Aluminum, SiO_2, and p-type Silicon.

Silicon dioxide is an insulator with a large energy gap in the range of 8-9 eV. It is convenient to relate the band structures of all three materials of the MOS system to a common reference potential, the vacuum level. The vacuum level is defined as the energy level at which the electron is free, in other words no longer bonded to the lattice. In silicon, the vacuum level is 4.05 eV above the conduction band. An electron at the conduction band edge must gain a kinetic energy of 4.05 eV (called the electron affinity, χ) in order to break loose from the crystal field of the silicon. In SiO_2, the vacuum level is 0.96 eV above the conduction band, which means that the potential barrier is 4.05 eV - 0.95 eV = 3.1 eV between the conduction band of Si and SiO_2. In metals, the energy difference between the vacuum level and the Fermi level is called the work function of the metal. The work function of Si is given by:

$$\Phi_S = \chi + \frac{E_g}{2q} + kT \ln\left(\frac{N_A}{n_i}\right) \quad \text{p-type Si} \tag{93}$$

$$\Phi_S = \chi + \frac{E_g}{2q} - kT \ln\left(\frac{N_D}{n_i}\right) \quad \text{n-type Si} \tag{94}$$

Flat-Band and Accumulation

When there is no applied voltage between the metal and the silicon, their Fermi levels line up. Since the work functions are equal, their vacuum levels will line up as well, and their bands in both the silicon and the oxide are flat, as shown in Fig. 42(a). This is called the flat-band condition. There is no charge, no field and the carrier concentration is at equilibrium value throughout the silicon. When a negative voltage is applied to the gate of a p-type MOS capacitor, as in Fig. 42(b), the metal Fermi level raises (i.e. electron energy) with respect to the Si Fermi level, and creates an electric field in the oxide that accelerates a negative charge toward the Si substrate. A field is induced at the Si surface (surface potential) in the same direction as the oxide field. Due to the lower carrier concentration in Si as compared to the metal, the bands bend upward toward the oxide interface. The Fermi level within the Si is flat since there is no net flow of conduction current. Due to the band bending, the Fermi level at the surface is much closer to the valence band than is the Fermi level in the bulk Si. This results in a hole concentration much higher at the surface than the equilibrium hole concentration in the bulk. Excess holes are accumulated at the surface. This condition is called accumulation ($p > N_A$).

Depletion and Inversion

If positive voltage is applied to the gate of a p-type MOS capacitor, the metal Fermi level moves downward, which creates an oxide field in the direction of accelerating a negative charge toward the metal electrode. A similar field is induced in the Si, which causes the bands to bend downward toward the surface as shown in Fig. 42(c). Since the valence band at the surface is now farther away from the Fermi level than is the valence band in the bulk, the hole concentration at the surface is lower than the concentration in the bulk. This is referred to as the depletion condition. The depletion of holes at the surface leaves the region with a net negative charge arising from the unbalanced acceptor ions. An equal amount of positive charge appears in the metal side of capacitor.

As the gate voltage is increased positively the band bending also increases, resulting in a wider depletion region and more negative depletion charge. This goes on until the bands bend downward so much that the intrinsic potential, near the midgap, at the surface becomes lower than the Fermi potential, as shown in Fig. 42(d). All the holes are now depleted from the surface, and the surface

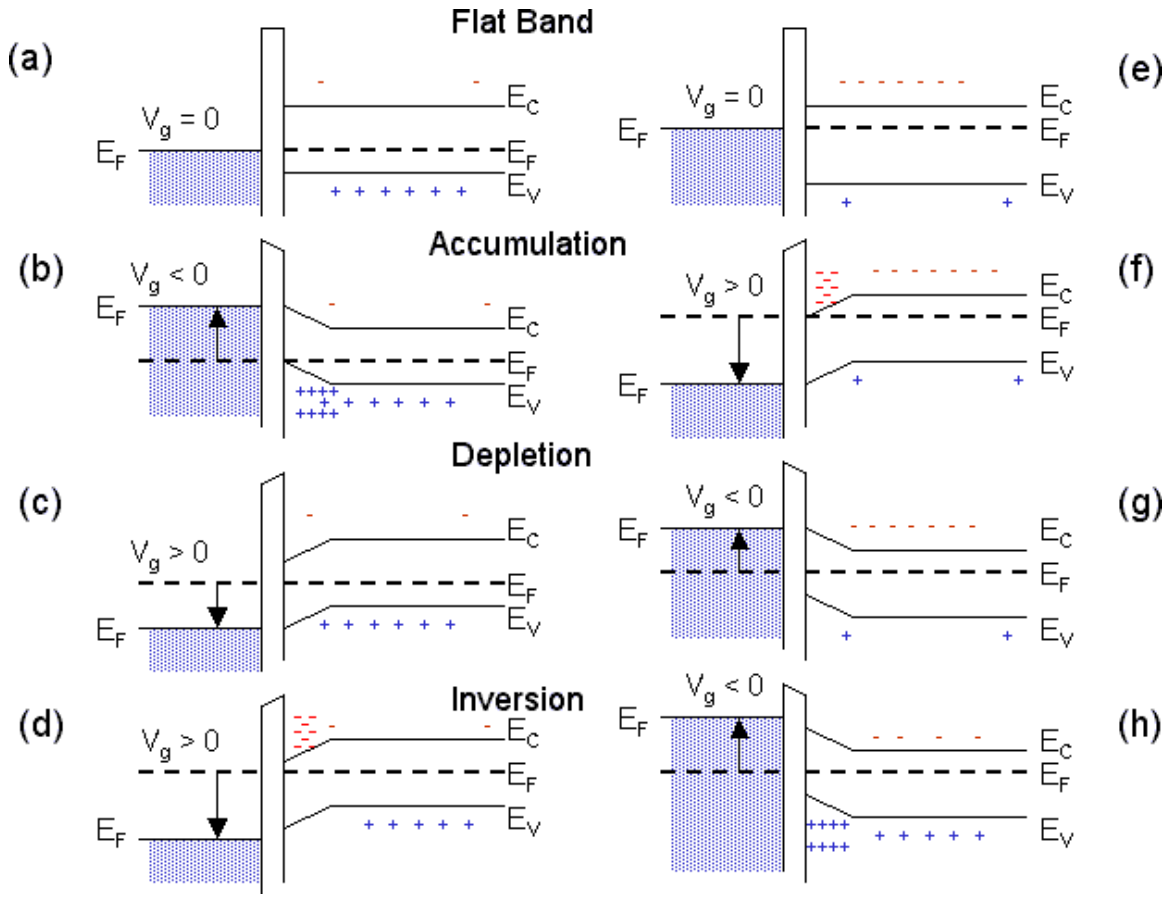

Figure 42: Energy-band diagrams for ideal p-type, (a) - (d), and n-type, (e) - (h), MOS capacitors under different bias conditions: flatband [(a), (e)], accumulation [(b), (f)], depletion [(c), (g)], and inversion [(d), (h)].

potential is such that it is energetically favorable for electrons to populate the conduction band. The surface behaves like an n-type material with an electron concentration given by:

$$n = n_i \exp\left(\frac{E_F - E_i}{kT}\right) \tag{95}$$

This condition is called inversion. The negative charge in the Si consists of both ionized acceptors, and the thermally generated electrons in the conduction band. It is balanced by an equal amount of positive charge in the metal gate. The surface is inverted as soon as $E_i = \frac{E_C + E_V}{2}$ crosses E_F. This is called the weak inversion because the electron concentration remains small until E_i is considerably below E_F. If the gate voltage is increased further, the concentration of electron at the surface will be equal to, and then exceed the hole concentration in the substrate. This condition is known as strong inversion ($\phi_s > 2\phi_B$).

MOS Capacitor

The total capacitance of the MOS structure with no interface traps, oxide charge, or work function difference (ideal MOS) is the series combination of the silicon differential capacitance per unit area, C_{Si}, and the oxide capacitance C_{ox} (Fig. 43).

Low Frequency C-V Characteristics

At low frequencies the MOS structure is in thermal equilibrium under small signal AC excitation, provided that minority carriers can respond to variations in the ac field to prevent energy loss.

Accumulation

Starting with negative bias (V_G negative), the first region of the C-V curve is called accumulation. The bands bend up; a large surface potential exists; the large hole charge density at the silicon surface will contribute a large differential capacitance, i.e. $C_{Si} \gg C_{ox}$ which implies that:

$$C \approx C_{ox} = \frac{\varepsilon_{ox}}{t_{ox}} \tag{96}$$

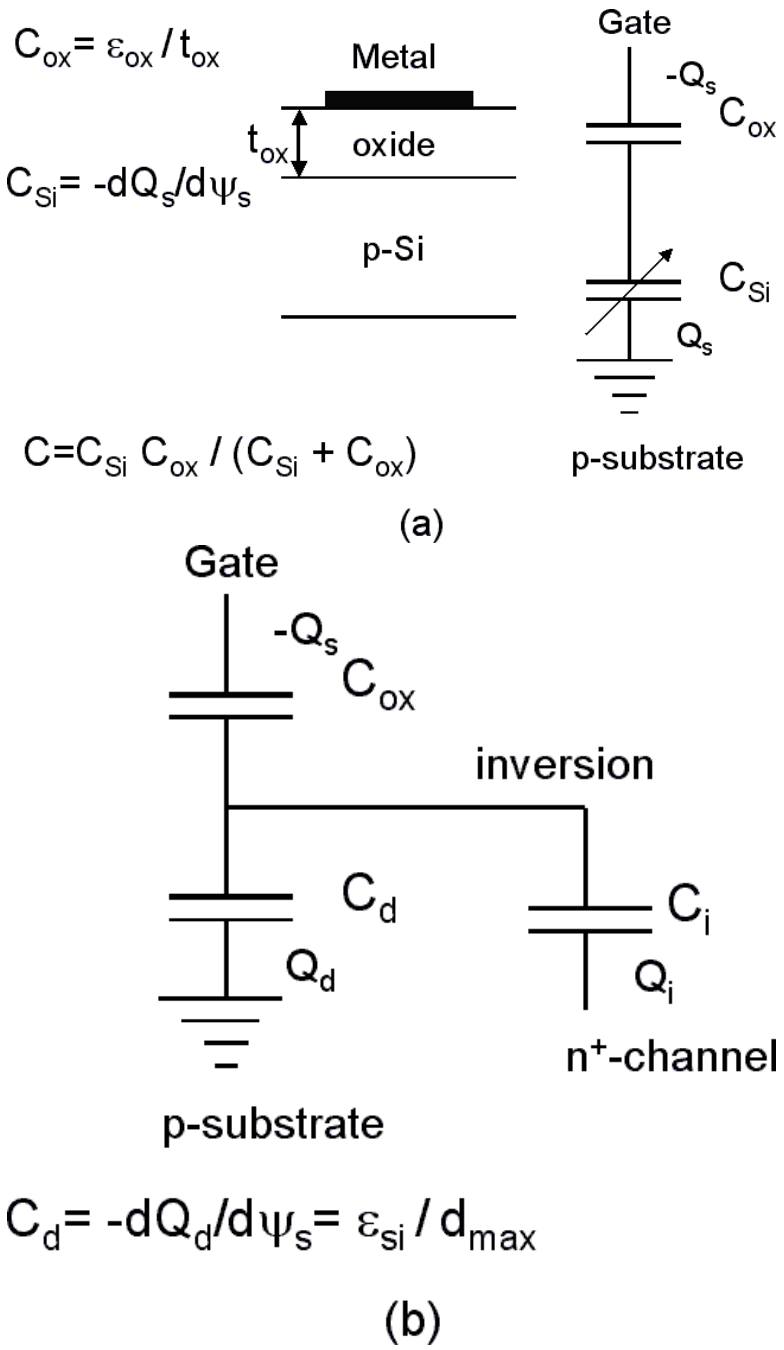

Figure 43: Equivalent circuits of MOS capacitor. (a) All the silicon capacitances are lumped in C_{Si}. (b) C_{Si} is broken up into a depletion capacitance C_d, and an inversion layer capacitance C_i. C_d arises from the majority carriers, which can respond to high frequency as well as low frequency signals. C_i arises from the majority carriers which can only respond to low frequency signals.

Flatband

As gate bias is made less negative, surface hole density will decrease, making C_{Si} smaller. As a result, C becomes less than C_{ox}. When gate bias decreases to zero, we are at flatbands for the ideal MOS situation. Here we need to take the oxide and the silicon capacitance into account. The total capacitance, C, will be lower than for accumulation.

Depletion

As gate bias is made more positive, holes are repelled from the silicon surface, resulting in the formation of a depletion layer of ionized acceptors. The bands bend down. As gate bias is made increasingly more positive, the depletion layer widens, making C_{Si} smaller. Therefore, C becomes smaller.

Inversion

As gate bias is made more positive, surface hole density decreases, whereas surface electron density increases ($p_s n_s = n_i^2$). Eventually an inversion layer of electrons is formed. When the surface band bending, $\phi_S \geq 2\phi_B$, (the bulk potential), then $n_S \geq N_A$ and the differential capacitance of the inversion layer becomes comparable to, and then exceeds C_{ox}, i.e. $C_{Si} \gg C_{ox}$, and C approaches C_{ox} asymptotically.

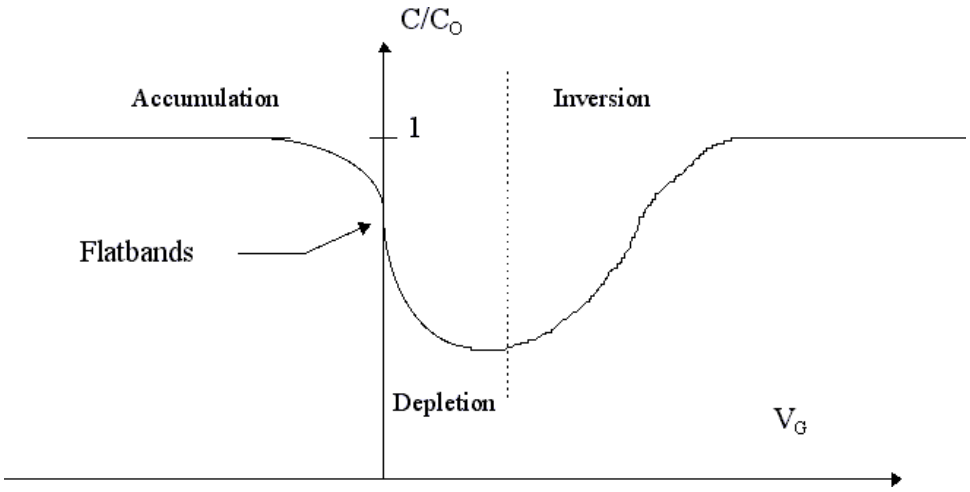

Figure 44: Low frequency CV curve for ideal MOS capacitor.

Frequency Effects

The increase in capacitance in inversion only occurs if the Generation/Recombination (G/R) of electrons can keep up with the applied ac signal. Capacitance meters generally employ a small ac signal, superimposed upon the dc gate bias to measure the MOS capacitance. In practice, G/R rates are relatively slow, so that the capacitance does not increase above a frequency of about 100Hz for the Si-SiO_2 system.

In the presence of some additional reservoir of electrons, the low frequency behaviour may be extended up to the MHz range. This is the case for a MOSFET, where the reservoir is the source and drain n+ regions.

If both the gate bias V_G and the small signal measuring voltage vary at a faster rate than may be allowed by G/R at the surface, then no inversion layer forms, and the MOS device goes into deep depletion. In order to equate metal surface charge, the depletion region must widen to expose more ionized acceptors. Thus the capacitance, C, decreases even further. The depletion region width, d, is now larger than d_{max}, the depletion width saturation value.

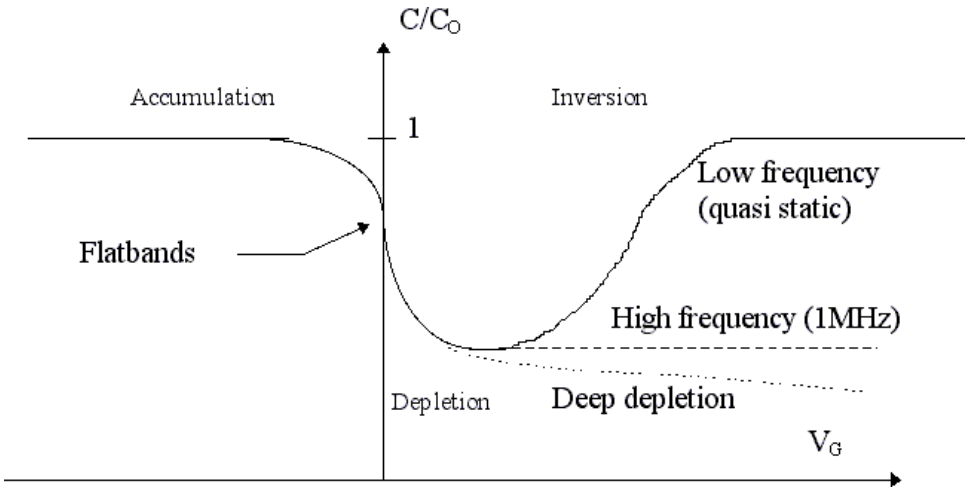

Figure 45: Frequency effects on CV profile for MOS capacitor.

Analysis of MOS Capacitor

The analysis is similar to that of a one-sided n^+p junction. We solve Poisson's equation in the p region.

$$\frac{d^2\Phi}{dx^2} = -\frac{\rho_s(x)}{\varepsilon_{Si}} \tag{97}$$

For depletion $\rho_s = -qN_A$.

Integrating Poisson's equation twice, and imposing appropriate boundary conditions gives:

$$\Phi = \Phi_S \left[1 - \frac{x}{d_{\max}}\right]^2 \tag{98}$$

where,

$$\Phi_S = \frac{qN_A d_{\max}^2}{2\varepsilon_{Si}} \tag{99}$$

For effective inversion the criterion is $n_S = N_A$ or

$$\Phi_S = 2\Phi_B \tag{100}$$

$$= 2\frac{kT}{q}\ln\frac{N_A}{n_i} \tag{101}$$

The depletion region width saturates, i.e. reaches a maximum, at effective inversion (low frequency).

$$d_{\max} = \sqrt{\frac{2\varepsilon_{Si}2\Phi_S}{qN_A}} \tag{102}$$

$$= \sqrt{\frac{2\varepsilon_{Si}2\Phi_S}{qN_A}} \tag{103}$$

$$= \sqrt{\frac{4\varepsilon_{Si}kT\ln\frac{N_A}{n_i}}{q^2N_A}} \tag{104}$$

i.e. $d_{\max} < 1/N_A$

The total depletion charge density in the silicon is equal to the charge per unit area of ionized acceptors in the depletion region, given by:

$$Q_d = -qN_A d_{\max} \approx -\sqrt{2q\varepsilon_{Si}N_A(2\Phi_B)} \tag{105}$$

Capacitance

Recalling that:

$$C = \frac{C_S C_O}{C_S + C_O} \tag{106}$$

$$C_{ox} = \frac{\varepsilon_{ox}}{t_{ox}} \tag{107}$$

$$C_{Si} = \frac{\varepsilon_{Si}}{d_{\max}} \tag{108}$$

$$\frac{C}{C_{ox}} = \frac{1}{\sqrt{1 + \frac{2\varepsilon_{ox} V}{q N_A \varepsilon_{Si} d_0^2}}} \tag{109}$$

For depletion V_G is positive. Increasing the gate voltage will result in a decreasing C.

For accumulation, V_G is negative and there is no depletion layer.

$$C = C_{ox} = \frac{\varepsilon_{ox}}{t_{ox}} \tag{110}$$

For inversion the capacitance is at a minimum.

$$C_{\min} = \frac{\varepsilon_{ox}}{t_{ox} + \frac{\varepsilon_{ox}}{\varepsilon_{Si}} d_{\max}} \tag{111}$$

Carrier Densities as functions of Φ

$$n_p = n_i \exp \frac{q(\Phi - \Phi_B)}{kT} \tag{112}$$

$$p_p = n_i \exp \frac{q(\Phi_B - \Phi)}{kT} \tag{113}$$

$$\tag{114}$$

The surface densities are:

$$n_s = n_i \exp \frac{q(\Phi - \Phi_B)}{kT} \tag{115}$$

$$p_s = n_i \exp \frac{q(\Phi_B - \Phi)}{kT} \tag{116}$$

$$\tag{117}$$

Surface Charge	Surface Charge Density
Accumulation	$p_s > N_A$
Neutral	$p_s = N_A$
Depletion	$n_i < p_s < N_A$
Intrinsic	$p_s = n_s = n_i$
Weak Inversion	$n_i < n_s < N_A$
Strong Inversion	$n_s > N_A$

Gate Voltage

In an ideal MOS structure (Fig. 46) with the absence of a work function difference, a voltage V_G applied to the MOS gate part of it appears as a potential drop V_{ox} across the oxide, and the rest appears as band bending, ϕ_S, in the silicon. V_G is expressed as:

$$V_G = V_{ox} + \phi_S = -\frac{Q_S}{C_{ox}} + \phi_S \tag{118}$$

where ϕ_S is the total charge per unit area induced in the silicon, and C_{ox} is oxide capacitance per unit area.

$$\phi_S = \phi_{S,\text{inv}} = 2\Phi_B \tag{119}$$

When the voltage is such as to make , it is known as the threshold voltage:

$$V_T = V_{ox} + 2\Phi_B \tag{120}$$

$$V_T = \frac{Q_S}{C_{ox}} + 2\Phi_B \tag{121}$$

$$= \frac{qN_A d_{\max}}{C_{ox}} + 2\Phi_B \tag{122}$$

$$= \frac{\sqrt{2\varepsilon_{Si} q N_A 2\Phi_B}}{C_{ox}} + 2\Phi_B \tag{123}$$

Real MOS Structures

The work function difference affects the flat-band voltage, V_{FB}, and the threshold voltage, V_T, of MOS capacitor as follows:

A) The work function difference:

- ϕ_m = metal work function; ϕ_s = silicon work function.
- $\phi_{ms} = \phi_m - \phi_s$

B) The Flat Band voltage

- Q_{ox} = charge per unit area in oxide near the oxide-silicon interface; C_{ox} = oxide capacitance per unit area.
- $V_{FB} = \phi_{ms} - Q_{ox}/C_{ox}$

C) The Threshold voltage

- $\phi_{Si} = 2\Phi_B = 2(kT/q)\ln(N/n_i)$ = the silicon surface potential at strong inversion conditions; and $Q_B = -qNx_{dm}$ = depletion charge in silicon bulk under the gate (+ for p-type, - for n-type Si).
- $V_T = V_{FB} + \psi_{Si} - Q_B/C_{ox}$

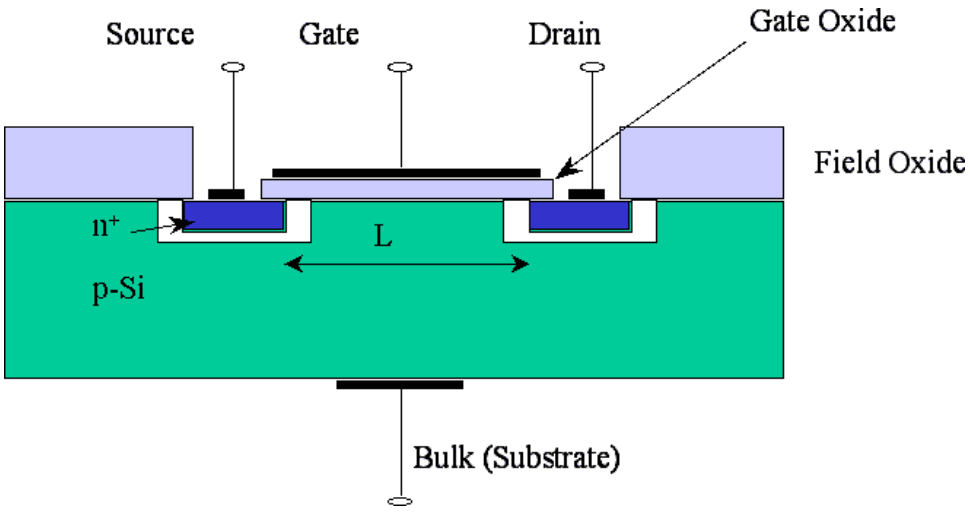

Figure 46: Basic MOS structure.

MOSFET Model

To arrive at an analytical solution for MOS current, use the charge sheet approximation in which the inversion layer thickness is treated as a sheet of zero thickness[108]. This approximation assumes that all inversion charges are located at the surface like a sheet of charge with no potential drop or band bending across the inversion sheet. This charge sheet approximation also incorporates the depletion region, and at the onset of inversion the surface potential is pinned at:

$$\phi_S = 2\phi_B + V(y) \tag{124}$$

This surface potential uses an approximation in that the variation of the electric field along the channel, the y-direction, is much less than the variation perpendicular to the channel, the x-direction (Pao and Sah 1966).

The bulk depletion charge is:

$$Q_d = -qN_A d_{\max} = -\sqrt{2\varepsilon_{Si} qN_A (2\phi_B + V(y))} \tag{125}$$

The total charge density in the Si is given by:

$$Q_S = -C_{ox}(V_G - V_{FB} - \phi_S) \tag{126}$$

$$= -C_{ox}(V_G - V_{FB} - 2\phi_B - V(y)) \tag{127}$$

Differencing Eq. (125) and (126) gives the inversion charge density as:

$$Q_i = Q_S - Q_d \tag{128}$$

$$= -C_{ox}(V_G - V_{FB} - 2\phi_B - V(y)) + \sqrt{2\varepsilon_{Si} qN_A (2\phi_B + V(y))} \tag{129}$$

The current flowing from drain-to-source along the channel with Q_i inversion charge density is:

$$I_{DS}(y) = -\mu_{\text{eff}} W \frac{dV}{dy} Q_i(V) \tag{130}$$

If the current is independent of y, the drain to source current is:

$$I_{DS} = \mu_{\text{eff}} \frac{W}{L} \int_0^{V_{DS}} (-Q_i(V) dV) \tag{131}$$

Substituting in Eq. (131) for Q_i:

$$I_{DS} = \mu_{\text{eff}} C_{ox} \frac{W}{L} \left[\left(V_G - V_{FB} - 2\phi_B - \frac{V_{DS}}{2} \right) V_{DS} - \frac{2\sqrt{2\varepsilon_{Si} q N_A}}{3C_{ox}} \left\{ (2\phi_B + V_{DS})^{\frac{3}{2}} - (2\phi_B)^{\frac{3}{2}} \right\} \right] \tag{132}$$

Remembering that the threshold voltage, V_T, is given by:

$$V_T = V_{FB} + 2\phi_B + \frac{\sqrt{4\varepsilon_{Si} q N_A \phi_B}}{C_{ox}} \tag{133}$$

One look at regions of operation of the MOS transistor, subthreshold, saturation, linear (triode), and pinch-off. In the linear region of operation, V_{DS} is small and Eq. (132) uses a power series expansion of V_{DS}, keeping only the first term of the expansion giving:

$$I_{DS} = \mu_{\text{eff}} C_{ox} \frac{W}{L} (V_G - V_T) V_{DS} \tag{134}$$

For large values of V_{DS} the second terms in the series are incorporated and I_{DS} is expressed as:

$$I_{DS} = \mu_{\text{eff}} C_{ox} \frac{W}{L} \left[(V_G - V_T) V_{DS} - \frac{m}{2} V_{DS}^2 \right] \tag{135}$$

where,

$$m = 1 + \frac{\sqrt{\frac{\varepsilon_{Si} q N_A}{4\phi_B}}}{C_{ox}} = 1 + \frac{C_{Si}}{C_{ox}} = 1 + \frac{3t_{ox}}{d_{\max}} \tag{136}$$

The term M is related to the body effect and is called the body-effect coefficient. This coefficient accounts for the changing substrate bias (V_{BS}). The threshold voltage V_T can be expressed as:

$$V_T = V_{FB} + (2m - 1)(2\phi_B) \tag{137}$$

As V_{DS} increases I_{DS} follows a parabolic curve until a maximum value is reached. This occurs when $V_{DS} = V_{d,\text{sat}} = (V_G - V_T)/m$, giving:

$$I_{D,\text{sat}} = \mu_{\text{eff}} C_{ox} \frac{W}{L} \frac{(V_G - V_T)^2}{2m} \tag{138}$$

The saturation of the drain current, I_{DS}, can be examined using the inversion charge density, Q_i. For $V \leq 2\phi_B$ once can use a power series on V and keep only the two lowest terms and $Q_i(V)$ becomes:

$$Q_i(V) = -C_{ox}(V_G - V_T - mV) \tag{139}$$

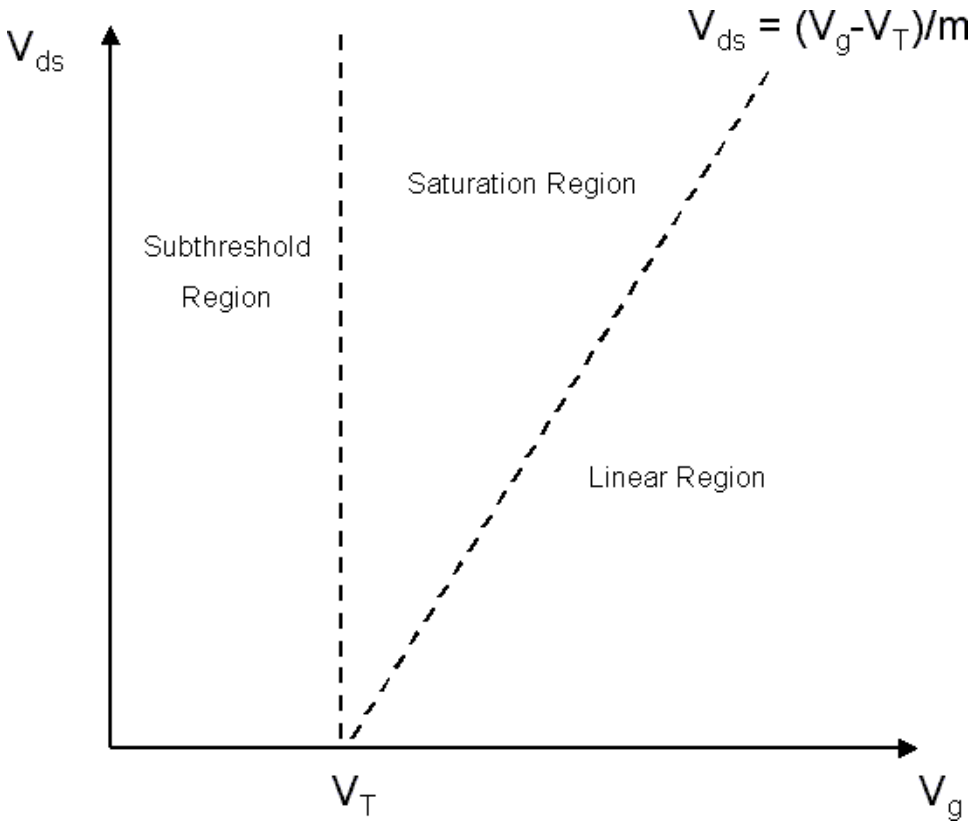

Figure 47: Three regions of MOSFET operation in the V_{DS}-V_G plane.

Plotting $Q_i(V)$, as in Fig. 48, shows that the drain current is proportional to the area under the $-Q_i(V)$ curve between V=0 and V_{GS}. When V_{DS} is small (linear region), the inversion charge density at the drain end of the channel is only slightly lower than at the source end. As the drain voltage increases, for a given V_G, the current increases, but the inversion charge density at the drain decreases until it goes to zero when $V_{DS} = V_{D,\text{sat}} = (V_G - V_T)/m$. The surface channel vanishes at the drain end of the channel when saturation occurs, called pinch-off. When V_{DS} increases beyond saturation, the pinch-off moves toward the source, with the drain current remaining essentially constant.

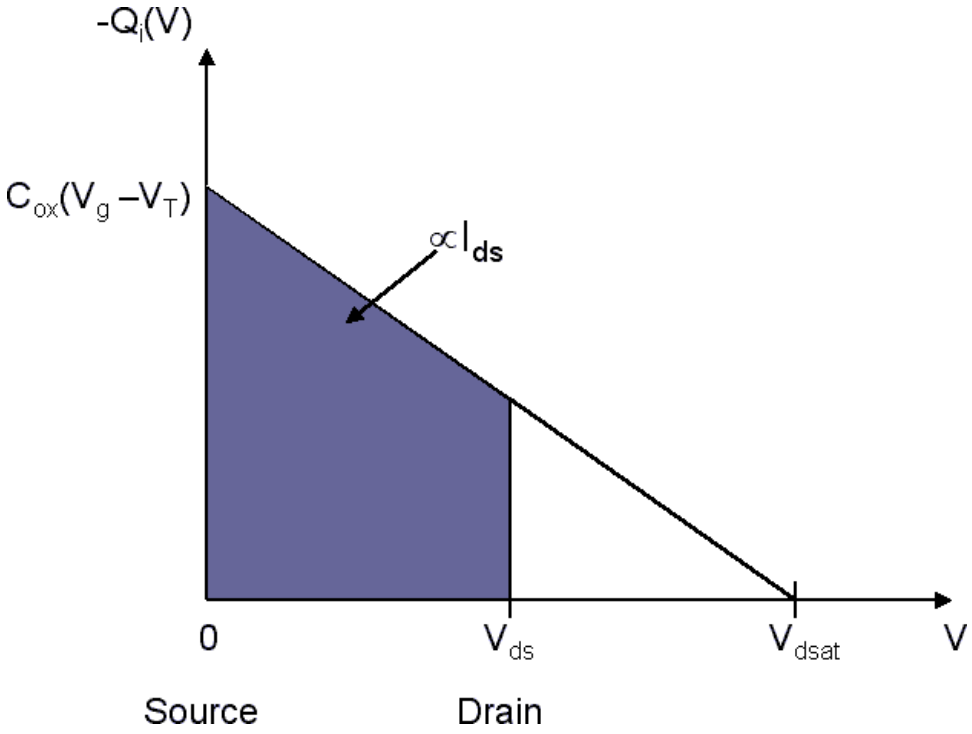

Figure 48: Inversion charge density as a function of the quasi-Fermi potential of a point in the channel. Before saturation, the drain current is proportional to the shaded area integrated from zero to the drain voltage.

Beyond pinch-off carriers are no longer confined to a surface channel, and a 2-D Poisson's equation must be solved for carrier injection into the region between pinch-off and drain depletion region. If one substitutes:

$$V_{DS} = V_G - V_{FB} - 2\phi_B + \frac{\varepsilon_{Si} q N_A}{C_{ox}^2} - \sqrt{\frac{2\varepsilon_{Si} q N_A}{C_{ox}^2}\left(V_G - V_{FB} + \frac{\varepsilon_{Si} q N_A}{2C_{ox}^2}\right)} \tag{140}$$

into Eq. (135)[109] I_{DS} is approximated beyond pinch-off.

One characterization region yet to be examined is subthreshold region where $V_G < V_T$. Here conduction is dominated by diffusion current. The charge density in Si is:

$$-Q_S = \varepsilon_{Si} E_{Si} = \sqrt{2\varepsilon_{Si} kT N_A}\left[\frac{q\phi_S}{kT} + \frac{n_i^2}{N_A^2}\exp\left(\frac{q(\phi_S - V)}{kT}\right)\right]^{\frac{1}{2}} \tag{141}$$

In weak inversion,

$$\frac{n_i^2}{N_A^2}\exp\left(\frac{q(\phi_S - V)}{kT}\right) \tag{142}$$

is much less than

$$\frac{q\phi_S}{kT} \tag{143}$$

Expanding $-Q_S$ into a power series the zeroth-order is the depletion charge density $-Q_d$ and the first order term gives the inversion charge density:

$$-Q_i = \sqrt{\frac{\varepsilon_{Si} q N_A}{2\phi_S}} \left(\frac{kT}{q}\right) \left(\frac{n_i}{N_A}\right)^2 \exp\left(\frac{q(\phi_S - V)}{kT}\right) \tag{144}$$

This implies that I_{DS} in the subthreshold region is:

$$I_{DS} = \mu_{eff} \frac{W}{L} \sqrt{\frac{\varepsilon_{Si} q N_A}{2\phi_S}} \left(\frac{kT}{2}\right)^2 \left(\frac{n_i}{N_A}\right)^2 \exp\left(\frac{q\phi_S}{kT}\right) \left[1 - \exp\left(-\frac{qV_{DS}}{kT}\right)\right] \tag{145}$$

To further simplify I_{DS} one can use:

$$\phi_S = 2\phi_B \tag{146}$$

which states that:

$$V_G = V_{FB} + 2\phi_B + \frac{\sqrt{4\varepsilon_{Si} q N_A \phi_B}}{C_{ox}} + \left(1 + \frac{\sqrt{\frac{\varepsilon_{Si} q N_A}{4\phi_B}}}{C_{ox}}\right)(\phi_S - 2\phi_B) \tag{147}$$

$$V_G = V_T - M(\phi_S - 2\phi_B) \tag{148}$$

This then allows one to solve for:

$$\phi_S = -\frac{V_G - V_T - 2m\phi_B}{m} = \frac{V_T + 2m\phi_B - V_G}{m} \tag{149}$$

The subthreshold current is rewritten to be:

$$I_{DS} = \mu_{\text{eff}} C_{ox} \frac{W}{L} (m-1) \left(\frac{kT}{q}\right)^2 \exp\left(q(V_G - V_T) mkT\right) \left[1 - \exp\left(-\frac{qV_{DS}}{kT}\right)\right] \tag{150}$$

Fig. 49 provides a view of the I_{DS}-V_{DS} characteristics of an NMOS device for various values of V_G.

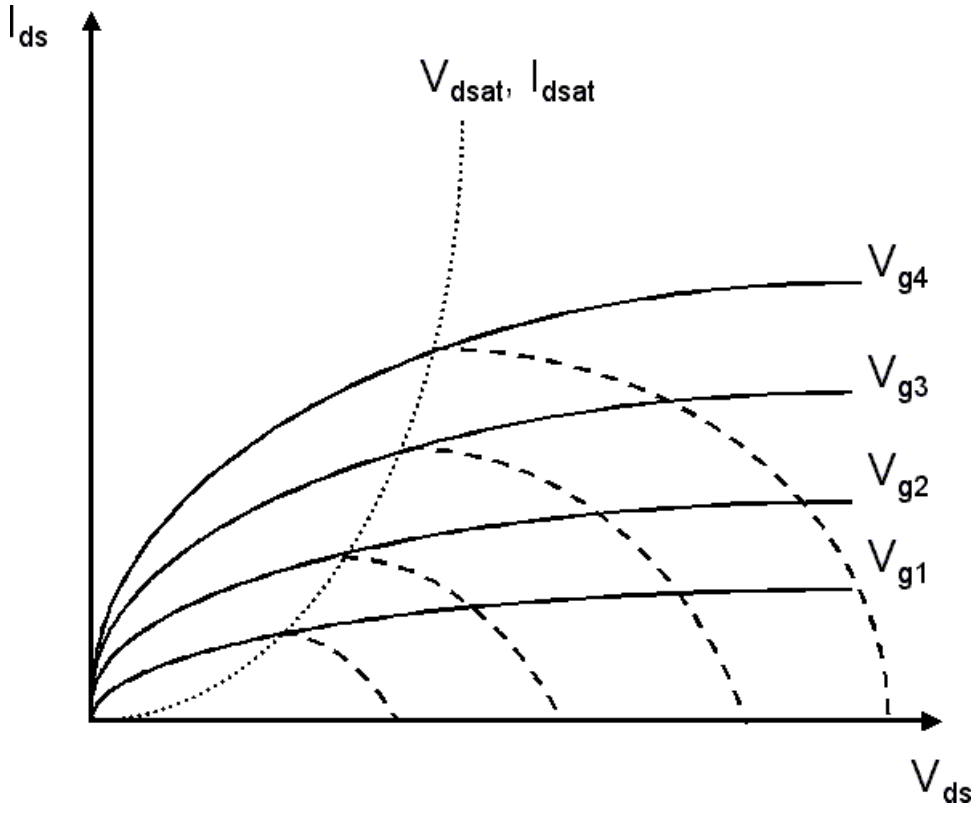

Figure 49: Long channel MOSFET I_{DS}-V_{DS} characteristics (solid curves) for several different values of V_G. The dotted curve shows the trajectory of drain voltage beyond which the current saturates. The dashed curves show the parabolic behavior of the characteristics before saturation.

Appendix C

SOI MOS TECHNOLOGY

SOI MOS technology starts with manufacturing wafers containing a thin silicon layer above a relatively thick layer of silicon oxide. There are several approaches to manufacturing SOI substrates, and their major features are briefly described below [1,3,4]. Separation by implantation of oxygen (SIMOX) injects a high concentration of oxygen beneath the surface of a silicon wafer, typically using a dose of 2×10^{18} atoms/cm^2 at 200 keV. The implantation receives a high-temperature anneal to restore crystalline quality of the silicon layer over the buried oxide (BOX), which forms during the same heat treatment.

A latest trend with SIMOX fabrication is to use a lower oxygen implant dose to obtain an improved, low-cost SOI material. This new approach has drastically improved the top silicon film crystalline quality, but also yields much thinner silicon and SiO_2 layers. For example, the internal thermal (ITOX) SIMOX process uses a high-energy, smaller-dose oxygen implant to produce a thick silicon layer and a thin BOX layer ($\sim$300 nm and 80 nm respectively). A subsequent anneal in oxygen oxidizes some of the superficial silicon layer, and increases the thickness of the BOX.

Separation by plasma implantation of oxygen (SPIMOX) is another potentially low-cost process for fabricating SOI substrates. In this modification of SIMOX process, oxygen is implanted by plasma immersion. The whole wafer is implanted at once, resulting in a much high wafer throughput. A potential drawback of this technique is the lack of ion beam selection and possible contamination.

Bond and etch-back SOI (BESOI) is used to manufacture relatively thick films of both oxide and silicon. Two silicon wafers, one with an oxide layer, are bonded together using Van der Waals forces. A subsequent anneal increases the bonding strength. Finally, one side of the bonded substrate is thinned to roughly 1m by mechanical grinding and polishing. Typically, the bonded wafers have thicker, yet better-quality, silicon and buried oxide layers compared to the SIMOX process. Analog Devices widely uses a high-speed complementary bipolar process called XFCB (eXtra-Fast Complementary Bipolar), which is a variation of the BESOI technology for production of commercial mixed-signal microcircuits.

Smart Cut Technology combines ion implantation and wafer-bonding technologies. A wafer is oxidized to form the buried oxide layer of the SOI structure. A high-dose (5×10^{16} ions/cm^2) hydrogen ion implantation through the oxide forms cavities or micro=bubbles at the implantation range. This wafer is then bonded to another wafer using Van der Waals forces. A 500°C thermal activation nucleates, coercing hydrogen into the cavities and merging them, causing delamination of the top section of the wafer. The use of ion implantation for the layer separation improves the layer thickness uniformity.

Epitaxial layer transfer (ELTRAN) produces SOI wafers with a relatively defect-free silicon film. It is formed by growing an epitaxial layer on a layer of porous silicon. This wafer is then bonded to a "handle" wafer and is either ground down, or separated at the porous layer. SIMOX is considered to be the most promising among the various SOI technologies. In spite of a seemingly destructive process, the SIMOX does result in stress-free silicon film, which enables manufacturing device-grade SOI structures. The thin silicon layer formed by this technology is a wafer-scale monocrystal with high quality and excellent electrical properties[110].

In a regular-quality SIMOX wafer, the buried oxide interfaces are sharp and uniform. However, physical properties of the buried oxides are different compared to the thermal oxide. The buried oxide is silicon-rich, which results in a high density of electron traps (strained Si-Si bonds) and E′-centers (acting as traps for holes). The breakdown electrical field in good-quality BOX exceeds 8 MV/cm, which is still below the values typical for thermal oxides (in the range of 10 to 16 MV/cm).

SOI Lateral Isolation

Traditionally, lateral isolation between SOI devices is obtained by the formation of a mesa structure, or by producing a thick field oxide using LOCOS (local oxidation of silicon) process.

In mesa isolation, the active device regions are masked to etch the field device areas (see Fig. 50. The SOI oxide helps as the etch-stop layer, while anisotropic etching allows for an efficient isolation scaling. The weak point of this isolation technique is the sharpness of the sidewall, and its potential impact on gate oxide integrity and the device subthreshold characteristics[110]. Special care should be taken to prevent the possibility of etching through a thin BOX (in some cases 100 nm) when a mesa isolation with an Si-island sidewall spacer is formed.

LOCOS isolation in SOI is much the same as the LOCOS in bulk silicon. However, the oxida-

tion kinetics in SOI is somewhat different, particularly when the growing oxide reaches the buried oxide. The oxidation time to consume the entire silicon film can be long, resulting in transistor-width loss. It is also possible that LOCOS isolation may introduce mechanical stresses in the active region of the MOSFET, causing device leakage.

Most manufacturers of the SOI devices use the trench isolation process (or shallow trench isolation, STI) as a prime choice for lateral isolation. Shallow trench isolation needs to be modified compared to conventional bulk-Si process for shallower, selective to oxide etch, thinner deposited oxide and shorter chemical-mechanical polishing (CMP) cycles.

SOI Defects and Issues

The dominant defects detected in the SIMOX are threading dislocations, small stacking faults (which are frequently observed at the bottom of the Si overlay) and the BOX defects, which can lead to leakage currents[111, 110].

These BOX defects are typically silicon inclusions, bridging defects (or “pipes”) and interface undulations in the SIMOX material. Two factors contribute to these defects: (1) the presence of particles on the wafer surface, locally masking oxygen ion implant, and (2) local kinetics of BOX formation during the implantation and annealing process. Crystalline silicon inclusions and islands are often encountered at the bottom of the oxide, reducing its effective thickness and hardness.

A thin SOI film has several characteristic defects: stacking faults, inclusions, and threading dislocations. The dislocations are not known to pose a performance or reliability risk in CMOS devices on SOI. The stacking faults are usually small, comparable to those found below the BOX, and located near the SOI/BOX interface. They are unlikely to have serious impact on the devices; however, they have been found to contribute to the transistor leakage when their size encroaches on the junction area. The inclusions, manifesting themselves as, so-called HF defects, when their size spans the full thickness of the SOI film, are considered killer defects when located under the gate area. Their origin is related to large oxygen precipitates, or BOX “upwelling” to the top of the wafer. These defects could be caused by particles locally masking oxygen implant, or heavy precipitation of metal contamination during high temperature processing that forms the HF-soluble silicides.

Dopant diffusion in thin SOI film can be different than in the bulk-Si process. This factor, as well as some implant dose loss into the BOX for very thin SOI films, and dopant segregation into

the buried oxide may require modification of the implantation regimes and the thermal processes.

Silicidation of very thin SOI film (typical for fully depleted SOI technology) with large amounts of refractive metal may lead to over-consumption of silicon, and form voids at the source/drain and channel boundary, which may also result in the formation of silicide under the gate area. Therefore, extreme precautions have to be taken during the front-end processing because of the limited amount of silicon on the top surface of an SOI substrate. This thin silicon layer can be easily removed by extensive wet or dry etches, or oxidation.

SOI MOSFET Transistors

The major difference between a bulk-Si MOS transistor, and a SOI MOS transistor from the circuit designer point of view, is that the later has smaller junction capacitance and has a floating body[110].

SOI MOS device physics are dependent on the thickness of the silicon on which they are produced. Devices are classified as thick, thin and medium film. Medium film thickness devices exhibit a thick on thin film behavior, depending on the back gate thickness. This SOI MOS device classification depends on the depletion zone width. In thick-film SOI devices, the silicon film is greater than twice the value of dmax. This thickness in tsi does not support interaction between the front and back depletion zones. The area of neutral silicon between the two depletion zones is called the body.

Thick film devices are also known as Partially Depleted (PD) devices. The characteristics of PD devices are similar to bulk devices if the body is connected to ground. Leaving the body floating the PD device will exhibit two parasitic effects: kink and open bipolar transistor between source and drain.

The thin film SOI device has a silicon film thickness less than dmax. In this device the silicon film is fully depleted at threshold. Back-gate bias conditions will change this fully depleted state for very large voltages only. Thin-film SOI devices are also known as fully depleted (FD) SOI devices.

Medium-thickness SOI devices are obtained when the silicon film thickness is between dmax and 2X dmax. The behavior of medium thickness SOI devices is dependent on front and back-depletion zones. If these depletion zones touch, overlapping depletion zones support behaviors similar to FD devices, while non touching depletion zones produce behaviors similar to PD devices.

A summary of SOI device performance behaviors referenced to bulk CMOS is given in Table 8.

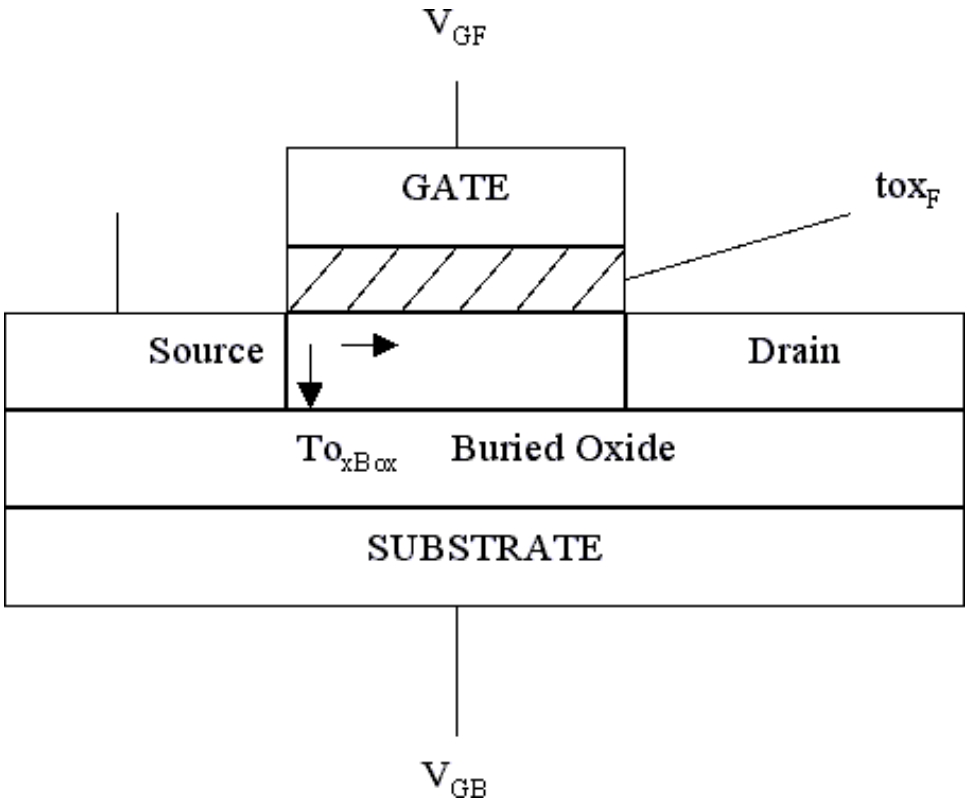

Figure 50: Basic SOI MOS structure.

These are some other effects and characteristics associated with SOI MOS devices are:

Floating-Body Effects Floating Body Effect (FBE) is the major parasitic effect in SOI-MOSFETs and is a consequence of the complete isolation of the transistor from the substrate. The effect is related to the built-up of a positive charge in the silicon body of the transistor, originating from the holes created by impact ionization. This charge can not be removed rapidly enough, primarily because no contact with the Si film (body) is available. There are various consequences of this built-up charge, which are generally referred to as the floating-body effects, such as[110]: kink-effect; negative conductance and transconductance; hysteresis and instabilities, single transistor latch (the transistor cannot be turned off by reducing gate voltage), bipolar transistor action, and premature breakdown. The FBE can lead to circuit instabilities, frequency-dependent delay time, and pulse stretching. Many of the negative consequences of the FBE could be eliminated by using a body contact for every MOSFET,

Table 8: Relative performance of PD (Thick-Film) and FD (Thin-Film) SOI MOS Devices compared to Bulk MOS devices.

	PD or Thick Film	FD or Thin Film
Mobility	Same	Better
Source and Drain Capacitance	Better	Better
Transconductance	Same	Better
Short Channel	Same	Same/Better
Subthreshold Slope	Same	Better
$V_T(t_{Si})$	Same	Worse
Kink	Worse	Same
Parasitic Transistor	Worse	Same/Worse
Radiation		
Total Dose	Same/Better	Worse
SEU	Better	Better
Dose Rate	Same	Better

but this is generally not an optimum solution. It should be noted that these typical SOI effects can be observed even in the bulk-Si MOSFETs at low temperatures when the substrate becomes semi-insulating and if the substrate contact is left floating.

Edge Effects - The lateral edges of the SOI MOSFETs represent a parasitic conduction path between the source and the drain. This sidewall transistor operates in parallel with the main transistor, and strong coupling and charge sharing between the front, back, and the edge channels dictate its threshold voltage. Special edgeless devices (e.g. H-gate transistor, which has two p+ body contacts that inhibit any conduction path along the sidewalls may be designed, but this is a space-consuming alternative[110].

Reliability Issues in SOI Technology

Self-Heating Effects

In general, many of the reliability issues related to bulk devices such as dielectric related, conductor and metallization, hot carrier related degradation and failures are applicable to SOI technology, as well. Most new reliability issues in SOI devices, which are not known in the traditional

bulk-Si devices are related to the presence of the buried oxide. In the bulk technologies, heat generated by charge transfer in the transistor is readily transferred out of the chip backside through silicon substrate. This transfer of heat is quick enough so that local device transconductance changes due to self-heating are negligible. For bulk devices with six or more layers of interconnect, the stacked inter-layer dielectrics (ILDs) present substantial thermal resistance. However, in the current generation of submicron technology bulk devices, these thermal issues are being addressed with the use of reduced dielectric constant dielectrics and higher conductivity metallization based on copper interconnect.

In SOI technology, silicon dioxide, comprises the BOX layer, so that the SOI transistor is encased in a perfect little insulated region of its own. As a result, the average junction temperature of SOI devices can be somewhat higher than for an identical bulk device, reducing the device transconductance. Since SOI transistors are thermally insulated from the substrate by the buried insulator, the removal of excess hear generated by the Joule Effect, within the device is less efficient than in the bulk devices. The excess heat has several conduction paths, diffusing vertically through the buried oxide and laterally through the silicon island into the contacts and the metallization.

Thus, SOI MOSFETs are susceptible to the local thermal heating generated in the channel due to less thermal conductivity of the buried oxide, which is approximately 100 times lower than thermal conductivity of silicon[110]. The self-heating causes a reduction of the carrier mobility, shifts the threshold voltage, and results in a negative differential conductance at high gate and drain voltages. The negative resistance, which can be seen in the output characteristics of SOI MOSFETs is due to a mobility reduction effect caused by device self-heating.

This effect can compromise reliability of the part when the part is operating at low and ultra low temperatures due to thermo-mechanical stresses and possible formation of structural defects and microcracks. In SOI devices, self-heating effect can be minimized by using a thin buried oxide film; thus, decreasing the bottom layer thermal resistance. Another advantage of this approach is the reduction of short channel effect for the back transistor. However, the back channel transistor threshold voltage is reduced if the doping level at the back channel interface is not increased. This, in combination with a floating body effect, can lead to a worst case behavior.

The self-heating effect is more pronounced in fully-depleted structures due to thinner silicon films, which means a thinner buried oxide will be required to minimize it. The limitation for thin-

ning the buried oxide is imposed by the variations of the threshold voltage with the backgate bias. Fully depleted devices exhibit a different electrical behavior from the partially depleted devices. The threshold voltage varies with the backgate bias for enhancement mode and accumulation mode devices due to the coupling effect between the front and the back gates when the silicon film is fully depleted. As a result of this coupling effect, the threshold voltage of fully depleted devices becomes a function of the silicon and buried oxide thicknesses.

A summary of SOI device performance behaviors reference to bulk MOS devices is given in Table 8.

Appendix D

PROPERTIES OF INTRINSIC DEFECTS

To form one vacancy at constant pressure, we introduce some free enthalpy G_F, known as Gibbs energy. This G_F is defined as:

$$G_F = H_F - T \cdot S_F \tag{151}$$

The index "F" here means "formation". H_F is the formation enthalpy of one vacancy, S_F the formation enthalpy of one vacancy, and T is the absolute temperature.

The formation entropy is a property of a single vacancy resulting from the disorder introduced into the structure by changing the vibrational properties of the neighboring atoms. S_F should not be confused with the entropy of mixing or configurational entropy. The configurational entropy originates from the many possibilities of arranging vacancies.

In examining oxides used in the semiconductor process there will be the possibility of point defects associated with the structure. In analysis of these oxide structures thermodynamically, one attempts to find the concentration of vacancies in thermal equilibrium from the minimum of G with respect to n (the number of vacancies):

$$\frac{\partial G}{\partial n} = \frac{\partial}{\partial n}(G_0 + G_1 + G_2) = 0 \tag{152}$$

where G_0 is the Gibbs energy of the perfect structure, G_1 is the energy needed to generate n vacancies ($n \cdot G_F$), and $G_2 = -T \cdot S_{\text{conf}}$. S_{conf} is the configurational entropy of n vacancies or the entropy of mixing n vacancies. Thermal equilibrium describes the unique state of an ensemble of particles that the system assumes by itself sooner or later for a given set of intrinsic parameters, (temperature, pressure, chemical potential) and extrinsic parameters (volume, entropy, number of particles).

The partial derivative of G with respect to n, $[\partial G/\partial n]$, is, by definition, the chemical potential, μ, of the defects under consideration. In other words, the "chemical potential" is a measure of how much the free enthalpy, or the free energy, of a system changes if you add or remove a number of

particles of species i while keeping the number of the other particles, the temperature T, and the pressure p constant. Thus, the partial derivative of G with respect to n, $[\partial G/\partial n]$, is:

$$\frac{\partial G_0}{\partial n} = 0 \tag{153}$$

$$\frac{\partial G_1}{\partial n} = G_F \tag{154}$$

This leads to:

$$G_F - T\frac{\partial S_{\text{conf}}}{\partial n} = 0 \tag{155}$$

Calculating the configurational entropy, S_{conf}, using Boltzmann's formula, one arrives at:

$$S = k_B \ln P \tag{156}$$

where, k_B is the Boltzmann's constant and P is the number of different microstate configurations for a given macrostate. Any particular arrangement of atoms or particles where one examines only average quantities is a macrostate, while any individual arrangement defining the properties, like location and momentary velocity, of all the particles for a given macrostate is a microstate. For a microstate, it matters what individual particles do; for the macrostate, it does not. Macrostates are defined by the number n of vacancies, and the number N of atoms in a particular structure. To obtain P(n), look at the number of possibilities to arrange n vacancies on N sites within the structure. This combinatoric expression is:

$$P = \frac{N!}{(N-n)!n!} \tag{157}$$

The entropy of mixing is now:

$$S = k \ln \frac{N!}{n!(N-n)!} \tag{158}$$

$$= k\left[\ln N! - \ln\{n!(N-n)!\}\right] \tag{159}$$

$$= k\left[\ln N! - \ln n! - \ln(N-n)!\right] \tag{160}$$

The free enthalpy for a crystal of N atoms containing n vacancies is:

$$G(n) = nG_F - kT\left[\ln N! - \ln n! - \ln(N-n)!\right] \tag{161}$$

To find the minimum of G(n) by setting $\partial G(n)/\partial n = 0$, it is necessary to differentiate factorials. This is accomplished using Stirling's approximation:

$$\ln x! \approx x \ln x \tag{162}$$

and the physical approximation that there are far fewer vacancies than atoms, $n \ll N$:

$$\frac{n}{N-n} \approx \frac{n}{N} = c_v = \text{Concentration of vacancies} \tag{163}$$

Substituting $\partial S(n)/\partial n$ using the Stirling formula, the following result is obtained:

$$\frac{\partial S_n}{\partial n} = k\frac{\partial}{\partial n}\left(\ln N! - \ln n! - \ln(N-n)!\right) \tag{164}$$

$$\approx k\frac{\partial}{\partial n}\left(N\ln N - n\ln n - (N-n)\ln(N-n)\right) \tag{165}$$

This can be reduced to:

$$\frac{\partial S_n}{\partial n} \approx -k\left(\ln n + 1 - \ln(N-n) - 1\right) \tag{166}$$

$$= -k\left(\ln n - \ln(N-n)\right) \tag{167}$$

$$= -k\ln\frac{n}{N-n} \tag{168}$$

Using the physical approximation one obtains:

$$\frac{\partial S_n}{\partial n} \approx -k\ln c_v \tag{169}$$

Putting this in Eq. (155) one gets:

$$\frac{\partial G(n)}{\partial n} = 0 = G_F - T\frac{\partial S_n}{\partial n} = G_F + kT\ln c_v \tag{170}$$

Solving for c_v, the concentration of vacancies, one obtains the formula:

$$c_v = \exp\left(-\frac{G_F}{kT}\right) \tag{171}$$

or, using $G_F = H_F - TS_F$:

$$c_v = \exp\left(\frac{S_F}{k}\right)\exp\left(-\frac{H_F}{kT}\right) \tag{172}$$

The constant factor $\exp(S_F/k)$ is due to the reference enthalpy G_0 of the defect-free structure not being constant, but dependent on the chemical environment since it is a sum over all chemical potentials of the constituent particles. The concentration of oxygen vacancies on oxide structure may depend on the partial pressure of O_2 in the atmosphere the structure experiences.

In general, an additional factor must be considered. This new factor results in c_v being set to:

$$c_v = D\exp\left(-\frac{G_F}{kT}\right) \tag{173}$$

The energy state of a vacancy might be “degenerate” because it is charged, and has trapped an electron that has a spin which could be either up or down - we have two energetically identical “versions” of the vacancy and D=2 in this case.

The formation entropy, S_F, is associated with a single defect as the additional entropy or disorder added to the structure with every additional vacancy. There is disorder associated with every single vacancy because the vibration spectra of the atoms are disturbed by defects.

Atoms with a vacancy as a neighbor tend to vibrate with lower frequencies because some bonds, acting as “springs”, are missing. These atoms are less well localized than the others. The calculation of the formation entropy is a bit complicated. If the structure is described as a sum of harmonic oscillators and the harmonic approximation from quantum mechanics is used, the energy E for an oscillator number i and the necessary quantum number n is:

$$E_{i,n} = \frac{h\omega_i}{2\pi}\left(n+\frac{1}{2}\right) \tag{174}$$

To derive the entropy it is necessary to use the partition functions of the system. The partition function is a statistical thermodynamic quantity that describes how particles will partition themselves over the possible quantum states. The partition function Z_i of one harmonic oscillator as

defined in statistical mechanics is given by:

$$Z_i = \sum_n \exp\left(-\frac{h\omega_i(n+1/2)}{2\pi kT}\right) \tag{175}$$

The partition function of the structure then is given by the product of all individual partition function of the p = 3N oscillators forming a structure with N atoms, each of which has three degrees of freedom for oscillations. We have:

$$Z = \prod_{i=1}^{p} Z_i \tag{176}$$

From statistical thermodynamics we know that the free energy F (for solids it is a very good approximation for the free enthalpy G) of our oscillator ensemble is given by:

$$F = -kT\ln Z = kT\sum_i \left[\frac{h\omega_i}{4\pi kT} + \ln\left\{1-\exp\left(-\frac{h\omega_i}{2\pi kT}\right)\right\}\right] \tag{177}$$

Likewise, the entropy of the ensemble for constant volume is:

$$S = -\frac{\partial F}{\partial T} \tag{178}$$

Differentiating with respect to T yields for the entropy of our ideal structure without defects:

$$S = k\sum_i \left[-\ln\left(1-\exp\frac{h\omega_i}{2\pi kT}\right) + \frac{\frac{h\omega_i}{2\pi kT}}{\exp\left(\frac{h\omega_i}{2\pi kT}-1\right)}\right] \tag{179}$$

Now consider a structure with just one vacancy. All eigen-frequencies of all oscillators change from ω_i to a new as yet undefined value ω_i'. The entropy of vibration now is S'.

The formation entropy (S_F) of our single vacancy now can be defined as:

$$S_F = S' - S \tag{180}$$

which is the difference in entropy between the defect free structure and a structure with one vacancy.

The Debye temperature (T_{Debye}) is the temperature of a crystal's highest normal mode of vibration, i.e. the highest temperature that can be achieved due to a single normal vibration. The

Debye temperature is given by:

$$T_{\text{Debye}} = \frac{h}{k}\left(\frac{3N}{4\pi V}\right)^{\frac{1}{3}} v_s \tag{181}$$

where h is Planck's constant, k is Boltzmann's constant, (N/V) is the number density of atoms and v_s is the effective speed of sound in the material.

At temperatures higher than T_{Debye},

$$\frac{h\omega_i}{2\pi} \ll kT \tag{182}$$

$$\frac{h\omega_i'}{2\pi} \ll kT \tag{183}$$

which means that one can expand $h\omega_i/2p$ into a series. Considering only the first term and summing over all eigen frequencies of the structure, results in:

$$S_F = k\sum_i \ln\frac{\omega_i}{\omega_i'} \tag{184}$$

For most analytical calculations only next neighbors of a vacancy need be considered as contributors to the sum. This assumes $\omega = \omega'$ everywhere else in the structure.

The formation entropy measures the spatial extension of a vacancy, or, more generally, of a zero-dimensional defect. The larger the S_F, the more extended the defect will be because more atoms must have changed their vibration frequencies. $S_F \approx 1k$ corresponds to a truly atomic defect with $S_F \approx 10k$ corresponding to extended defects disturbing a volume of about 5 - 10 atoms.

This analysis assumes that there is no interaction between point defects, or that their density is so low that they "never" meet. Interactions are the rule, and for vacancies they are usually attractive. A vacancy introduces a disturbance in the otherwise perfectly periodic potential that will be screened by the free electrons, a rearrangement of the electron density around a vacancy. The formation enthalpy of a vacancy is mostly the energy needed for the rearrangement; the elastic energy contained in the somewhat changed atom positions is comparatively small. If one now introduces a second vacancy next to to the first one, part of the screening is already in place; the free enthalpy needed to remove the second atom is smaller.

For covalently bonded structures, the formation energy of a vacancy is mostly determined by the energy needed to "break" the bonds. Taking away a second atom means that fewer bonds

need to be broken. Ionic structures have vacancies that are charged, leading to coulomb attraction between vacancies in the cation or anion sub-lattice, and to repulsion between vacancies of the same nature.

Appendix E

ANALOG BEHAVIORAL USER DEFINED CAPABILITY

As more complex element behaviors are desired, it becomes more difficult to simulate using basic library elements or waiting for user requests to be implemented into the commercial code. One method of simulating complex element behaviors is to create behavioral models using the below developed constructs now available within our Multi-Level framework. Silvaco software supports this capability through specific interfaces.

All behavioral devices calculate output variables as Y=F(X) where,

Y is the output current, voltage, resistance, or capacitance.

X is the controlling current or voltage, and

F is one of the following:

polynomial function

piecewise linear function

an “expression”

a lookup table

Polynomial Function

SmartSpice supports the polynomial controlling function `POLY`. This function is implemented for all four types of dependent sources (`E`, a Voltage Controlled Voltage Source, `F`, a Current Controlled Current Source, `G`, a Voltage Controlled Current Source and `H`, a Current Controlled Voltage Source). The polynomial function is specified by the keyword `POLY` followed by a number of dimensions: `POLY(ndim)`.

For example:

`POLY(1)` specifies a one-dimensional polynomial (function of one controlling variable)

`POLY(2)` specifies a two-dimensional polynomial (function of two controlling variables)

`POLY(3)` specifies a three-dimensional polynomial (function of three controlling variables)

There is no limit on the number of dimensions or the degree of the polynomial. The keyword `POLY(ndim)` is followed by a list of the polynomial coefficients: `p0`, `p1`, `p2`, `p3`, ...

For a one-dimensional polynomial:

$$\texttt{value} = \texttt{p0} + \texttt{p1} \cdot \texttt{vc1} + \texttt{p2} \cdot \texttt{vc1}^2 + \texttt{p3} \cdot \texttt{vc1}^3 + \cdots \tag{185}$$

For two-dimensional polynomial:

$$\begin{aligned} \texttt{value} = & \texttt{p0} \\ & + \texttt{p1} \cdot \texttt{vc1} + \texttt{p2} \cdot \texttt{vc2} + \\ & + \texttt{p3} \cdot \texttt{vc1}^2 + \texttt{p4} \cdot \texttt{vc1} \cdot \texttt{vc2} + \texttt{p5} * \texttt{vc2}^2 \\ & + \texttt{p6} \cdot \texttt{vc1}^3 + \texttt{p7} \cdot \texttt{vc1}^2 \cdot \texttt{vc2} + \texttt{p8} \cdot \texttt{vc1} \cdot \texttt{vc2}^2 + \texttt{p9} \cdot \texttt{vc2}^3 + \cdots \end{aligned} \tag{186}$$

For a three-dimensional polynomial:

$$\begin{aligned} \texttt{value} = & \texttt{p0} \\ & + \texttt{p1} \cdot \texttt{vc1} + \texttt{p2} \cdot \texttt{vc2} + \texttt{p3} \cdot \texttt{vc3} \\ & + \texttt{p4} \cdot \texttt{vc1}^2 + \texttt{p5} \cdot \texttt{vc1} \cdot \texttt{vc2} + \texttt{p6} \cdot \texttt{vc1} \cdot \texttt{vc3} + \texttt{p7} \cdot \texttt{vc2}^2 + \texttt{p8} \cdot \texttt{vc2} \cdot \texttt{vc3} + \texttt{p9} \cdot \texttt{vc3}^2 \\ & + \texttt{p10} \cdot \texttt{vc1}^3 + \texttt{p11} \cdot \texttt{vc1}^2 \cdot \texttt{vc2} + \texttt{p12} \cdot \texttt{vc1}^2 \cdot \texttt{vc3} \\ & + \texttt{p13} \cdot \texttt{vc1} \cdot \texttt{vc2}^2 + \texttt{p14} \cdot \texttt{vc1} \cdot \texttt{vc2} \cdot \texttt{vc3} + \texttt{p15} \cdot \texttt{vc1} \cdot \texttt{vc3}^2 \\ & + \texttt{p16} \cdot \texttt{vc2}^3 + \texttt{p17} \cdot \texttt{vc2}^2 \cdot \texttt{vc3} + \texttt{p18} \cdot \texttt{vc2} \cdot \texttt{vc3}^2 + \texttt{p19} \cdot \texttt{vc3}^3 + \cdots \end{aligned} \tag{187}$$

What are vc1, vc2, etc. in the above equations ?

Piecewise Linear (PWL) Function

The piecewise linear function is described by a set of data points. A disadvantage of the piecewise linear approach is the fact that though the approximation is continuous, the derivatives are discontinuous, due to the corners. A parameter DELTA is added for smoothing of corners to ensure derivative continuity, supporting better convergence and sets the curvature of the characteristic at the corners. The smoothing algorithm uses a cubic spline approximation at each corner on the interval [X(corner) - DELTA, X(corner) + DELTA]. The maximum value allowed for DELTA is half the smallest distance between the corners. The minimum value DELTA=0 means no smoothing.

A (Analog Behavior Device)

Axxx: Analog device name. This name must begin with the letter ”A”.

n+, n-: Positive and negative terminal node names.

```
Axxx n+ n- I/V='expression'
+ <SCALE=val> <TC1=val> <TC2=val> <M=val>
+ <MIN=val> <MAX=val> <ABS=1>
```

or,

```
Axxx n+ n- DELAY=val <DELIC=val> <RES=val>
+ <SCALE=val> <TC1=val> <TC2=val>
+ <HIGH=val> <LOW=val> <COEF=val>
```

or,

```
Axxx n+ n- LAST <DELIC=val> <RES=val>
+ <SCALE=val> <TC1=val> <TC2=val>
```

I: Current through the device (A-device is a current source)

V: Voltage across the source (A-device is a voltage source)

SCALE: Scaling multiplier for the A-device output variable (current or voltage).

TC1: Linear temperature coefficient for the A-device output variable.

TC2: Quadratic temperature coefficient for the A-device output variable.

SCALE, TC1, and TC2 are involved in calculation of the A-device output variable through:

$$I_{eff}(\text{or}V_{eff}) = I_{out}(\text{or}V_{out}) \cdot \texttt{SCALE} \cdot (1 + \texttt{TC1} \cdot dT + \texttt{TC2} \cdot dT^2) \tag{188}$$

where,

$$dT = \text{temperature} - t_{\text{nominal}} \tag{189}$$

M: Device multiplier, when A-device is a current source.

MIN: Minimum value of output variable (current or voltage). The condition I/V $\geq$ MIN is not effective unless the parameter MIN is specified.

MAX: Maximum value of output variable (current or voltage). The condition I/V $\leq$ MAX is not effective unless the parameter MAX is specified.

ABS=1: Output is absolute value of output variable (current or voltage).

DELAY: Indicates a delay-type device that cannot contain an I/V expression. In transient analysis, the device propagates a voltage value from node n+ to n- with a delay of val seconds. In AC and DC analyses, V(n-) = V(n+).

DELIC: Initial condition for node voltage V(n-) at time 0.

RES: Output impedance. The default is GMIN.

HIGH: The voltage corresponding to logic state 1.

LOW: The voltage corresponding to logic state 0.

COEF: Used to calculate threshold voltage value.

The HIGH, LOW and COEF parameters are not effective unless the LOGIC option is specified in an .OPTIONS statement. The LOGIC=1 or LOGIC=2 option causes event-driven simulation to be performed and the A-device's voltage value V(n-) is equal to HIGH or LOW or (HIGH+LOW)/2. These values represent logic states 1, 0, and X respectively.

LAST: Indicates a delay-type device that cannot contain an I/V expression. When transient analysis is performed, the device propagates from n+ to n- the voltage calculated at the previous time point (time - tstep).

Expression

An expression is a function of: algebraic and logical expressions; real constants; parameter labels; circuit temperature (TEMP); integration time (TIME), integration timestep (TSTEP); frequency (HERTZ); node voltages; voltages across two nodes; branch currents - independent currents

through: independent voltage sources (V), controlled voltage sources (E and H), analog behavioral devices (A) with V-type expressions and inductors (L); operator DER; functions DERIVATIVE and INTEGRAL; user-defined functions by statements:

```
.FUNCmyFunc(x) expression(x)
.DEFINE myFunc(x) expression(x)
.PARAM myFunc(x) = 'expression(x)'
.PARAM myFunc = 'expression(x)'
```

Algebraic and logical expressions can contain or be scholar arguments, but they can also be operands of the functions and operators that are listed:

Logical expression:

```
if_cond: <IF log_cond THEN if_cond | expr ELSE > if_cond | expr
```

where:

log_cond:

```
(log_cond | lexpr log_op rexpr) and (log_cond | lexp log_op rexpr)
(log_cond | lexpr log_op rexpr) or (log_cond | lexpr log_op rexpr)
```

log_op:

```
== or EQ (equal to)
!= or NE (not equal to)
<= or LE (less than or equal to)
<  or LT (less than)
>= or GE (greater than or equal to)
>  or GT (greater than)
```

Where `expr`, `lexpr` and `rexpr` are expressions.

`DER` is the derivative operator with respect to variable “time” and has the syntax:

`DER.V(N)`: The derivative, of the node voltage V(`N`) with respect to time.

`DER.V(N1,N2)`: The derivative, of the voltage across two nodes with respect to time.

`DER.I(DEV)`: The derivative of the independent current I(`DEV`) with respect to time.

The Analog Behavioral can be implemented into a SPICE deck or through schematic entry using SCHOLAR. Two symbols have been created, a BVS (Behavioral Voltage Source) and a BCS (Behavioral Current Source) which are related to V=`'expression'` and I=`'expression'` respectively. These symbols are depicted in Fig. 51.

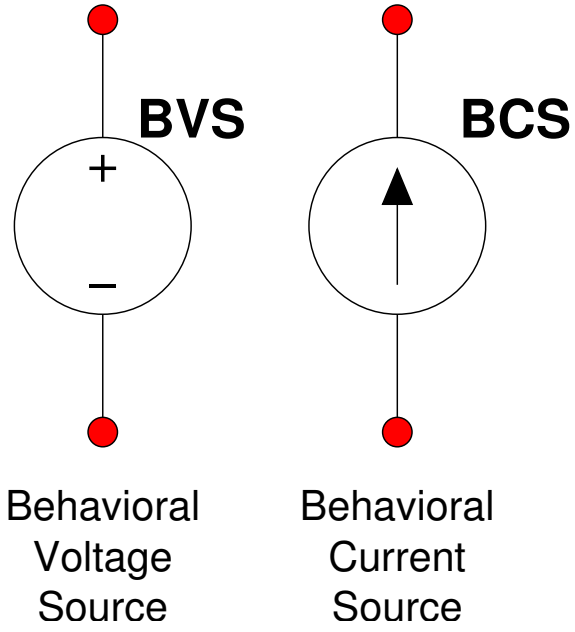

Figure 51: Behavioral model symbols.

Appendix F

VOLTAGE/CURRENT ANALOG BEHAVIORAL IMPLEMENTATION

```
V=If (TD==100K) Then
        @’File_100K_TD’
   Else If (TD==200K) Then
        @’File_200K_TD’
   Else If (TD==500K) Then
        @’File_500K_TD’
   Else If (TD==1Meg) Then
        @’File_1Meg_TD’
   Else 0;
```

Appendix G

ANALOG BEHAVIORAL FOR BACKGATE LEAKAGE CURRENT

```
// Analog Behavioral for Backgate Leakage Current

include "constant.va"

module radtran(d,g,s,b);
//
// Node definitions
//
        inout           d,g,s,b ;   // external nodes
        electrical      d,g,s,b ;   // external nodes
//
//*** Local variables
//
real x, VG, VS, VD, VGprime, VP, VRAD;
real beta, n, iff, ir, Ispec, Id;
//
//*** model parameter definitions
//
parameter real L = 0.8E-6  from[0.0:inf];
parameter real W = 200E-6  from[0.0:inf];

//***  Threshold voltage
//     substrate effect parameters (long-channel)
parameter real VTO    =  31    from[0.0:inf];
parameter real GAMMA  =  0.7    from[0.0:inf];
```

```
parameter real PHI    =  0.5    from[0.2:inf];

//***  Mobility parameters (long-channel)
parameter real KP     =  20E-6   from[0.0:inf];
parameter real THETA  =  50.0E-3 from[0.0:inf];

// Calculation of Radiation VRAD
 If (TD==100k ) then
        VRAD=:
else if ( TD == 500k) then
        VRAD=;
else if (TD==1Meg) then
        VRAD=;
else
        VRAD=0;

analog begin // RADTRAN

VG = V(g); VS = V(s); VD = V(d);

// Effective gate voltage
VGprime = VG - VTO + VRAD+ PHI + GAMMA * sqrt(PHI);

// Pinch-off voltage
VP = VGprime - PHI - GAMMA
   * (sqrt(VGprime+(GAMMA/2.0)*(GAMMA/2.0))-(GAMMA/2.0));

// Slope factor
n = 1.0 + GAMMA / (2.0*sqrt(PHI + VP + 4.0*$vt));
```

```
// Mobility equation
beta = KP * (W/L) * (1.0/(1.0 + THETA * VP));

// forward  and reverse  currents
x=(VP-VS)/$vt; iff = (ln(1.0+exp( x /2.0)))*(ln(1.0+exp( x /2.0)));
x=(VP-VD)/$vt; ir  = (ln(1.0+exp( x /2.0)))*(ln(1.0+exp( x /2.0)));

// Specific current
Ispec = 2 * n * beta * $vt * $vt;

// Drain current
Id = Ispec * (iff - ir);

//
// Back Gate contributions to IDS (Large Device > 150um)
//
I(d,s) <+ Id;

end // analog
endmodule
```

Appendix H

GLOSSARY OF TERMS

A

Ab initio Latin for "from scratch" or "from first principles". Means that all results are based on solutions of Schrödinger's Equation and the wavefunction(s) used. No empirical data is used.

Activation Energy The amount of energy hump or energy barrier needed to allow a reaction to proceed to form transition structure.

Algorithm Mathematical model representation of the application.

Angstrom Unit of distance. $1\ \text{Å} = 10^{-10}$ meters.

Architecture Computing structure or platform used to execute the algorithm.

Atomic Orbital Representation of the electron cloud surrounding an atom. Named by primary quantum number and shape, i.e. 1s, 2s, 2p.

B

Basis Set Group of numerical constants used in the wavefunctions. Named by number and type of wavefunctions used to represent an atom.

Bohr Atom Idea of the atom with electrons in fixed "orbits". Developed by Neils Bohr in early 20^{th} century. Supports idea of ground state and excited state, and explains quantization of photons absorbed and emitted.

Bohr Radius Distance of the first orbit in the Bohr atom from the nucleus. $a_0 = 0.529$ Å

Boltzmann's Constant $k_B = 1.380 \times 10^{-23}\ \text{J/K}$

Bond, Covalent A shared orbital between two atoms.

Bond, Ionic An electrostatic attraction between two ions.

Bond Angle Angle from a pair of bonded atoms to another atom, one of the bonded pair being the vertex.

Bond Length Distance between the nuclei of two bonded atoms.

Born Oppenheimer Approximation Used to simplify Schrödinger's Equation. Assumes that nuclei are massive and slow-moving compared to electrons.

D

Debye Unit of dipole moment.

Delta Greek symbol, looks like a triangle and denotes "change in".

Delocalization, Delocalized Electrons which do not reside along a single bond, but move from bond to bond.

Density Functional Theory A theoretical framework for treating the complicated interactions in an N-electron system leading to effective one-electron equations which form the basis for most current electronic structure calculations for solids, surfaces, and many molecules. Walter Kohn received the 1998 Nobel Prize in Chemistry for his work on density functional theory.

Dihedral Angle Angle between an atom and a plane, formed by three or more other atoms.

Dipole Equal positive and negative charges separated by a distance.

Dipole Moment Measure of how polarized a molecule i.e. how large the dipole is.

Dissociation When a compound separates into two or more parts.

Double Bond A pair of shared electrons, called a "Pi" bonding in which atoms at either end cannot rotate around bond.

E

Effective Medium Theory An empirical approach to describe the interactions between atoms using the electron density and empirical repulsive terms.

Eigenfunction, Eigenvalue Function such that when an operation is performed on it, the result is the same function times a constant. That constant is know as the eigenvalue.

Electron Subatomic particle, with wave-like qualities, negatively charged found in all atoms balancing the charge of nucleus.

Electron Affinity The energy released when an electron is added to an atom.

Electron charge $q = -1.602 \times 10^{-19}$ C

Electron cloud Physical space where the electron's wavefunction indicates it has a high probability of appearing.

Electron density A measure of the "thickness" of the electron cloud in a given place, the probability of the electron's presence. Function defined over all space; sum over all space gives number of electrons present.

Electron structure Way of accounting for the shape of an electron cloud. Indicates which orbitals are occupied.

Electronegativity An atom's attraction for the electrons in a bond.

Electrostatic potential Attraction between positive and negative charges. Relating to a molecule, it expresses what would happen to a small positive charge brought near the molecule.

Excited state When electrons are not in the lowest possible orbitals.

Extended Basis Set Function A basis set that describes the orbitals in great detail.

Electron Volt $1 \text{ eV} = 1.602 \times 10^{-19}$ J

F

Fermi level The energy of the highest occupied states in a metal or semiconductor.

G

Gaussian Mathematical function shaped like the normal distribution, or bell curve. Used in approximating the wavefunction.

Geometry of a molecule Description of bond lengths and angles.

Ground state When electrons are in lowest possible orbitals.

GTO (Gaussian Type Orbital) An approximation of the wavefunction using gaussian curves.

GW method A many-electron method to calculate excitation energies in semiconductors and insulators. It uses a Green's function (G) and a screened Coulomb potential (denoted W) to express the so-called self-energy operator. The self-consistent solution of quasi-particle equations containing the self-energy operator gives quasi particle energies, which can be interpreted as excitation energies. The GW method, which is computationally very demanding, can be performed after a local density functional calculation.

H

Hamiltonian Mathematical operator used in the Schrödinger Equation.

Hartree Amount of electrostatic repulsion between two electrons held one Bohr radius apart used as atomic unit of energy.

Hartree Fock approximation Used to simplify Schrödinger's Equation. Breaks complex orbitals down into a series of one-electron orbitals, sometimes called Self Consistent Field (SCF) method, UHF or RHF for unrestricted and restricted Hartree Fock approximations. Unrestricted methods allow for lone electrons, while restricted methods only deal with paired electrons.

Heat of Formation Energy which would be required to form a molecule from dissociated atoms. If positive, the structure will not be formed spontaneously. Lower heats of formation indicate more stable molecules, which are formed preferentially. A difference of one kcal/mol means that the more stable geometry will be approximately 10 times more common.

HOMO (Highest Occupied Molecular Orbital) Orbital with the most energy which contains an electron.

Hybrid orbital The mixing of orbitals, like one s-orbital with two p orbitals result in sp2 hybrid orbitals.

Hybridization When orbitals combine to form bonds which are not exactly one shape or the other.

I

Imaginary frequency Vibration which is impossible, ie, would cause molecule to spontaneously break down. Finding EXACTLY ONE indicates that molecule is a transition structure.

Ion Atom or group of atoms which has a net charge. Three are not enough electrons to properly balance out the charge of the nuclei.

Ionization energy Amount of energy required to remove one electron from an atom.

J

Jellium Model A simple model for bulk metals and metal surfaces. The atomic nuclei are replaced by a uniform positive background with a sharp drop to zero at the surface. The distribution of electrons in the resulting potential is calculated using density functional theory yielding properties such as the work function.

L

LCAO (Linear Combination of Atomic Orbitals) An approximation which sums atomic orbitals, with certain coefficients to produce molecular bonding and anti-bonding orbitals.

LUMO (Lowest Unoccupied Molecular Orbital) Orbital with least energy without any electrons in it.

M

Magnetic Quantum Number Describes the shape of the orbital. Often described in terms of the x,y,z orientation of the orbital, e.g., $2p_x$ where the x is the magnetic quantum number. Also called ”azimuthal quantum number”, written ”m”.

Maximum, global Molecular geometry with the largest possible energy.

Maximum, local relating to energy Molecular geometry with an energy larger than most, however, not the largest energy possible.

Minimal Basis Set Function A basis set that describes only the most basic aspects of the orbitals.

Minimal, global Configuration with lowest possible energy.

Minimum, local Configuration with lowest possible energy.

Molecule More than one atom bonded together.

Molecular mechanics Method of using empirical data to greatly simplify the calculations for very large molecules.

Molecular orbital Representation of electron cloud surrounding a molecule. May be hybridized.

Muffin-tin potential A simple form of a crystal potential for quantum mechanical calculations. The space in the crystal is partitioned into spheres around the atoms and a remaining interstitial region. Inside the spheres the potential is assumed to have only radial dependence. In the interstitial region the potential is take to be constant.

N

Nanometer Measure of length, equal to 10^{-9} m.

Nucleus Collection of subatomic particles found in the center of an atom and is positively charged.

O

Orbital Representation of electron cloud.

Order-N methods Quantum mechanical methods where the computational efforts increases linearly with the number of atoms. These methods are also sometimes referred to as ”linear-scaling methods”.

P

Phase One of the three normal states of matter, solid, liquid, or gas, depending on the level of organization between particles.

Pi (Π) bond A single covalent bond in which two paired electrons lie between the two bonded atoms.

Picometer Measure of length, equal to 10^{-12} m.

Planck Constant Numerical value expressing the amount of uncertainty which must be present in any concurrent measurement of a particle's position and momentum.
($\hbar = \mathrm{h}/2\pi$, $\mathrm{h} = 6.626 \times 10^{-19}$ Js).

P-orbital A cloud with two lobes (px, py and pz) on opposite sides of the nucleus.

Potential Energy Surface A mathematical relationship between different molecular geometries and their corresponding single point energies.

Primary quantum number Number used in electron structure notation, 1s, 2s, etc. Correcponds to the orbit in the Bohr atom where an electon would be found. Written ”n”.

Probabilty A number between one and zero which denotes how likely an event is to happen. Multiplied by 100, it becomes a percentage.

Probability density A mathematical distribution of probability over space or time. Sum of all probabilities must equal one.

Q

Quantum Separate units of something. An example is money comes in quanta of 1 cent.

Quantum Numbers Set of numbers used to specify any orbital in a given atom. Consist of Primary, Secondary, Azimuthal, and Spin numbers.

R

Radius Distance from the center to the edge. In chemistry and physics it usually is associated with the distance.

Resonance structure Different possible structures for the same molecule.

S

Saddle Point A molecular geometry such that slight changes cause both a maximum in one direction and a minimum in the other. Saddle points represent a transition structure connecting two equilibrium structures.

Schrödinger’s Equation Original equation used to write wavefunctions for particles, incorporating the Hamiltonian.

Secondary Quantum Number Has values of +1/2 or -1/2, also called ”up” and ”down” or ”alpha” and ”beta” spin. Serves to differentiate between two electrons in the same orbital. Written ”m_s”.

Shell model An empirical potential model which includes effects of electronic polarization. In addition to the potential terms describing long-range attraction and short-range repulsion between atoms, the electrons are represented by a negatively charged shell which is connected by a harmonic spring to the positive nucleus. The spring constant is chosen to fit experimental data such as polarizabilities.

Sigma (σ) bond A single covalent bond in which two paired electrons lie between the two bonded atoms.

S-orbital A spherical cloud that becomes less dense as the distance from the nucleus increases.

Split Valence Basis Set Basis set which uses several wavefunctions to represent different valences. Denoted by a star at the end of name.

STO (Slater Type Orbital) Orbital using Slater renormalization factor to approximate wavefunction.

Symmetry (Point-Group Symmetry) Properties of a molecule describing how it can be transformed and still appear exactly the same. Point-group symmetry is a method of naming the combination of symmetry elements which a molecule has.

T

Tight-binding method A semi-empirical quantum mechanical method which is used for the description of inorganic materials such as transition metal compounds with pronounced covalent character.

Transition state (transition structure) Molecule or group of molecules formed during a reaction. Unstable, containing weak bonds and having high energy. Requires energy of activation to form. Vibrates at imaginary frequencies.

Triple bond Three shared electrons.

U

Unfilled Valence Valence which has no electrons in it.

V

Valence One level of an orbital

Valence electrons The outermost electrons in an atom.

W

Wavefunction Complex mathematical representation of a particle.

REFERENCES

[1] F. B. McLean, H. E. Boesch, Jr., and T. R. Oldham, *Electron-Hole Generation, Transport, and Trapping in* SiO_2 *in Ionizing Radiation Effects in MOS Devices and Circuits*, John Wiley and Sons, New York, 1989, (Chapter 3, page 87).

[2] T. P. Ma and Paul V. Dressendorfer, *Ionizing Radiation Effects in MOS Devices and Circuits*, John Wiley and Sons, 1989.

[3] George C. Messenger and Milton S. Ash, *The Effects of Radiation on Electronic Systems*, Van Nostrand Reinhold, July 1992.

[4] C. J. Nicklaw, M. P. Pagey, S. T. Pantelides, D. M. Fleetwood, R. D. Schrimpf, K. F. Galloway, J. E. Wittig, B. M. Howard, E. Taw, W. H. McNeil, and J. F. Conley, "Defects and Nanocrystals Generated by Si Implantation into a-SiO_2", *IEEE Transactions on Nuclear Science*, vol. 47, no. 6, pp. 2269–2275, Dec. 2000.

[5] D. R. Alexander, *Design Issues for Radiation Tolerant Microciruits for Space*, IEEE Nuclear Science and Radiation Effects Conference Short Course, 1996.

[6] SILVACO International, Santa Clara, *ATLAS User's Manual, Volume I*, February 2000.

[7] SILVACO International, Santa Clara, *ATLAS User's Manual, Volume II*, February 2000.

[8] J. M. Thijssen, *Computational Physics*, Cambridge University Press, May 1, 1999.

[9] J. Bhaskar, *Verilog HDL Synthesis: A Practical Primer*, Star Galaxy Publisher, 1st edition, 1998.

[10] J. Bhasker, *A VHDL Primer*, Prentice Hall, 3rd edition, 1998.

[11] D. E. Thomas, P. R. Moorby, and D. B. Thomas, *The Verilog Hardware Description Language*, Kluwer Academic Publications, 5th edition, 2002.

[12] T. Grotker, G. Margin, and S. Liao, *System Design with System-C*, Kluwer Academic Publications, 2002.

[13] P. K. Ko, J. H. Huang, Z. H. Liu, and C. Hu, "BSIM3 for Analog and Digital Circuit Simulation", *IEEE Symposium on VLSI Technology and CAD*, pp. 400–429, Jan. 1993.

[14] J. M. Aitken, "Radiation-Induced Trapping Centers in Thin Silicon Dioxide Films", *Journal of Non-Crystalline Solids*, vol. 40, pp. 31–47, 1980.

[15] J. F. Conley, Jr. and P. M. Lenahan, "Room Temperature Reactions Involving Silicon Dangling Bond Centers and Molecular Hydrogen in Amorphous SiO_2 Thin Film on Silicon", *Appl. Phys. Lett.*, vol. 62, no. 1, pp. 40–42, Jan. 1993.

[16] J. M. Benedetto and H. E. Boesch, "The Relationship Between Co^{60} and 10 keV X-Ray-Damage in MOS Devices", *IEEE Transactions on Nuclear Science*, vol. 33, no. 6, pp. 1318–1323, Dec. 1986.

[17] F. B. McLean and H. E. Boesch, Jr., "Time-Dependent Degradation of MOSFET Channel Mobility Following Pulsed Irradiation", *IEEE Transactions on Nuclear Science*, vol. 36, no. 6, pp. 1772–1783, Dec. 1989.

[18] P. M. Lenahan, J. J. Mele, J. F. Conley, Jr., R. K. Lowry, and D. Woodbury, "Predicting Radiation Response From Process Parameters: Verification Of A Physically Based Predictive Model", *IEEE Transactions on Nuclear Science*, vol. 46, no. 6, pp. 1534–1543, Dec. 1999.

[19] R. K. Freitag, D. B. Brown, and C. M. Dozier, "Experimental Evidence of Two Species of Radiation-Induced Trapped Positive Charge", *IEEE Transactions on Nuclear Science*, vol. 40, no. 6, pp. 1316–1322, 1993.

[20] J. F. Conley, Jr. and P. M. Lenahan, "Room-Temperature Reactions Involving Silicon Dangling Bond Centers and Molecular-Hydrogen in Amorphous SiO_2 Thin-Films on Silicon", *Applied Physics Letters*, vol. 62, no. 1, pp. 40–42, 1993.

[21] D. M. Fleetwood, W. L. Warren, J. R. Schwank, P. S. Winokur, M. R. Shaneyfelt, and L. C. Riewe, "Effects of Interface Traps and Border Traps on MOS Postirradiation Annealing Response", *IEEE Transactions on Nuclear Science*, vol. 42, pp. 1698–1707, 1995.

[22] A. Stesmans and V. V. Afanasev, "Thermally Induced Interface Degradation in (111) Si/SiO_2 Traced by Electron Spin Resonance", *Physical Review B*, vol. 54, no. 16, pp. R11 129–132, 15 Oct. 1996.

[23] E. H. Poindexter, G. J. Gerardi, M.-E. Rueckel, P. J. Caplan, N. M. Johnson, and D. K. Biegelsen, "Electronic Traps and P_b Centers at the Si/SiO_2 Interface: Band-Gap Energy Distribution", *Journal of Applied Physics*, vol. 56, no. 10, pp. 2844–2849, 15 Nov. 1984.

[24] J. F. Conley, Jr. and P. M. Lenahan, "Room-Temperature Reactions Involving Silicon Dangling Bond Centers and Molecular-Hydrogen in Amorphous SiO_2 Thin-Films on Silicon", *IEEE Transactions on Nuclear Science*, vol. 39, no. 6, pp. 2186–2191, Dec. 1992.

[25] J. F. Conley, Jr. and P. M. Lenahan, "Molecular Hydrogen, E' Center Hole Traps, and Radiation-Induced Interface Traps in MOS Devices", *IEEE Transactions on Nuclear Science*, vol. 40, no. 6, pp. 1335–1340, 1993.

[26] N. S. Saks, R. B. Klein, R. E. Stahlbush, B. J. Mrstik, and R. W. Rendell, "Effects of Post-Stress Hydrogen Annealing on MOS Oxides After ^{60}Co Irradiation or Fowler-Nordheim Injection", *IEEE Transactions on Nuclear Science*, vol. 40, no. 6, pp. 1341–1349, 1993.

[27] J. R. Schwank, D. M. Fleetwood, M. R. Shaneyfelt, P. S. Winokur, C. L. Axness, and L. C. Riewe, "Latent Interface-Trap Buildup and Its Implications for Hardness Assurance", *IEEE Transactions on Nuclear Science*, vol. 39, no. 6, pp. 1953–1963, Dec. 1992.

[28] P. E. Bunson, M. Di Ventra, S. T. Pantelides, D. M. Fleetwood, and R. D. Schrimpf, "Hydrogen-Related Defects in Irradiated SiO_2", *IEEE Transactions on Nuclear Science*, vol. 47, no. 6, pp. 2289–2296, Dec. 2000.

[29] P. E. Bunson, M. Di Ventra, S. T. Pantelides, R. D. Schrimpf, and K. F. Galloway, "Ab initio calculations of H^+ energetics in SiO_2: Implications for transport", *IEEE Transactions on Nuclear Science*, vol. 46, no. 6, pp. 1568–1573, Dec. 1999.

[30] S. N. Rashkeev, D. M. Fleetwood, R. D. Schrimpf, and S. T. Pantelides, "Defect Generation by Hydrogen at Si-SiO_2 Interface", *Physical Review Letters*, vol. 87, no. 16, pp. 165506–1–165506–4, 15 Oct. 2001.

[31] F. W. Sexton and J. R. Schwank, "Correlation of Radiation Effects in Transistors and Integrated-Circuits", *IEEE Transactions on Nuclear Science*, vol. 32, no. 6, pp. 3975–3981, Dec. 1985.

[32] K. F. Galloway, M. Gaitan, and T. J. Russell, "A Simple Model for Separating Interface and Oxide Charge Effects in MOS Device Characteristics", *IEEE Transactions on Nuclear Science*, vol. NS-31, no. 6, pp. 1497–1501, 1984.

[33] Y. Nishioka, T. Itoga, K. Ohyu, M. Kato, and T.-P. Ma, "Radiation Effects On Fluorinated Field Oxides And Associated Devices", *IEEE Transactions on Nuclear Science*, vol. 37, no. 6, pp. 2026–2032, Dec. 1990.

[34] S. Wolf, *Silicon Processing for the VLSI Era: Volume 4 - Deep-Submicron Process Technology*, Lattice Press, May 2002.

[35] S. Wolf and R. N. Tauber, *Silicon Processing for the VLSI Era : Process Technology*, Lattice Press, 2nd edition, Nov. 1999.

[36] S. Wolf, *Silicon Processing for the Vlsi Era: Process Integration*, Lattice Press, Mar. 1990.

[37] R. A. Swalin, *Thermodynamics of Solids*, John Wiley & Sons, 1972.

[38] J. F. Conley, Jr. and P. M. Lenahan, "Hydrogen Complexed EP (E'_δ) Centers and EP/H_2 Interactions: Implications for EP Structure", *Microelectronic Engineering*, vol. 28, no. 1-4, pp. 35–38, June 1995.

[39] J. F. Conley, Jr. and Patrick M. Lenahan, "Electron Spin Resonance Evidence that E'_γ Centers Can Behave as Switching Oxide Traps", *IEEE Transactions on Nuclear Science*, vol. 42, no. 6, pp. 1744–1749, Dec. 1995.

[40] J. F. Conley, Jr. and P. M. Lenahan, "Molecular Hydrogen, E' Centers Hole Traps and Radiation Induced Interface Traps in MOS Devices", Private Communication, Dec. 1993.

[41] D. M. Fleetwood, P. S. Winokur, R. A. Reber, Jr., T. L. Meisenheimer, J. R. Schwank, M. R. Shaneyfelt, and L. C. Riewe, "Effects of Oxide Traps, Interface Traps, and "Border Traps" on Metal-Oxide-Semiconductor Devices", *Journal of Applied Physics*, vol. 73, no. 10, pp. 5058–5074, May 1993.

[42] J. R. Schwank, F. W. Sexton, D. M. Fleetwood, M. R. Shaneyfelt, K. L. Hughes, and M. S. Rodgers, "Strategies For Lot Acceptance Testing Using CMOS Transistors And ICs", *IEEE Transactions on Nuclear Science*, vol. 36, no. 6, pp. 1971–1980, Dec. 1989.

[43] Robert G. Parr and Weitao Yang, *Density-Functional Theory of Atoms and Molecules*, Oxford Science Publications, 1989.

[44] S. M. Sze, *Physics of Semiconductor Devices*, John Wiley and Sons, New York, second edition, 1981.

[45] G. Barbottin and A. Vapaille, Eds., *Instabilities in Silicon Devices: Silicon Passivation and Related Instabiliites*, vol. 2, North-Holland, 1989.

[46] P. M. Lenahan and P. V. Dressendorfer, "Hole Traps and Trivalent Silicon Centers in Metal/Oxide/Silicon Devices", *Journal of Applied Physics*, vol. 55, pp. 3495–3499, 1984.

[47] P. M. Lenahan and J. F. Conley, "A Comprehensive Physically Based Predictive Model For Radiation Damage In MOS Systems", *IEEE Transactions on Nuclear Science*, vol. 45, no. 6, pp. 2413–2423, Dec. 1998.

[48] W. L. Warren, M. R. Shaneyfelt, D. M. Fleetwood, J. R. Schwank, P. S. Winokur, and R. B. Devine, "Microscopic Nature of Border Traps in MOS Oxides", *IEEE Transactions on Nuclear Science*, vol. NS-41, pp. 1817–1827, 1994.

[49] Frank J. Feigl, W. Beall Fowler, and Kwok L. Yip, "Oxygen Vacancy Model for the E' Center in SiO_2", *Solid State Communications*, vol. 14, pp. 225–229, 1974.

[50] P. M. Lenahan, W. L. Warren, D. T. Krick, P. V. Dressendorfer, and B. B. Triplett, "Interaction of Molecular-Hydrogen with Trapped Hole E' Centers in Irradiated and High-Field Stressed Metal-Oxide Silicon-Oxides", *Journal of Applied Physics*, vol. 67, no. 12, pp. 7612–7614, 1990.

[51] S. P. Karna, H. A. Kurtz, W. M. Shedd, R. D. Pugh, and B. K. Singaraju, "New fundamental defects in a-SiO_2", *IEEE Transactions on Nuclear Science*, vol. 46, no. 6, pp. 1544–1552, Dec. 1999.

[52] J. R. Chavez, S. P. Karna, A. C. Pineda, R. D. Pugh, W. M. Shedd, and T. R. Oldham, "Microscopic Structure of the E'_δ Center in Amorphous SiO_2: A First Principles Quantum Mechanical Investigation", *IEEE Transactions on Nuclear Science*, vol. 44, no. 6, pp. 1799–1803, Dec. 1997.

[53] A. Courtot-Descharles, P. Paillet, and J. L. Leray, "Theoretical Study Using Density Functional Theory of Defects in Amorphous Silicon Dioxide", *Journal of Non-Crystalline Solids*, vol. 245, pp. 154–160, 1999.

[54] S. P. Karna, A. C. Pineda, R. D. Pugh, W. M. Shedd, and T. R. Oldham, "Electronic Structure Theory and Mechanisms of the Oxide Trapped Hole Annealing Process", *IEEE Transactions on Nuclear Science*, vol. 47, no. 6, pp. 2316–2323, Dec. 2000.

[55] J. K. Rudra and W. B. Fowler, "Oxygen Vacancy and the E'_1 Center in Crystalline SiO_2", *Physical Review B*, vol. 35, pp. 8223–8229, 15 May 1987.

[56] W. L. Warren, J. Kanicki, F. C. Rong, and E. H. Poindexter, "Paramagnetic Point Defects in Amorphous Silicon Dioxide and Amorphous Silicon Nitride Thin Films", *J. Electrochem. Soc.*, vol. 139, no. 3, pp. 880–889, Mar. 1992.

[57] D. L. Griscom and E. J. Friebele, "Fundamental Radiation-Induced Defect Centers in Synthetic Fused Silicas: Atomic Chlorine, Delocalized E′ Centers and Triplet State", *Physical Review B*, vol. 34, pp. 7524–7533, 1986.

[58] R. A. Weeks, "The Many Varieties of E′ Centers: A Review", *Journal of Non-Crystalline Solids*, vol. 179, pp. 1–9, 1994.

[59] L. Skuja, "Section 1. Defect Studies in Vitreous Silica and Releated Materials: Optically Active Oxygen-Deficiency-Related Centers in Amorphous Silicon Dioxide", *Journal of Non-Crystalline Solids*, vol. 239, pp. 16–48, 1998.

[60] R. G. Parr and W. Yang, *Density Functional Theory of Atoms and Molecules*, Oxford University Press, 1989.

[61] P. Hohenberg and W. Kohn, "Inhomogeneous Electron Gas", *Physical Review*, vol. 136, no. 3B, pp. B864–B871, 9 Nov. 1964.

[62] W. Kohn and L. J. Sham, "Self-Consistent Equation Including Exchange and Correlation Effects", *Physical Review*, vol. 140, pp. A1133–A1138, 1965.

[63] Arthur H. Edwards, W. Beall Fowler, and Frank J. Feigl, "Asymmetrical Relaxation of Simple E′ Centers in Silicon Dioxide Isomorphs", *Physical Review B*, vol. 37, no. 15, pp. 9000–9005, 15 May 1988.

[64] J. P. Perdew and W. Yang, *Electronic Structure of Solids*, Akadamie Verlag, Berlin, 1991.

[65] J. Sarnthein, A. Pasquarello, and R. Car, "Model of Vitreous SiO_2 Generated by an *ab initio* Molecular-Dynamics Quench from the Melt", *Physical Review Letters*, vol. 74, pp. 4682–4688, 1995.

[66] J. Sarnthein, A. Pasquarello, and R. Car, "Model of Vitreous SiO_2 Generated by an *ab initio* Molecular-Dynamics Quench from the Melt", *Physical Review B*, vol. 42, pp. 12690, 1995.

[67] M. Boero, A. Pasquarello, J. Sarnthein, and R. Car, "Structure and Hyperfine Parameters of E_1' Centers in α-Quartz and in Vitreous SiO_2", *Physical Review Letters*, vol. 78, no. 5, pp. 887–890, 3 Feb. 1997.

[68] M. Walters and A. Reisman, "Radiation-Induced Neutral Electron Trap Generation in Electrically Biased Insulated Gate Field Effect Transistor Gate Insulators", *Journal of the Electrochemical Society*, vol. 138, pp. 2756–2760, 1991.

[69] D. Goguenheim and M. Lannoo, "Theoretical and Experimental Aspects of the Thermal Dependence of Electron Capture Coefficients", *Journal of Applied Physics*, vol. 68, no. 3, pp. 1059–1069, 1 Aug. 1990.

[70] D. Goguenheim and M. Lannoo, "Theoretical Calculation of the Electron-Capture Cross Section due to a Dangling Bond at the Si(111)-SiO_2 Interface", *Physical Review B*, vol. 44, no. 4, pp. 1724–1733, 15 July 1991.

[71] D. M. Fleetwood, T. L. Mesisenheimer, and J. H. Scofield, "1/f Noise and Radiation Effects in MOS Devices", *IEEE Transactions on Electron Devices*, vol. 41, no. 11, pp. 1953–1964, 1994.

[72] A. J. Lelis, H. E. Boesch, Jr., T. R. Oldham, and F. B. McLean, "Reversibility of Trapped Hole Annealing", *IEEE Transactions on Nuclear Science*, vol. 35, no. 6, pp. 1186–1191, Dec. 1988.

[73] A. J. Lelis, T. R. Oldham, H. E. Boesh, Jr., and F. B. McLean, "The Nature of the Trapped Hole Annealing Process", *IEEE Transactions on Nuclear Science*, vol. 36, no. 6, pp. 1808–1815, Dec. 1989.

[74] J. R. Schwank, P. S. Winokur, P. J. McWhorter, F. W. Sexton, P. V. Dressendorfer, and D. C. Turpin, "Physical Mechanisms Contributing to Device "Rebound"", *IEEE Transactions on Nuclear Science*, vol. NS-31, no. 6, pp. 1434–1438, Dec. 1984.

[75] D. M. Fleetwood, M. R. Shaneyfelt, L. C. Riewe, P. S. Winokur, and R. A. Reber, "The Role of Border Traps in MOS High-Temperature Postirradiation Annealing Response", *IEEE Transactions on Nuclear Science*, vol. 40, no. 6, pp. 1323–1334, 1993.

[76] Timothy R. Oldham, *Ionizing Radiation Effects in MOS Oxides*, World Scientific Publishing Company, Incorporated, 2000.

[77] D. M. Fleetwood, P. S. Winokur, L. C. Riewe, O. Flament, P. Paillet, and J. L. Leray, "The Role Of Electron Transport And Trapping In MOS Total-Dose Modeling", *IEEE Transactions on Nuclear Science*, vol. 46, no. 6, pp. 1519–1525, Dec. 1999.

[78] C. J. Nicklaw, Z. Y. Lu, D. M. Fleetwood, R. D. Schrimpf, and S. T. Pantelides, "The Structures, Properties, and Dynamics of Oxygen Vacancies in Amorphous SiO_2", *IEEE Transactions on Nuclear Science*, vol. 49, no. 6, pp. 2667–2673, Dec. 2002.

[79] H. Z. Massoud, E. H. Pointdexter, and C. R. Helms, Eds., *The Physics and Chemistry of* SiO_2 *and the Si*-SiO_2 *Interface*, vol. 3, The Electrochemical Society, Inc., 1996.

[80] S. T. Pantelides, S. N. Rashkeev, R. Buczko, D. M. Fleetwood, and R. D. Schrimpf, "Reactions of Hydrogen with Si-SiO_2 Interfaces", *IEEE Transactions on Nuclear Science*, vol. 47, no. 6, pp. 2262–2268, Dec. 2000.

[81] B. J. Mrstik, "Hydrogen Permeability in Thermally Grown Films of SiO_2 on Silicon Substrates", *Physical Review*, vol. 47, pp. 4115–4120, 1993.

[82] B. J. Mrstik and R. W. Rendell, "Model for Si–SiO_2 Interface State Formation During Irradiation and During Postirradiation Exposure to Hydrogen Environment", *Applied Physics Letters*, vol. 59, no. 23, pp. 3012–3014, 1991.

[83] B. J. Mrstik, P. J. McMarr, N. S. Saks, R. W. Rendell, and R. B. Klein, "Hydrogen Permeability in Thermally Grown Films of SiO_2 on Silicon Substrates", *Physical Review B – Condensed Matter*, vol. 47, no. 7, pp. 4115–4118, 1993.

[84] D. L. Griscom, "Hydrogen Model for Radiation Induced Interface States in SiO_2-on-Si Structures : A Review of the Evidence", *Journal of Electronic Materials*, vol. 21, no. 7, pp. 763–767, 1992.

[85] B. J. Mrstik, P. J. McMarr, R. K. Lawrence, and H. L. Hughes, "A Study Of The Radiation Sensitivity Of Non-Crystalline SiO_2 Films Using Spectroscopic Ellipsometry", *IEEE Transactions on Nuclear Science*, vol. 45, no. 6, pp. 2450–2457, Dec. 1998.

[86] F. B. McLean, "A Framework for Understanding Radiation-Induced Interface States in $Si-SiO_2$ MOS Structures", *IEEE Transactions on Nuclear Science*, vol. 27, pp. 1651–1657, 1980.

[87] M. R. Shaneyfelt, J. R. Schwank, D. M. Fleetwood, and P. S. Winokur, "Interface-Trap Buildup Rate in Wet and Dry Oxides", *IEEE Transactions on Nuclear Science*, vol. 39, no. 6, pp. 2244–2251, IEEE Transactions on Nuclear Science 1992.

[88] M. R. Shaneyfelt, J. R. Schwank, D. B. Fleetwood, P. S. Winokur, K. L. Hughes, and F. W. Sexton, "Field Dependence Of Interface-Trap Buildup In Polysilicon And Metal Gate MOS Devices", *IEEE Transactions on Nuclear Science*, vol. 37, no. 6, pp. 1632–1640, Dec. 1990.

[89] B. J. Mrstik and R. W. Rendell, "Si–SiO_2 Interface State Generation During X-Ray Irradiation and During Postirradiation Exposure to a Hydrogen Ambient", *IEEE Transactions on Nuclear Science*, vol. 38, no. 6, pp. 1101–1110, 1991.

[90] A. Stesmans, "Dissociation Kinetics of Hydrogen-Passivated P_b Defects at the (111)Si/SiO_2 Interface", *Physical Review B*, vol. 61, no. 12, pp. 8393–8403, 15 Mar. 2000.

[91] A. Stesman, R. Devine, A. G. Revesz, and H. Hughes, "Irradiation-Induced ESR Active Defects in SIMOX Structures", *IEEE Transactions on Nuclear Science*, vol. 37, no. 6, pp. 2008–2012, Dec. 1990.

[92] A. Stesmans, "The $Si \equiv Si_3$ Defect at Various (111)Si/SiO_2 and (111)Si/Si_3N_4 Interfaces", *Semicond. Sci. Technol.*, vol. 4, pp. 1000–1011, 1989.

[93] S. N. Rashkeev, D. M. Fleetwood, R. D. Schrimpf, and S. T. Pantelides, "Proton-Induced Defect Generation at the Si-SiO_2 Interface", *IEEE Transactions on Nuclear Science*, vol. 48, no. 6, pp. 2086–2092, Dec. 2001.

[94] O. L. Curtis, Jr. and J. R. Srour, "The Multiple-Trapping Model and Hole Transport in SiO_2", *Journal of Applied Physics*, vol. 48, no. 9, pp. 3819–3828, Sept. 1977.

[95] J. Noolandi, "Equivalence of Multiple-Trapping Model and Time-Dependent Random Walk", *Physical Review B*, vol. 16, no. 10, pp. 4474–4479, 15 November 1977.

[96] V. Vasudevan and J. Vasi, "A Simulation of the Multiple-Trapping Model for Continous Time Random Walk Transport", *Journal of Applied Physics*, vol. 74, pp. 3224–3230, 1993.

[97] *Python Documentation*, release 2.2.1 edition, Apr. 2002.

[98] G. A. Ausman and F. B. McLean, "Electron-Hole Pair Creation Energy in SiO_2", *Applied Physics Letters*, vol. 26, pp. 173–175, 1975.

[99] C. R. Viswanathan and J. Maserjian, "Model for Thickness Dependence of Radiation Charging in MOS Structures", *IEEE Transactions on Nuclear Science*, vol. 23, no. 6, pp. 1540–1545, 1976.

[100] S. M. Sze, *Physics of Semiconductor Devices*, John Wiley and Sons, New York, 1981.

[101] Silvaco International, *SmartSpice/UTMOST-III Modeling Manual: Vol. 1*, Dec. 2002.

[102] Silvaco International, *SmartSpice/UTMOST-III Modeling Manual: Vol. 2*, Dec. 2002.

[103] Silvaco International, *SmartSpice/UTMOST-III Modeling Manual: Vol. 3*, Dec. 2002.

[104] Randall J. Milanowski, *Transient Simulation of Radiation-Induced Charge Trapping and Interface Trap Formation Using a Physically-Based, Three-Carrier Transport Model in Silicon Dioxide*, PhD thesis, Vanderbilt University, 1999.

[105] R. J. Milanowski, M. P. Pagey, L. W. Massengill, R. D. Schrimpf, M. E. Wood, B. W. Offord, R. J. Graves, K. F. Galloway, C. J. Nicklaw, and E. P. Kelley, "TCAD-Assisted Analysis of Back-Channel Leakage in Irradiated Mesa SOI nMOSFETs", *IEEE Transactions on Nuclear Science*, vol. 45, no. 6, pp. 2593–2599, Dec. 1998.

[106] R. O. Jones and O. Gunnarsson, "The Density Functional Formalism, Its Applications and Prospects", *Reviews of Modern Physics*, vol. 61, no. 3, pp. 689–746, 1989.

[107] D. M. Ceperley and B. J. Alder, "Ground-State of the Electron-Gas by a Stochastic Method", *Physical Review Letters*, vol. 45, no. 7, pp. 566–569, 1980.

[108] E. H. Nicollian and J. R. Brews, *MOS (Metal Oxide Semiconductor) Physics and Technology*, John Wiley and Sons, Nov. 2002.

[109] E. H. Nicollian and J. R. Brews, *MOS (Metal Oxide Semiconductor) Physics and Technology*, John Wiley and Sons, New York, 1982.

[110] S. Cristoloveanu, P. L. Hemment, K. Izumi, and S. Wilson, Eds., *Silicon-On-Insulator Technology & Devices VIII*, Electrochemical Society, June 1997.

[111] S. Cristoloveanu, D. Muteanu, and M. S. T. Liu, "A Review Of The Pseudo-MOS Transistor in SOI Wafers: Operation, Parameter Extraction, And Applications", *IEEE Transactions on Electron Devices*, vol. 147, no. 5, pp. 1018–1027, May 2000.